Semi-Analytical Modeling of Water Injection Under Fracturing Conditions by Capturing Effects of Formation Damage Mechanisms to Predict Fracture Propagation

Aditya Harsh

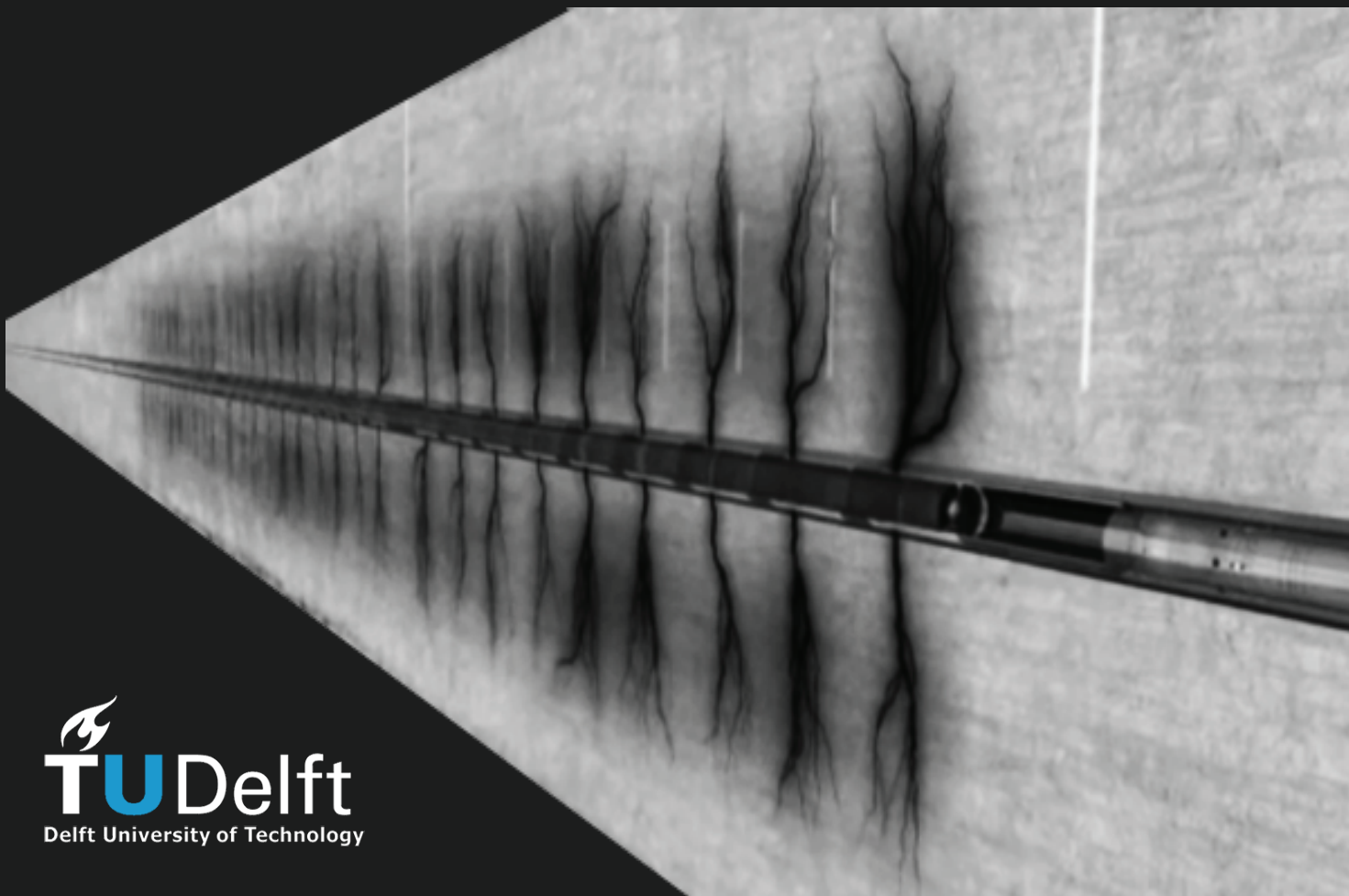

TU Delft
Delft University of Technology

Semi-analytical modeling of water injection under fracturing conditions by capturing effects of formation damage mechanisms to predict fracture propagation

By

Aditya Harsh

in partial fulfillment of the requirements for the degree of

Master of Science

in Petroleum Engineering

at the Delft University of Technology,

to be defended publicly on Thursday August 31, 2017 at 20:00 PM

Student Number:	4509390	
Supervisors:	Prof.dr.P.L.J Zitha	TU Delft
	Dr.Paul van den Hoek	TU Delft
	Dr.Hans de Pater	Fenix Consulting
Thesis committee:	Prof.dr.P.L.J Zitha	TU Delft
	Dr.Paul van den Hoek	TU Delft
	Dr.P.J. Vardon	TU Deflt
	Dr.Hans de Pater	Fenix Consulting

TU Delft

Supervisors:

Prof. dr. P.L.J.Zitha
P.L.J.Zitha@tudelft.nl
Professor and Chair Oil and Gas Production
Faculty of Civil Engineering and Geosciences
Department of Geotechnology
TU Delft

Dr. Paul van den Hoek
P.J.vandenHoek@tudelft.nl
Senior Research Associate Reservoir Geomechanics
Dept. of Geoscience and Engineering
TU Delft

Dr. Hans de Pater
hans.depater@fenixdelft.com
General Manager
Fenix Consulting
Delft

Other committee Members:

Dr. P.J. Vardon
P.J.Vardon@tudelft.nl
Assistant Professor
Faculty of Civil Engineering and Geosciences
Department of Geoengineering
TU Delft

Acknowledgement

I would like to express my deep gratitude to Dr. Hans de Pater, Mr. Josef Shaoul and Dr. Cas Berentsen at Fenix Consulting Delft for accepting me as a master thesis intern in the summer of 2016, and for their constant guidance. The last nine months has been an exciting journey into the fascinating world of fracturing, and I greatly appreciate the opportunity to work with such learned fracking professionals.

I would like to thank my daily supervisor at TU Delft, Dr.Paul van den Hoek for his continuous support and numerous fruitful discussions throughout my thesis. I would also thank my faculty advisor Prof. dr. Pacelli Zitha for his fruitful suggestions throughout the duration of my thesis. Without them this thesis would never have been possible.

I would like to thank all my colleagues at Fenix Consulting, Delft for their support and fun discussions during my time at Fenix Consulting. I would also like to thank my thesis committee member Dr.Phil Vardon for accepting to be part of the final assessment committee.

Finally, I would like to thank my dear parents, my sister and my friends who have always been by my side, especially during last two years on this exciting journey in the Netherlands.

TU Delft

Contents

Abstract

It is well known in the oil & gas industry that mature oil fields with a water drive produce increasing volumes of oily produced water which require treatment and efficient disposal. It is a major concern of all waterflood operations now in the industry, to adopt cost effective and environmentally sound water disposal systems. Re-injection into the subsurface has been chosen to be a potentially attractive option from environmental regulations view point, but to become the preferred alternative for produced water disposal, re-injection (PWRI) must also be economical and should not incur excessive risk in form of injectivity decline and damage to the formation.

In this study, a semi-analytical model of contaminated water injection under fracturing conditions, including the effects of damage mechanisms over time is developed, that couples the reservoir engineering and fracture mechanics aspects of the problem. The main features of this model are finite fracture conductivity, external filter-cake build-up on the fracture face, internal plugging at fracture tip by injected solids, backstress resulting from pore pressure inflation (poro-elastic stress), backstress resulting from formation cooling (thermo-elastic stress), and fracture propagation. The most important characteristic is that the fracture is of finite condutivity due to fracture fill up by total suspended solids and oils in injected water. This is what differentiates this model from conventional waterflood induced fracturing simulators.

This model is an extension to Koning's model for waterflood induced fracturing, where fracture is of infinite conductivity. This model is largely based on work of Hoek *et al.* for finite conductivity fracture. This model incorporates a rectangular fracture that fully penetrates a permeable layer bounded by impermeable layers on top and bottom. The fracture is surrounded by three elliptically shaped zones, formation damages caused are included which are critical for fracture propagation, and the primary objective is to predict long term fracture growth and well injectivity. The governing Equations for fracture propagation are based on four fundamental physical phenomena which are fluid leak-off from the fracture into the formation, fluid flow inside the fracture, poro-elastic and thermo-elastic backstress on the fracture face and fracture propagation into the formation.

The novelty of the new simulator is the ability to model waterflood induced fracture including all kinds of damage mechanisms, and accurately predict fracture propagation quickly.

List of Figures

List of Tables

1

Introduction

1.1. Motivation

Waterflooding is often applied to increase the recovery of oil or to maintain the reservoir pressure. It is well-established in the industry that water injectors are likely to be fractured either intentionally or unintentionally during the life of the well. Induced fracturing conditions is particularly common in low mobility reservoir conditions or in case of produced water re-injection (PWRI) where contaminated water is injected that could induce large fractures during field life. One of the common causes of induced fracturing is often cooling of hot formation rocks by cold sea water or cold produced water injection. Water injection generally leads to rapid decline in injectivity unless it is done under induced fracturing conditions. The theme of this thesis is water injection under fracturing conditions, which can be of significant benefit in the development plan of a field. It may enable lesser injection wells to be drilled either for recovery processes or waste disposal, which will lead to major savings in exploitation costs of the field.

In this thesis, a model is presented for predicting the performance of water injection wells under fracturing conditions in terms of fracture growth over time. The fracture can be both of infinite conductivity in case of clean water injection and finite conductivity in case of contaminated water injection (seawater, produced water etc). So, the basic difference between conventional waterflood fracturing and unfiltered water injection is that in the latter case, the fracture is no longer infinite anymore due to fracture fill up by the suspended particles in injected water during continued injection over time. This could potentially form internal filter-cake in invaded zone around fracture, external filter-cake on the fracture face and subsequently lead to formation of internal plug in the fracture. This reduces the effective permeability in the fracture and causes rise in the injection pressure, in order to maintain a constant injection rate. When the pressure at the fracture tip exceeds the fracture propagation pressure, the fracture extends in length.

This thesis discusses several aspects of simulating unfiltered water injection under fracturing conditions using both analytical and numerical models that couples the reservoir engineering and fracture mechanics concepts of the problem. The key features of the numerical model are finite conductivity fracture, external filter-cake build up on fracture face, internal plugging of fracture, poro-elastic backstress on fracture face resulting from pore pressure inflation and thermo-elastic backstress by formation cooling due to cold water injection. This model shows that the pressure drop over the finite conductivity fracture can lead to significant increase in the fracture volume without much increase in the injection pressure. As a result, more injected solids can be “accommodated” in the fracture. This creates a picture that large volumes of solids can be injected without much loss of injectivity unlike in conventional waterflood cases. The analytical model of fracture with tip plug emphasizes on an analytical approximation for fractures with tip plug permeability very close to permeability of formation surrounding the fracture[2].

1.2. Thesis Scope

The thesis investigates four fundamental physical phenomena which are the main research objectives as well. The objectives of the thesis are as follows: -

- Investigate fluid leak-off mechanism from an elliptical fracture into formation, and formulate the pressure solution around the fracture which will be elliptically symmetrical in infinite conductivity fracture and non-symmetrical for finite conductivity fracture.

- Investigate fluid pressure profile within the fracture with and without the presence of an external filter-cake of uniform permeability on fracture face, and formulate fracture pressure solution in the model.
- Investigation of Poro-elastic and thermo-elastic backstress on fracture wall resulting from pore pressure inflation and formation cooling respectively, and formulation of both analytical and numerical model to calculate the stress conditions.
- Investigation of fracture propagation condition for finite conductivity fracture and implementing it in the numerical model by analyzing the factors that influence fracture propagation pressure. The purpose is to predict the fracture growth over time under influence of formation damages, backstresses etc.
- Analyze different types of fracture tip propagation models and study their comparative behavior by varying key simulation parameters like solids loading, modulus of the formation, injection water temperature, constant filter-cake permeability etc.

1.3. Novelty of the Thesis

The work in this thesis is focused on building a semi-analytical model in MATLAB that investigates and produces reliable results of the four physical phenomena that occur during water injection under fracturing conditions, as mentioned in Section 1.2. This model is an extension of Koning's model for infinite conductivity fractures and focuses mostly on the concepts of paper[2] SPE 57385. The model also investigates and implements three different scenarios for fracture propagation which are primarily based on the fundamental concepts that, (i) All suspended solids must be accommodated by the fracture, and (ii) Tip-stress either remains constant or grows in time with increase in fracture length. In tip model 1, the fracture toughness K_{Ic} is constant whereas, in model 2 and 3, the model estimates an effective fracture toughness K_{Ic} that increases with fracture length X_f.

1.4. Thesis Outline

- Chapter 1 introduces the thesis and outlines its general motivation and objectives.
- Chapter 2 presents a state of the art review of the methods that have been incorporated in the past, their objectives and conclusions.
- Chapter 3 describes the investigation carried out to formulate and model pressure solution in and around the fracture especially for finite conductivity fractures. It also emphasizes on the effect caused by formation damages like external filter-cake build up, internal plugging etc.
- Chapter 4 describes the geomechanical concepts of poro-elastic backstress on fracture face due to the pressure field around the fracture. In addition, it also covers the thermo-elastic stress induced due to cold water injection.
- Chapter 5 describes the combined effect of fracture pressure, poro-elastic backstress, thermo-elastic backstress etc on fracture propagation pressure and models the fracture length growth over time by Newton Raphson iterative technique.
- Chapter 6 discusses all the analytical and numerical results produced for all four physical phenomena mentioned above.
- Chapter 7 presents the main conclusions of this research along with recommendations for further work.

2

Literature Review

2.1. SPE 14684, Waterflooding under Fracturing Conditions, Koning[1]

Koning's model focused on analytical modeling of waterflood induced fracturing from a single well in an infinite reservoir. The paper focused on propagation of the infinite conductivity fracture. Analytical expressions are incorporated in the model assuming maximum leak-off into the formation. Analytical calculation of poro-elastic stress changes on the fracture face induced by quasi-steady state elliptical pressure profile with elliptical discontinuities in fluid mobility are also included. Koning also presented a simple numerical model for calculating stress changes around a fracture and gave a comparative analysis of both models.

The basic assumptions in Koning's model are: -

- A vertical rectangular fracture extends laterally from a single well in an infinite reservoir. The shape of fracture is elliptical in horizontal cross-section.
- Fluid pressure drop along fracture can be neglected due it infinite conductivity of fracture.
- Rate of change of fracture volume is negligible compared to total leak-off rate because the total leak-off rate from fracture into reservoir is equal to injection rate from well into fracture.
- The propagation of the fracture is very slow w.r.t the velocity of transient pressure wave of fluid leak-off from fracture into the reservoir. It can be described as 2D-pseudo radial flow.
- The shape of the fronts separating the three zones-cold waterflooded zone, warm waterflooded zone and oil zone are elliptical which are confocal with fracture tips always.
- The thermo-elastic stress changes at fracture face are calculated under the assumption of an elliptical inclusion of uniform change in temperature based on the work of Perkins and Gonzalez[8].

The main difference in Koning's approach to the previous work done by Perkins and Gonzalez[8] was the methodology adopted in calculation of poro-elastic stresses on the fracture face.

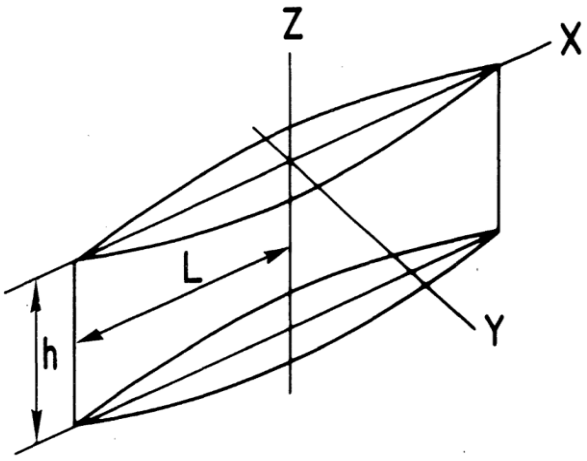

Fig 2.1: Geometry of fracture (wedge shaped)[1]

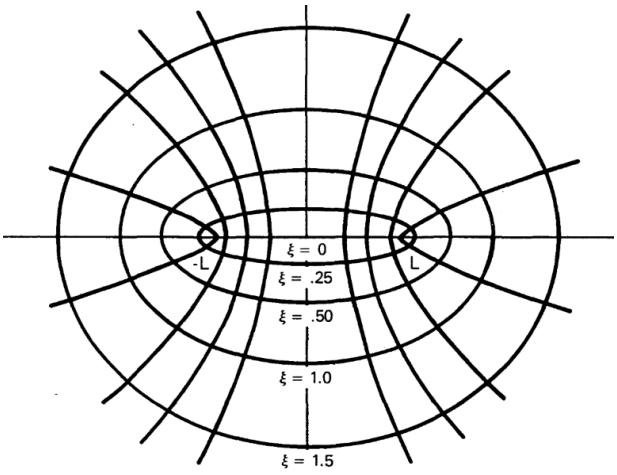

Fig 2.2: Elliptical coordinate system (ξ, η) with elliptical zones confocal with fracture tips[1]

The calculation of pressure solution for infinite conductivity fracture, poro-elastic stress and thermo-elastic stress are briefly explained in Chapter 3 and 4 of this thesis, and for detailed explanation Chapters 1, 2 and 3 of Koning's doctoral thesis[1] can be referred.

2.2. WF Model, Fenix Consulting

Koning[1] (1988) improved the poro-elastic stress calculation in his extension to the work of Perkins and Gonzales[8] (1978). WF (Water Frac) model build at Fenix Consulting is an analytical model based on Koning's work used to estimate fracture size and the associated stress changes. This model considers fracture growth in a reservoir, assuming that the fracture stays in the reservoir itself and all stress changes occur in the reservoir. The WF model basically simulates planar fracture propagation in a vertically confined isotropic uniform medium, where the incompressible and less mobile cold injected fluid displaces a zone of heated (cold fluid becomes warm when comes in contact with formation rocks) incompressible fluid in a piston like manner. So, each zone has its own mobility. The pressure drop in cold and warm zone are approximated as steady state and pressure transient is approximated in the reservoir fluid zone. The pressure solution estimated around the infinite conductivity fracture has three contributions from each zone based on their relative mobilities, extent of each flood front and the penetration depth of pressure transient in the oil zone (maximum drainage radius R_e).

The shape of cold and flood fronts is elliptical with major axis a and minor axis b. So, if V is the cooled (or flooded) zone volume, h is height of fracture and X_f *or* Lf $(in\ some\ cases)$ is fracture half-length then, the relation between the axis of ellipse and X_f is,

$$X_f = \sqrt{a^2 - b^2} \tag{2.1}$$

The focal points of ellipse are equivalent to the fracture half-length. Also, the volume of cooled (or flooded) zone is given by,

$$V = \pi abh \tag{2.2}$$

Combining both Equations 2.1 & 2.2 yields,

$$a = X_f\sqrt{\frac{1+\sqrt{1+c^2}}{2}} \quad , \quad b = X_f\sqrt{\frac{-1+\sqrt{1+c^2}}{2}} \quad , \quad c = \frac{2V}{\pi h X_f^2} \tag{2.3}$$

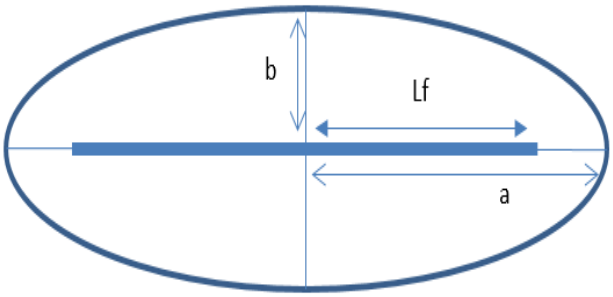

Fig: 2.3 Shape of cooled and flooded front

The fracture propagation criterion is based on a balance between the net effect of fracture pressure, the rock stress and fracture toughness (K_{Ic}). Since, the fracture is of infinite conductivity, the stress and pressure in fracture can be approximated to be constant. Therefore, fracture propagation equation for this case is,

$$P_f = \Delta P_{cold} + \Delta P_{flooded} + \Delta P_{oil} + P_{res,i} = \sigma_{min,i} + \Delta\sigma_T + \Delta\sigma_p + \frac{K_{Ic}}{\sqrt{\pi X_f}} \tag{2.4}$$

where, P_f = fracture pressure, ΔP = pressure drop in each zone, $\sigma_{min,i}$ = initial minimum horizontal stress, Δσ = stress changes, X_f = fracture length and K_{Ic} =fracture toughness.

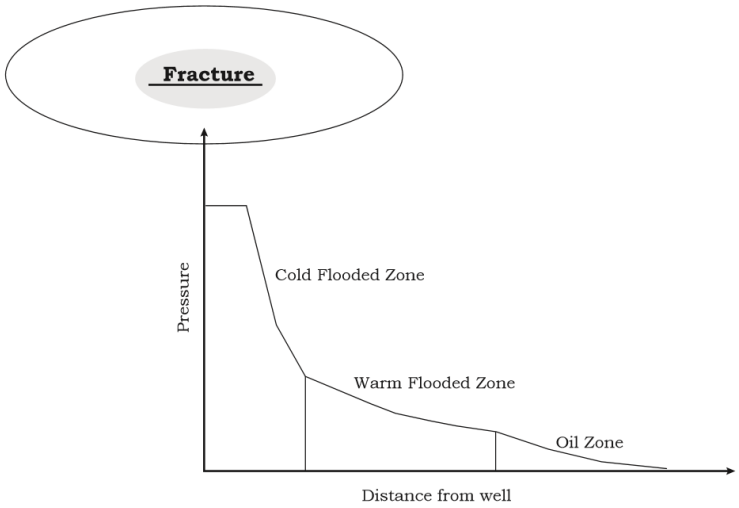

Fig 2.4: Schematic description of the WF model

The model in this thesis recreates Koning's model based on concepts in WF model and extends it for finite conductivity fracture case that requires estimation of poro-elastic backstress numerically. This thesis also investigates different fracture propagation criterion in both the analytical and numerical models.

2.3. SPE 36846, Simulation of PWRI under Fracturing Conditions[2]

This model is also an extension to Koning's model but now incorporates finite conductivity fracture. Due to injection of produced water, suspended solids in it can lead to formation damage in form of internal filter-cake build up in formation, external filter-cake build up on fracture face, internal plugging of fracture etc, which in turn leads to non-uniform fracture permeability. The fracture is assumed to fully penetrate the formation bounded by impermeable layers. As in WF model, there are elliptically shaped zones surrounding the fracture. The extent of these zones is calculated from the injected water volume and heat capacities of formation rock using Koning's approach. This model includes a simple damage model. The effect of damage because of PWRI above fracturing pressure includes,

- An external filter-cake on fracture face with uniform permeability (k_e).
- Internal plugging of the fracture over time due to continued injection.
- A damage zone around the fracture where smaller sized solids have penetrated. The boundary between damage zone and cold-water zone is calculated from the volume of deeply penetrated solids (user input), assuming that the saturation of deeply penetrating solids is equal to the residual oil saturation. This zone has not been included in this thesis as all the damage caused due to total suspended solids (TSS) have been assumed to either form an external cake on fracture face or accommodate as plug at the fracture tip.

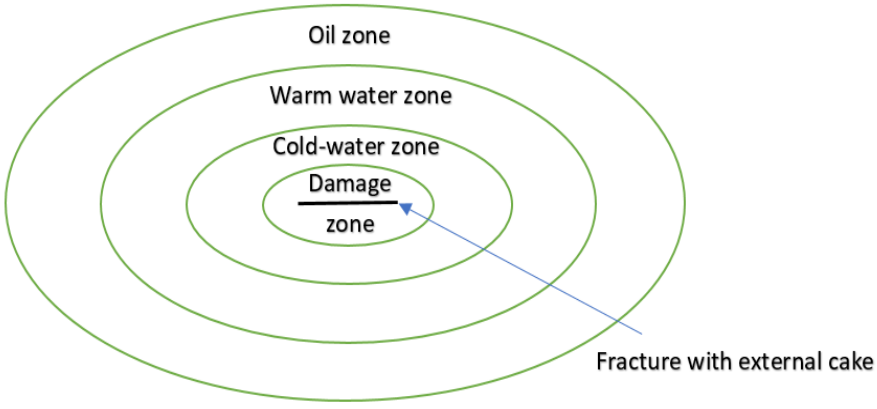

Fig 2.5: Multiple zones developed around the fracture during PWRI

As shown in the Figure2.5 above, at any given time there will be three distinct elliptical zones around the fracture (neglecting damage zone),

- The cold flooded zone is closest to fracture where water is mobile and oil is at residual saturation. The temperature in this region is equal to injected cold-water temperature T_{inj}.
- Warm water zone is ahead of cold zone but behind the flood front. The connate water is mobile and oil is at residual saturation. The temperature in this region is equal to initial reservoir temperature T_{res}.
- The oil or reservoir fluid zone is ahead of the flood front where both water and oil are mobile. The temperature in this region is also equal to initial reservoir temperature T_{res}.

This thesis investigates the above model and builds the finite fracture conductivity model both analytically and numerically in MATLAB using similar fundamentals. For completeness, infinite conductivity fracture equations and results are also included in Chapter 3 and Chapter 6 respectively. The main purpose of this thesis is to predict fracture growth over time during contaminated water injection (PWRI, seawater, etc.) under fracturing conditions.

3

Pressure Field Profile Model

3.1. Waterflood Induced Fractures

In the previous Chapter, we discussed the previous works done which have been used as the basis in this thesis. Over the last few decades, numerous papers have been published on various aspects of hydraulically induced fractures. It is widely accepted in the industry that to inject at economic rates, waterflood often occurs under induced fracturing conditions[9]. Induced fractures are typically open during injection and closed when well is shut-in which is different than a stimulation fracture such as frac-packs that remains always open. The trademark signature of induced fracturing can be observed on a plot between bottom hole pressure (BHP) and injection rate. Two different regions can be distinguished on this plot. At low rates, Darcy law is prevalent that gives a linear relation of proportionality between BHP and Q_{inj} whereas, when the fracturing pressure is reached, this relation is no longer valid and pressure becomes almost insensitive to the injection rate. The main reason for this is that extra injection rate gets accommodated by increasing the surface area of induced fracture. This is described in the graphs below.

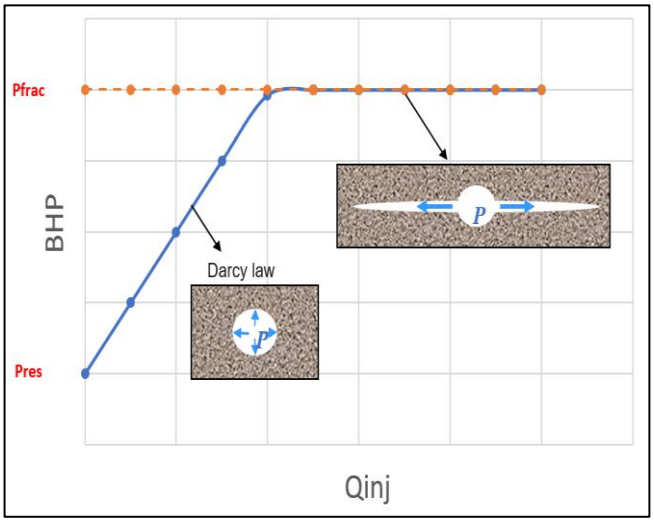

Fig 3.1: Trademark signature of Induced fracturing by water injection

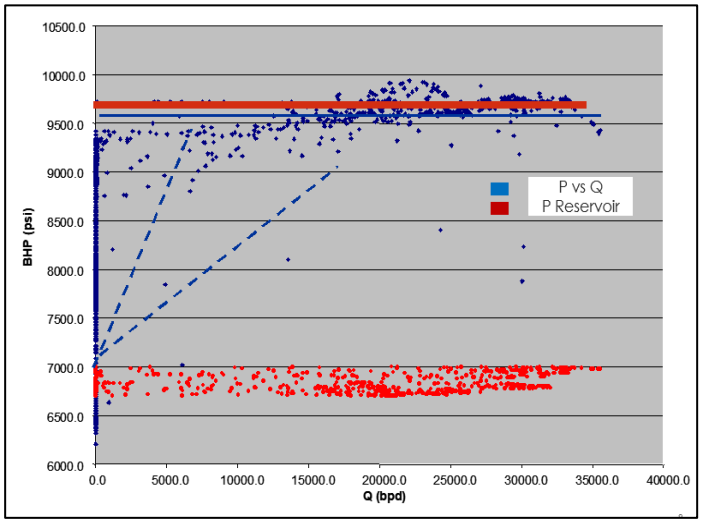

Fig 3.2: Gulf of Mexico field data example for Figure3.1 (adapted from Shell)

In this thesis, we focus on a typically low rate and viscosity of injected fluid as compared to a stimulation job. Also, the leak-off is maximum as there are no additives present to minimise leak-off. The injection well fracture tends to grow slower compared to in a stimulation job. A 2D flow pattern of leak-off in the plane of the reservoir is developed. This clearly means that the leak-off needs to be modelled in a separate way for induced fractures.

3.2. Infinite Conductivity Fractures – Elliptical Solution

Koning presented a comparative analysis of Carter's 1D leak-off solution[22] vs. 2D pseudo radial and elliptical leak-off solution (refer Chapter 3, page 119[1]). The analysis clearly demonstrates the importance of leak-off

modelling in prediction of fracture length. Hagoort[23] (1980) in his work on modelling the propagation of waterflood induced fractures, coupled a numerical reservoir simulator to an analytical fracture model. He observed that in an infinite reservoir, fracture length is always proportional to square root of time. Gringarten[24] also proposed an analytical expression for pressure solution for an infinite conductivity fracture given by,

$$\Delta p_D = \frac{1}{2}\sqrt{\pi t_D}\left\{\left(\mathrm{erf}\left(\frac{0.134}{\sqrt{t_D}}\right)+\mathrm{erf}\left(\frac{0.866}{\sqrt{t_D}}\right)\right)-0.067Ei\left(-\frac{0.018}{t_D}\right)-0.433E_i\left(-\frac{0.750}{t_D}\right)\right\} \tag{3.1}$$

where, $\Delta p_D = \frac{P_f - P_i}{q\mu}(2\pi kh)$, $t_D = \frac{\eta t}{X_f^2}$, $\eta = \frac{k}{\Phi\mu c}$

In this thesis, a model for pressure solution and flow distribution in and around a fracture is used in elliptical coordinate system given by,

$$x = X_f\, cosh\xi\, cos\eta \quad , \quad y = X_f\, sinh\xi\, sin\eta \tag{3.2}$$

The expression for steady state pressure profile surrounding infinite conductivity fracture used by Koning[1], was given by Muskat[21],

$$\Delta p(\xi) = \frac{q\mu}{2\pi kh}\ln\left(\frac{a_e + b_e}{X_f\, cosh\xi + X_f\, sinh\xi}\right) \tag{3.3}$$

where, $a_e = X_f \cosh(\xi e)$, $b_e = X_f \sinh(\xi e)$ are the major and minor axes respectively of the equi-pressure ellipse surrounding the elliptical zone affected by the change in pressure field. The pressure drops across each of the zones are obtained depending on position of equi-pressure ellipse using the following equations,

- When both cold and flood fronts have surpassed the equi-pressure ellipse i.e. $b_e < b_c < b_F$(b_e = minor axis of arbitrary ellipse, b_C = minor axis of cold zone ellipse boundary and b_F = minor axis of flood front ellipse boundary), then pressure drops are given by,

$$\Delta p_1(\xi) = \frac{i_w}{2\pi\lambda_1 h}\ln\left(\frac{a_c + b_c}{X_f\, cosh\xi + X_f\, sinh\xi}\right) \tag{3.4}$$
$$\Delta p_2(\xi) = \frac{i_w}{2\pi\lambda_2 h}\ln\left(\frac{a_F + b_F}{a_c + b_c}\right)$$
$$\Delta p_3(\xi) = \frac{i_w}{2\pi\lambda_3 h}\ln\left(\frac{2R_e}{aF + b_F}\right)$$

- When the waterflood front has surpassed equi-pressure ellipse but not cold/thermal front i.e. $b_c < b_e < b_F$, then

$$\Delta p_2(\xi) = \frac{i_w}{2\pi\lambda_2 h}\ln\left(\frac{a_F + b_F}{a_C + b_c}\right) \tag{3.5}$$
$$\Delta p_3(\xi) = \frac{i_w}{2\pi\lambda_3 h}\ln\left(\frac{2R_e}{a_F + b_F}\right)$$

- When both the fronts are behind the equi-pressure ellipse i.e. $b_c < b_F < b_e$ then,

$$\Delta p_3(\xi) = \frac{i_w}{2\pi\lambda_3 h}\ln\left(\frac{2R_e}{a_F + b_F}\right) \tag{3.6}$$

In this model, for infinite conductivity fractures, the pressure field around the fracture has elliptical symmetry mainly because of uniform pressure within the fracture. So, this pressure is only dependent on coordinate ξ, and not η. The formulated steady state pressure distribution for three zones of different mobility is given by,

$$\begin{aligned} p(\xi) &= p_{res} + \Delta p_1(\xi)\ , \qquad 0 \le \xi \le \xi_1 \\ &= p_{res} + \Delta p_2(\xi)\ , \qquad \xi_1 \le \xi \le \xi_2 \end{aligned} \tag{3.7}$$

$$= p_{res} + \Delta p_3(\xi) \ , \qquad \xi_2 \le \xi \le \xi_3$$
$$= p_{res} \qquad , \qquad \xi \ge \xi_3$$

In the model, using the assumption that pressure front grows elliptically outward w.r.t slowly growing fracture, an effective time dependent exterior radius R_e, is defined from the late-time approximation of the fully transient solution by substituting,

$$R_e(t) = 1.5\sqrt{\eta t} \tag{3.8}$$
$$\xi_3(t) = \ln\left(\frac{3\sqrt{\eta t}}{X_f}\right) = \ln(\frac{2R_e(t)}{X_f})$$

where, $\eta = \frac{k_3}{\Phi \mu_3 c_3}$ is hydraulic diffusivity derived from reservoir and fluid properties of zone 3.

The pressure profile $\Delta p(\xi)$ satisfies the Laplace Equation,

$$\frac{\partial^2}{\partial \xi^2}\Delta p(\xi) = 0 \tag{3.9}$$

with boundary conditions at each elliptical zone boundary given by,

$$\Delta p_1(\xi_3) = 0, \tag{3.10}$$
$$\Delta p_1(\xi_1) = \Delta p_2(\xi_1),$$
$$\Delta p_2(\xi_2) = \Delta p_3(\xi_2)$$

In addition, using Darcy's law, we get the following boundary conditions,

$$\frac{k_1}{\mu_1}\frac{\partial}{\partial \xi}\Delta p_1(\xi = \xi_1) = \left(\frac{k_2}{\mu_2}\right)\frac{\partial}{\partial \xi}\Delta p_2(\xi = \xi_1) \tag{3.11}$$
$$\frac{k_2}{\mu_2}\frac{\partial}{\partial \xi}\Delta p_2(\xi = \xi_2) = \left(\frac{k_3}{\mu_3}\right)\frac{\partial}{\partial \xi}\Delta p_3(\xi = \xi_1)$$

Using the above equations, the pressure field profile can be deduced as,

$$\Delta p_1(\xi) = \frac{i_w}{2\pi\lambda_1 h}(\xi_1 - \xi) + \frac{i_w}{2\pi\lambda_2 h}(\xi_2 - \xi_1) + \frac{i_w}{2\pi\lambda_3 h}(\xi_3 - \xi_2) \tag{3.12}$$
$$\Delta p_2(\xi) = \frac{i_w}{2\pi\lambda_2 h}(\xi_2 - \xi) + \frac{i_w}{2\pi\lambda_3 h}(\xi_3 - \xi_2)$$
$$\Delta p_3(\xi) = \frac{i_w}{2\pi\lambda_3 h}(\xi_3 - \xi)$$

where, subscripts i = 1, 2 & 3 in $\Delta p_i(\xi)$ represent fluid pressure change in cold flooded zone, warm flooded and oil zone respectively. The above equations are generalised under the conditions that fronts separating each zone are ellipses confocal with fracture tips and the fluid mobilities are uniform within each zone. The corresponding stress changes are illustrated in Chapter 4 and Appendix B in detail.

3.3. Damage Mechanisms

The main agents responsible for damage caused are total suspended solids (TSS) in produced water, salty seawater, oil in water (OIW) etc. TSS is arguably the most damaging factor present in the injection stream mainly due to corrosion along with bacteria present, scaling effect etc adding significant solid content to the contaminated produced water by the time it reaches the sand face during injection. The damages could be due to solids deposition in fracture, on fracture face, solids getting trapped internally in formation, solids travelling freely in the fracture etc. It depends primarily on the TSS to pore throat ratio. In this thesis, the following formation damages have been discussed,

Internal Filter-cake: It is caused because of very small sized particles that deposit internally in the adjacent formation to the fracture. These particles form a damage zone around the fracture as shown in Figure2.5 and reduce the adjacent formation porosity. Also, the permeability of the damage zone is significantly low.

But, the magnitude of damage caused by Internal Filter-cake formation is much less compared to the pressure decline caused due to formation damages in the fracture in form of external filter-cake build-up on fracture face and internal Plug evolution at fracture tip. The formulation of damage or impaired zone can be done in following way[2],

$$\xi_0 = 0.5 \operatorname{asinh}\left(\frac{2V_s}{\pi X_f^2 h}\right) \tag{3.13}$$

where, ξ_0 is the elliptical coordinate of the damage zone adjacent the fracture and before the cooled water zone, volume $V_s = \frac{f}{\emptyset_{Sor}} W_i, f$ is the fraction of TSS that penetrates deeply in the adjacent formation and, Wi is the total water volume injected at that time.

External Filter-cake: It is build up on fracture face mainly due to particles that are large. These particles tend to deposit at fracture face and form a primary damage zone on the fracture face. Generally, the external filter-cake composition is highly complex due to presence of solids, OIW, bacteria, scale, debris etc due to which, the pressure drop is much higher compared to internal Filter-cake. In this model, external filter-cake is assumed to have uniform permeability (k_e). The filter-cake thickness is generally larger near the fracture mouth or wellbore and decreases in width towards the fracture tip. This is because the total suspended solids and oil in injected water accumulates throughout the fracture face in proportion to the fluid volume that leaks off. The flow at fracture mouth is greater than tip due to leak-off, which causes more erosion near the wellbore leading to larger external filter-cake thickness at the mouth (b_0). So, in this model the external filter-cake is assumed to have an elliptical shape given by[2],

$$b(x) = b_0 \sqrt{1 - \left(\frac{x}{X_f}\right)^2} \tag{3.14}$$

where, b is the external filter-cake thickness and x is the coordinate on fracture face. In elliptical coordinates, it can be written as,

$$b(\eta) = b_0 \sin(\eta), 0 \leq \eta \leq (\frac{\pi}{2}) \tag{3.15}$$

The filter-cake thickness is calculated from volume of total suspended solids in injected water that remains in the fracture surface area given by,

$$TSS.V_{inj} = \pi b_0 X_f h \tag{3.16}$$

It is to be noted from Equation (3.14) that, in case of an infinite conductivity fracture such a thickness profile will lead to uniform pressure drop over the filter-cake because pore pressure distribution is as given in Equation (3.12). But, the main focus of this thesis is fracture with finite conductivity that requires internal plugging of the fracture as well.

Internal Plugging at fracture tip: Filter-cake damage w.r.t the fracture occurs not only on the fracture face but also inside the fracture at fracture tip. It is illustrated in Figure3.3. In this model, the internal plug is formed once the external filter-cake starts building up on fracture face and no newly injected solids can penetrate adjacent formation. This is because of conventional filtration theory. Since, the induced fracture during water injection grows slowly, this leads to a situation in which the interior of the fracture starts getting filled (partial plugging) by TSS and oil in injected water with time. Also, if the external filter-cake thickness tends to be large at fracture mouth, causing a small gap for fluid to enter through, then particles at the mouth get displaced to the tip[4]. So, tip plug forms by impurities in injected stream as well as particles eroded from filter-cake[4]. Therefore, the fracture is no more of infinite conductivity. The computation of plug length and volume evolution is carried out in Chapter 5 using following volume balance of solids injected,

$$V_{solids}(t) = TSS.i_w.t = \pi h \int_{X_{fu}}^{X_f} X_f(x,t)\ w(x,t)\ dx \tag{3.17}$$

where, $w(x,t)$ is the fracture width profile, $x = X_{fu}$ is the unplugged length.

The main challenge in modelling a finite conductivity fracture is that the fracture permeability profile is unknown due to the formation of internal plug near fracture tip. The main principle for calculation of fracture conductivity in this model is that at any given time, the volume of the fracture is equal to total volume of injected solids. The formulation of fracture permeability profile is done in next section.

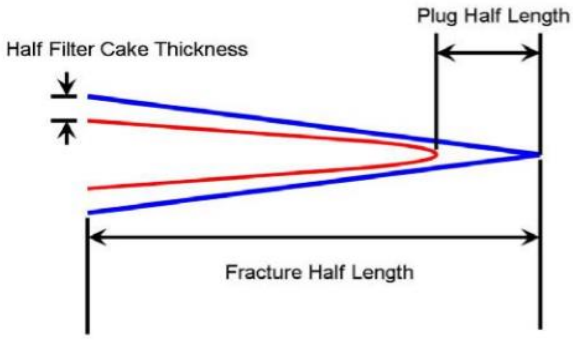

Fig 3.3: Schematic of filter-cake thickness and internal plug length formed[4]

3.4. Finite Conductivity Fractures – Elliptical Solution

Finite Conductivity fracture is the main scope of this Chapter. A semi-analytical model has been developed to solve for the pressure field in and around the finite conductivity fracture. Finite Conductivity fractures can be defined accurately using the fracture permeability profile explained below.

Fracture Permeability profile: In this model, due to elliptical profile the leak-off is minimum near fracture tip. So, it is expected that injected solids/oil droplets will fill the tip area first. The fracture permeability tends to decrease from fracture mouth to the tip. This is because the permeability distribution taken has an impermeable plug behind the fracture tip along with an infinite conductivity unplugged area behind the plug up to fracture mouth (Figure3.3). This is given by a two-step permeability profile step-function[2],

$$k_f(\eta) = \begin{cases} k_{f1}\ , & \eta_{12} \le \eta \le (\frac{\pi}{2}) \\ k_{f2}\ , & 0 \le \eta \le \eta_{12} \end{cases} \tag{3.18}$$

This fracture permeability profile in Equation (3.18) is used to calculate the Fourier coefficients by building a linear set of Equations of the form AX = B, which is discussed later. In this model with an impermeable tip plug, the plug length is iterated along with iteration of fracture length for fracture propagation scenario which is discussed in detail in Chapter 5. Also, in case of a fracture with uniform permeability, the fracture permeability would be iterated until all injected solids/oil droplets are accommodated by the fracture. This case has not been included in the model, but can be referred to in work of Hoek *et al.*[2].

In this model, the pressure drop over the fracture will be non-zero that will disturb the elliptical symmetry of pressure field around the fracture as mentioned in (3.2). So, for a finite fracture the pressure profile $\Delta p(\xi)$ must satisfy the fully Laplace equation instead of Equation (3.9). This is because the pressure field now depends on both ξ and η coordinates. The full Laplace equation is given by,

$$\left(\frac{\partial^2}{\partial \xi^2} + \frac{\partial^2}{\partial \eta^2}\right) \Delta p(\xi, \eta) = 0 \tag{3.19}$$

The pressure solution is periodic in η with period as π. Therefore, it is expressed in form of a Fourier series given by,

$$\Delta p_1(\xi) = \frac{i_w}{2\pi\lambda_1 h}(\xi_1 - \xi) + \frac{i_w}{2\pi\lambda_2 h}(\xi_2 - \xi_1) + \frac{i_w}{2\pi\lambda_3 h}(\xi_3 - \xi_2) + \frac{\mu i_w}{2\pi k h}\sum_{m=1}^{\infty}\{a_{1m}\cosh[2m(\xi_1 - \xi)] + b_{1m}\sinh[2m(\xi_1 - \xi]\}\cos[2m\eta]]$$

$$\Delta p_2(\xi) = \frac{i_w}{2\pi\lambda_2 h}(\xi_2 - \xi) + \frac{i_w}{2\pi\lambda_3 h}(\xi_3 - \xi_2) + \frac{\mu i_w}{2\pi k h}\sum_{m=1}^{\infty}\{a_{2m}\cosh[2m(\xi_2 - \xi)] + b_{2m}\sinh[2m(\xi_2 - \xi]\}\cos[2m\eta]]$$

$$\Delta p_3(\xi) = \frac{i_w}{2\pi\lambda_3 h}(\xi_3 - \xi) + \frac{\mu i_w}{2\pi k h}\sum_{m=1}^{\infty}\{b_{3m}\sinh[2m(\xi_3 - \xi]\}\cos[2m\eta]] \quad (3.20)$$

The above equations also satisfy boundary conditions given by Equations (3.10 & 3.11). Also, μ and k are reference viscosity and permeability respectively. The coefficients $a_{1m}, a_{2m}, b_{1m}, b_{2m}$ *and* b_{3m} can be related using the boundary conditions in following way,

$$\left(\frac{k_1}{\mu_1}\right)b_{1n} = \left(\frac{k_2}{\mu_2}\right)b_{2n}\cosh[2n(\xi_2 - \xi_1)] \quad (3.21)$$

$$\left(\frac{k_2}{\mu_2}\right)b_{2n} = \left(\frac{k_3}{\mu_2}\right)b_{3n}\cosh[2n(\xi_3 - \xi_2)]$$

$$a_{1n} = b_{2n}\sinh[2n(\xi_2 - \xi_1)]\ , a_{2n} = b_{3n}\sinh[2n(\xi_3 - \xi_2)]$$

In order to solve for the five coefficients, a system of linear Equations of the form AX = B is developed to first solve for coefficient b_{1m} of the Fourier sum in MATLAB. It gives the rest four coefficients from Equation (3.21). The detailed calculations are presented in Appendix A. The solution of this linear set of Equations requires finite fracture permeability profile which was discussed in section 3.3.

3.5. Fracture Pressure Profile – Elliptical Solution

The fracture (viewed from top) is treated as a 1D line with very small width at fracture mouth that decreases elliptically to zero at fracture tip. This 1D line is divided into uniform grids of length DX. The pressure inside the fracture is estimated at centre of each of this grid cells i.e. in discretized manner, pressure is evaluated at each i^{th} segment from 1 to N's as depicted below.

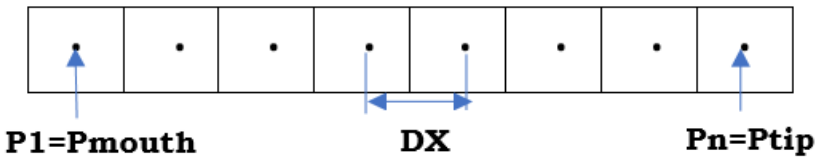

In order to derive the equation for fracture pressure, the fluid volume balance locally in the fracture is done. The local fluid volume balance in the fracture is achieved under the condition that fluid flow rate along the fracture (along x) is equal to the (constant injection flow rate (i_w) – leak-off flow along the fracture face). The balance Equation for it is mentioned in Appendix A both with and without external filter-cake on fracture face. In the absence of external filter-cake we get,

$$\Delta pf(\eta) = \Delta p1(\xi = 0, \eta)\ , 0 \le \eta \le \left(\frac{\pi}{2}\right) \quad (3.22)$$

Equation (3.22) clearly shows that the fracture pressure depends only on coordinate η at ξ=0 i.e. at fracture face. So, in case of an infinite conductivity fracture, a constant fracture pressure profile is expected from $x = 0\ to\ X_f$ *or* $\eta = \pi/2\ to\ 0$. On the other hand, in case of a finite conductivity facture with fracture permeability profile as given in Equation (3.18), a sharp pressure drop is expected at transition area from unplugged to plugged part i.e. at $x = X_{fu}$. The fracture pressure profile in presence of an external filter-cake built on fracture face with thickness $b(x)$ *or* $b(\eta)$ in elliptical coordinates is given by,

$$\Delta p_f(\eta) = \Delta p_1(\xi = 0, \eta) - \left[\left(\frac{k_1}{k_e}\right)\left(\frac{b_0}{X_f}\right)\left(\frac{\partial \Delta p_1(\xi, \eta)}{\partial \xi}\right)\right] at\ \xi = 0, 0 \le \eta \le \left(\frac{\pi}{2}\right) \quad (3.23)$$

The presence of external filter-cake changes the linear set of equations developed in the coefficients of the Fourier sum, which have been described in detail in Appendix A from Equations A.11 to A.15.

4

Poro-Elastic and Thermo-elastic Stress Models

In this Chapter, the factors that affect the fracture propagation pressure using the similar wedge-shaped fracture geometry (Figure2) is investigated. The pressure field solutions derived in Chapter 3 are used to estimate the poro-elastic backstress effect on fracture face due to pore pressure inflation. Also, the thermo-elastic stress due to formation cooling is evaluated.

4.1. In-situ Stress

The underground formations are in confined state and under stress conditions. In-situ stress underground is the result of overburden stress due to mass of rock and pore fluid. In general coordinate, it has six components (3 stress and 3 shear components). Figure4.1 illustrates the local state of stress translated into three principal stress (σ_1, σ_2, σ_3) for an element of the formation. The components are σ_1 which is often vertical and maximum in a normal tectonic regime ($\sigma_1 > \sigma_2 > \sigma_3$), σ_2 is the maximum horizontal stress and σ_3 is the minimum horizontal stress. Such induced fractures open against the minimum horizontal stress σ_3 i.e. formation breaks out along σ_3 (perpendicular to fracture) and fracture propagates in other two directions, in the plane of greatest and intermediate stresses. So, that is the reason why in deep reservoirs we often have vertical fractures induced as σ_3 is horizontal and overburden (σ_1) is maximum whereas, in shallow reservoirs we get, horizontal fractures induced as σ_3 is vertical and overburden is minimum. The latter is often common in tectonically relaxed regions.

The principal stresses are generally compressive, anisotropic and heterogeneous in nature. This implies that compressive forces acting on the rocks are not equal and vary in magnitude depending on their direction of orientation. So, the magnitude and direction of principal stresses are key factors in net pressure calculation for fracture propagation, fracture widening, shape of the fracture, vertical extent of the fracture, etc. In this model, we assume elliptical shape and a rectangular fracture, so focus is only on calculation of minimum horizontal stress (σ_3) magnitude in a normal tectonic regime.

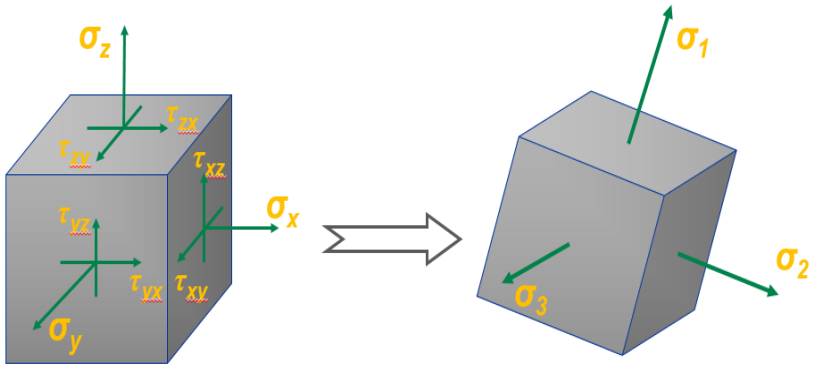

Fig 4.1: In-situ stress components (adapted from Shell)

4.2. Poro-elasticity and Calculation of Poro-elastic Stress

Poro-elasticity is a term used to describe the interaction between fluid flow and deformation of solids under external load within a porous media. It results from increase in pore pressure in the formation around fracture due to water injection. The pore pressure increase around the fracture leads to increase in backstress and propagation pressure. This pore pressure increase was evaluated in Chapter 3. In this

Chapter, we model the reaction to this change in pore volume and pressure in form of elastic deformation of rocks or poro-elastic backstress mechanism.

The principal mechanism of poro-elasticity says that, the stress around the fracture will increase proportional to the pressure increase around the injection well w.r.t. P_{res} prior to injection. In equation form it can be written as,

$$\Delta\sigma_h = A_p * \Delta p \tag{4.1}$$

$$A_p = \alpha_B * \left(\frac{1-2\nu}{1-\nu}\right) \tag{4.2}$$

where, α_B = Biot coefficient, ν = Poisson's ratio, and A_p = Poro-elastic constant typically of the order of 0.5-0.7 (bar/bar). Equations 4.1 and 4.2 are valid under the assumption that overburden stress doesn't change during injection. The $\Delta\sigma_h$ also depends on ratio between pressure penetration front into the reservoir and fracture length[1]. In specific terms, the larger the fracture and smaller the penetration, the $\Delta\sigma_h$ is "small" whereas, smaller the fracture and larger the penetration, $\Delta\sigma_h$ is "large". This model largely deals with the latter case. The approach in the model to solve stress fields have been taken from Chapter 2 of Koning's work. The main results of Koning's stress model which have been incorporated in this model are,

- When the reservoir pressure increases, the rock matrix tries to expand which results in increase of poro-elastic horizontal stress $\sigma_{h,min}$.
- The change in total horizontal stress for a given wellbore pressure and/or temperature depends on the ratio of reservoir height and penetration depth of pressure and/or temperature front ($h/2R_e$). A comparative analysis of analytical and numerical results of this model vs Koning's results for different $h/2R_e$ ratios, have been tabulated in Chapter 6.
- When reservoir is cooled upon cold water injection, the rock matrix tends to contract which results in decrease of thermo-elastic horizontal stress σ_{yT}.

The net effect of poro- and thermo-elastic stress changes on fracture face given by Koning[1] is,

$$\sigma_{h,net} = \sigma_{h,initial} + \Delta\sigma_{yT} + \Delta\sigma_{yT} \tag{4.3}$$

where, $\sigma_{h,initial}$ is initial horizontal stress.

This equation is then used for fracture propagation modelling. The analytical expressions of poro-elastic stress changes have been discussed in Appendix 3-A of Koning's thesis[1]. In this model, the main focus is put on numerical modelling of stress changes at the fracture wall. In this method, the reservoir is divided into cartesian grid blocks or small adjacent parallelepipeds as shown in Figure4.2. The pressure in the field evaluated in Chapter 2 is constant within each grid block. The principle of superposition is used to calculate the net stress on fracture face by summing up the contributions from all grid blocks.

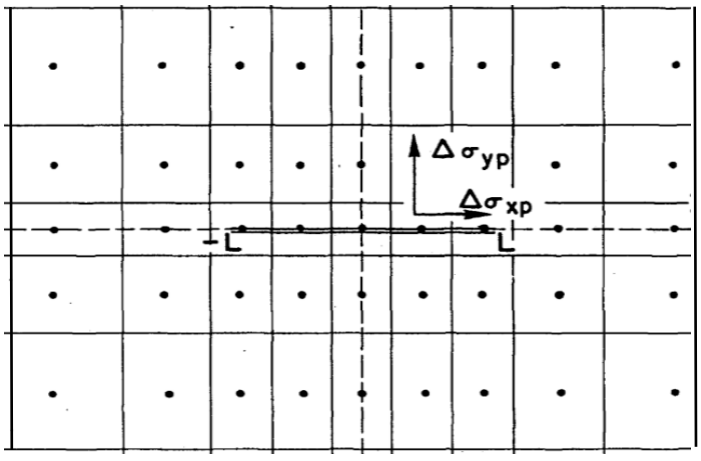

Fig 4.2: Schematic representation of grid block distribution for poro-elastic stress calculation[1]

The poro-elastic backstress induced by a pressure field change $\Delta p(\vec{x})$ can be expressed using the Goodier potential[1] $\Phi(\vec{x})$. In generalized manner, the equation in cartesian coordinates (x, y, z) for the Goodier displacement potential is given by,

$$\left(\frac{\partial^2}{\partial x^2}+\frac{\partial^2}{\partial y^2}+\frac{\partial^2}{\partial z^2}\right)\emptyset \;=\; -m\,\Delta p \tag{4.4}$$

The solution for the above equation given by Koning[1] is,

$$\emptyset = \frac{m}{4\pi}\int dx\,dy\,dz\;\;\Delta p(x,y,z)\frac{1}{R} \tag{4.5}$$

Where, R is given by,

$$R = [(x-x')^2+(y-y')^2+(z-z')^2]^{0.5} \tag{4.6}$$

Therefore, on solving Equation 4.4 the stresses are given by,

$$\sigma_{ijp} = Ap * \left\{\frac{1}{4\pi}\int dx\,dy\,dz\,\Delta p(x,y,z)\;\frac{\partial^2}{\partial xi\;\partial xj}\;\left(\frac{1}{R}\right)+\Delta p\;\;\delta_{ij}\right\} \tag{4.7}$$

where, δ_{ij} is the Kronecker delta. The detailed procedure is outlined in Appendix 3-B[1].

In Figure4.2, the coordinate space has been divided into parallelepipeds with edges of length $2a_1, 2a_2 \& 2a_3$ in the x, y, z directions respectively. In this model, equal size grids have been used which means the edges are of equal length. Also, as mentioned above Δp is constant within each parallelepiped. This means equation 4.7 becomes,

$$\sigma_{ijp} = \frac{Ap}{4\pi}\left\{\sum_{x,y,z}\Delta p(x,y,z)\int_{x-a_1}^{x+a_1}dk_1\int_{y-a_2}^{y+a_2}dk_2\int_{z-a_3}^{z+a_3}dk_3\frac{\partial^2}{\partial k_i\,\partial k_j}[(x-k_1)^2+(y-k_2)^2+(z-k_3)^2]^{-\left(\frac{1}{2}\right)}\right\} + Ap(\Delta p(x,y,z)\delta_{ij}) \tag{4.8}$$

On solving the above integrals, we get[1]

$$\sigma_{ijp} = \frac{Ap}{4\pi}\left\{\sum_{x,y,z}\Delta p(x,y,z)\int_{a_1}^{a_1}dk_1\int_{a_2}^{a_2}dk_2\int_{a_3}^{a_3}dk_3\frac{\partial^2}{\partial k_i\,\partial k_j}[(x_0-x-k_1)^2+(y_0-y-k_2)^2+(z_0-z-k_3)^2]^{-\left(\frac{1}{2}\right)}\right\} + Ap(\Delta p(x_0,y_0,z_0)\delta_{ij}) \tag{4.9}$$

where, (x_0, y_0, z_0) is a source point on the fracture and (x, y, z) is a field point. The integral is calculated analytically[16]. The results are given in Appendix B of this thesis.

In Equation (4.9), a volume integral needs to be computed. In case of a dynamic fracture, this volume integral will be calculated for each iteration until fracture length converges (Chapter 5). This makes this computation a time-consuming affair. Also, the numerical accuracy of this integral relies on the accurate estimation of pressure field around the fracture (Chapter 3) at field point (x, y, z) due to presence of singularity in the integrand[7]. In this model, it is assumed that the pressure at each grid block is constant over the height of the reservoir. So, the summation over z direction is neglected and is replaced by $h/2, h/4, h/5$ etc. where, h is the reservoir height. Also, the only stress component of interest is the one perpendicular to fracture surface $\sigma_{yp}(\vec{x})$ induced by pore pressure inflation (Appendix B). The stress is fundamentally expected to be greatest at centre of entire fracture $2X_f$, and least at the tips.

4.3. Thermo-elasticity and Calculation of Thermo-elastic Stress

Perkins and Gonzalez[13] (1985) calculated the thermo-elastic backstress $\Delta\sigma_{yT}$ for an elliptical disc with uniform change in temperature. Their analytical model assumed the elliptical temperature discontinuity confocal with the fracture tips. A similar model is built for $\Delta\sigma_{yT}$ calculation in this thesis. The thermo-elastic

stress for cold water injection, unlike poro-elastic stress has a negative effect due to formation cooling (rock contraction) and thus, reduces the net backstress on fracture face. The principal mechanism of thermo-elasticity says that, the stress around the fracture will increase proportional to the temperature difference between injection fluid temperature and initial reservoir temperature. In equation form it is given by,

$$\Delta\sigma_{yT} = A_T.\Delta T \tag{4.12}$$

$$A_T = \frac{E\ \alpha T}{1-\nu} \tag{4.13}$$

where, E = Young's modulus (bar), αT = linear thermal expansion coefficient (1/℃), and $\Delta T = T_{inj} - T_{res}$ (℃).

The thermo-elastic constant A_T typically has value of 1 bar/$^{\circ}$C for medium strength rock. It is proportional to Young's modulus which indicates that in soft rocks the thermo-elastic effect is lesser than hard rocks. In this model, we use Perkins and Gozalez's[13] expressions for $\Delta\sigma_{yT}$ calculation. Firstly, following dimensionless quantities are defined,

$$\Delta\sigma_{xTD} = \frac{\Delta\sigma_{xT}}{AT.\Delta T} \quad , \quad \Delta\sigma_{yTD} = \frac{\Delta\sigma_{yT}}{AT.\Delta T} \tag{4.14}$$

Using Equations (4.12) to (4.14), for the elliptical inclusion of uniform ΔT, the thermo-elastic stresses in x and y are given by[1],

$$\Delta\sigma_{yTD} = \frac{e_c}{1+e_c} + \frac{(1+e_c)^{-1}}{1+0.5[1.45(h_D)^{0.9}+0.35(h_D)^2][1+(e_c)^{0.774}]} \tag{4.15}$$

$$\Delta\sigma_{xTD} = \frac{1}{1+e_c} + \frac{e_c(1+e_c)^{-1}}{1+[1.45(h_D)^{0.9}+0.35(h_D)^2][1+(1-e_c)^{1.36}]} \tag{4.16}$$

where, $h_D = \frac{h}{2b_c}, e_c = \frac{b_c}{a_c}$ with a_c, b_c being the major and minor axes respectively of temperature front.

In Appendix B, the detailed calculation of major and minor axis of elliptical temperature front is discussed using heat and volume balance. The poro-elastic stress $\Delta\sigma_{yP}$ and thermo-elastic stress $\Delta\sigma_{yT}$ discussed in this Chapter, both will have significant impact on the fracture propagation pressure (Injection pressure) and fracture size. This will be discussed in Chapter 5.

Combining section 4.2 and 4.3, we get the overall effect of pore pressure and temperature on reservoir stress changes given in elliptical coordinates by,

$$\sigma_{min}(\xi,t) = \sigma_{min,i}(\xi,0) + \Delta\sigma_{yT} + \Delta\sigma_{yP} \tag{4.17}$$

5

Fracture Propagation Model

In previous Chapters, the factors that influence fracture propagation pressure have been discussed. In this Chapter, the fracture propagation criterion is investigated and different approaches are discussed to model fracture propagation pressure and predict fracture length after continued constant rate water injection over time.

5.1. Stages of Fracturing

The fracture initiation pressure must exceed the sum of minimum horizontal stress ($\sigma_{h,min}$) and tensile stress of formation rock for rock to breakdown. A sudden drop in measured pressure on surface is indicative of fracture initiation. Fracture closure pressure is lesser and is observed when injection is stopped and fracture starts to close. The minimum principal compressive stress ($\sigma_{h,min}$) controls the fracture closure pressure generally. In most cases, the fracture propagation pressure lies between both the pressures. The fracture propagates at slightly lesser pressure than breakdown pressure and remains constant for an infinite conductivity fracture as long as injection is done at constant rate. But, in case of a plug formation for finite conductivity fractures, the pore pressure and stress in fracture is now a function of x coordinate.

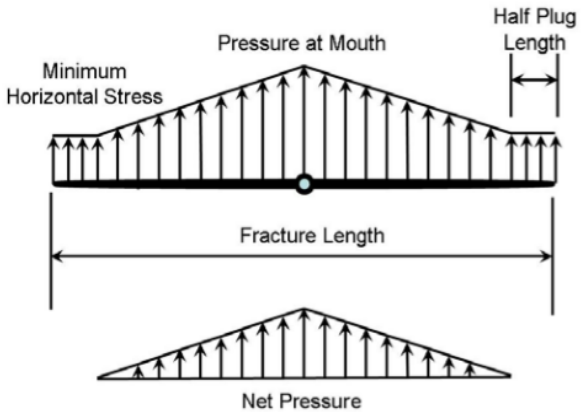

Fig 5.1: Schematic representation of pressure and stress distribution in plugged fracture[4]

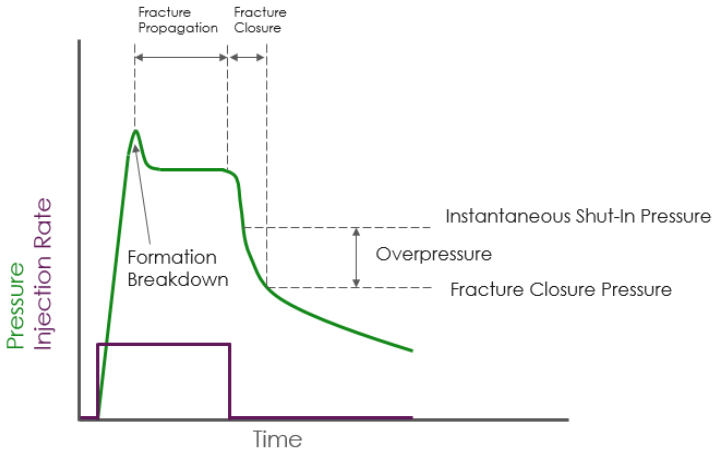

Fig 5.2: General description of Stages of fracturing (adapted from Shell)

The pressure inside the fracture is greatest at the fracture mouth (near wellbore) and declines towards fracture tip due to lesser friction and leak-off. Figure5.1 shows a schematic representation of pressure and stresses on fracture face. The fracture pressure at mouth continuously increases with time along with increase in plug length due to more suspended solids being accumulated with time. So, it is to be noted that if the rate of plug length increase is greater than rate of increase in pressure, then the fracture will not propagate and will eventually plug completely. In this model, this issue has been investigated and a model has been build which shows that the pressure drop over the entire fracture can lead to sufficient increase in fracture width and length, and thus fracture volume (ballooning effect). It also shows that the finite conductivity fracture can accommodate more solids over time without substantial increase in bottom-hole

injection pressure, and hence is able to propagate. A schematic representation of various stages of fracturing over time, under constant injection rate is shown in Figure5.2.

5.2. Fracture Propagation Criteria

In order to solve the main problem statement of this thesis, we need to combine the pressure profiles estimated in Chapter 3, induced stress changes calculated in Chapter 4 and the fracture propagation physical phenomena. In case of infinite conductivity fracture, Koning[1] solved the following fracture propagation equation to calculate fracture half-length X_f, for constant injection rate i_w, constant height of fracture h and at time t,

$$\Delta p_f(i_w, t, X_f, h) - \sigma_i - \sigma_{pT}(i_w, t, X_f, h) = G(X_f, h)\frac{K_{Ic}}{\sqrt{\pi X_f}} \tag{5.1}$$

where, Δp_f is difference between fracture and reservoir pressure before injection, σ_i is initial minimum horizontal stress before injection, σ_{pT} is combined effect of poro-elastic and thermo-elastic stress on fracture face, and $G(X_f, h)$ is a dimensionless fracture geometry factor that depends on whether fracture is short or long. In this model, $G(X_f, h) = 1$.

In fracture modelling during water injection, the fracture could grow, remain constant or shrink (partial closure) at a time step. This is determined using the stress intensity factor (K_I). It characterises the stress behaviour near fracture tip. The K_I at each fracture tip is evaluated at all time steps w.r.t the material property called rock toughness K_{Ic}, which is typically of the order of 10 $bar\sqrt{m}$. Using this concept, the following fracture propagation criterion has been used in this model to determine whether fracture propagates in a given time step or not.

$$K_I > K_{Ic}\ ;\text{Fracture tip extension or } X_f \text{ increases until } K_I = K_{Ic} \tag{5.2}$$

$$K_I < 0\ ;\text{Fracture tip shrinkage or } X_f \text{ decreases until } K_I = 0$$

$$0 \le K_I \le K_{Ic}\ ;\ \text{No extension or shrinkage of } X_f$$

This is called the Barenblatt propagation criterion for hard rocks. The stability range for it is shown in Figure5.3.

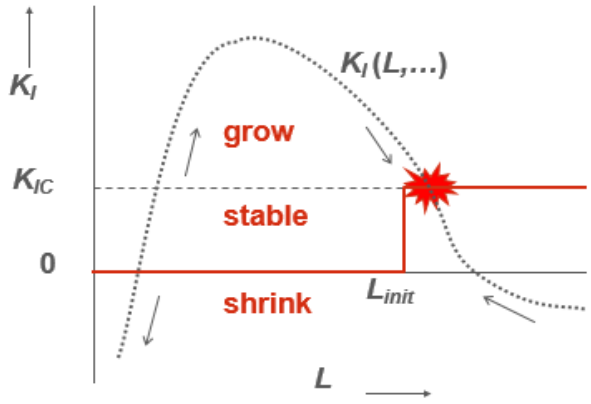

Fig 5.3: Barenblatt fracture propagation criterion (adapted from Shell)

Firstly, for a given time step, using the reservoir, fluid and rock properties, the pressure field around and in fracture is estimated at each grid cell. From this 2D pressure field, backstresses are estimated on fracture face. They are combined to estimate the fracture length at each time step using values from previous time step by Newton Raphson Iteration Method. In this model, the following fracture propagation equation for a recti-linear fracture has been implemented,

$$\frac{1}{\sqrt{\pi X_f}}\int_0^{X_f} dx\left[P_{frac}(q, t, X_f, h, x) - \sigma_i - \Delta\sigma_{pT}(q, t, X_f, h, x)\right]\sqrt{\frac{X_f + x}{X_f - x}} = K_{Ic} \tag{5.3}$$

The dimensionless stress intensity factor is given by,

$$K_{IcD} = \frac{2\pi kh}{\mu q}\frac{1}{\sqrt{\pi\, X_f}}\, K_{Ic} \tag{5.4}$$

This Equation (5.3) signifies the concept that in case of a finite conductivity fracture, the fluid pressure in the fracture P_{frac} *or* P_f, and the net backstress $\Delta\sigma_{pT}$ depend on the position along the fracture, x. Therefore, for implementation of this semi-analytical model, efficient algorithms for calculation of P_f and $\Delta\sigma_{pT}$ as function of time and fracture length is scripted and executed. By solving this Equation (5.3) in the model, we get the time dependence of fracture length and bottom-hole injection pressure. From Equation (5.2), the fracture propagation criterion could lead to different possible propagation scenarios such as,

- $K_I > K_{Ic}$: It signifies that the fluid pressure increases inside the fracture due to volume injected during (t_i-t_{i-1}) provides enough energy to overcome the rock toughness and fracture to propagate. So, a new fracture length X_f is computed that is in equilibrium with pressure field and stress conditions for time t_i using the Newton Raphson Method until $K_I - K_{Ic} \approx 0$.
- $K_I < 0$: It signifies that the volume injected does not provide sufficient energy to keep the fracture open. So, the facture begins to close and a new fracture length is computed that is in equilibrium with pressure field and stress conditions for time t_i until $K_I \approx 0$.
- $0 \leq K_I \leq K_{Ic}$: It signifies that the fracture is neither growing nor shrinking. So, X_f computed at time step t_{i-1} is equal to X_f at time step t_i. This is a stable scenario.

5.3. Fracture Tip Models

In this thesis, for finite fracture conductivity fracture, three fracture tip models have been discussed. For the concepts discussed above the following are the tip propagation models that can be implemented,

- The first model which is also the default model is based largely on the above-mentioned concepts. The fracture toughness K_{Ic} being a rock material property is input as a constant value. The fracture length is then iterated such that stress intensity factor K_I for each time-step converges with this K_{Ic} value to give the converged fracture length at that time. The tip stress $\Delta\sigma_{tip}$ evaluated in this case is proportional to $1/\sqrt{X_f}$. In terms of stress intensity factor, stress close to the fracture tip can be approximated as in Equation (5.5). This resulting tip stress reduces with increasing fracture length from Equation (5.5). This is often not observed in practice, where the tip-stress either gradually grows in time or remains high.

$$\sigma_{tip} = \frac{K_{Ic}}{\sqrt{\pi X_f}} \tag{5.5}$$

- In the second tip model, the minimum tip-stress $\Delta\sigma_{tip,initial}$ is specified along with an initial fracture toughness $K_{Ic,initial}$ value which tend to grow in time for large fractures. It is given by Equation (5.6). In this model, an effective fracture toughness $K_{Ic,eff}$ is estimated after every time step, which grows with fracture length. So, as the fracture propagates, new tip stress and fracture toughness are estimated. The criteria for propagation is that if the bottom hole pressure (BHP) exceeds the sum of minimum confining stress and effective tip stress evaluated from this tip stress model, then the fracture will propagate. It is to be noted that, since the confining stress changes with time, the fracture propagation may occur at an elevated stress state if poro-elastic stress increase dominates the confining stress, or at reduced stress state if thermal stress reduction due to formation cooling dominates the stress development.

$$\Delta\sigma_{tip} = \Delta\sigma_{tip,initial}\left(1 + \left(\frac{X_f}{3000}\right)^{0.25}\right) \tag{5.6}$$

$$\sigma_{tip} = \frac{K_{Ic,eff}}{\sqrt{\pi X_f}} \tag{5.7}$$

- In the third tip model, the initial fracture toughness $K_{Ic,initial}$ is specified as an input parameter as well. Unlike the second fracture tip model, in this case the tip stress remains constant with time. Only the effective fracture toughness $K_{Ic,eff}$ increases with fracture length after every time-step. So, as X_f grows with time, from Equation (5.5) the calculated $K_{Ic,eff}$ also grows with time by a factor of constant σ_{tip}. For this case as well, since the confining net stress changes with time, the fracture propagation may occur at an elevated stress state if poro-elastic stress increase after every time-step dominates the confining stress, or at reduced stress state if thermal stress reduction is dominant factor. The governing Equation for this model is given by,

$$\sigma_{tip} = \frac{K_{Ic,eff}}{\sqrt{\pi X_f}} = \text{constant} \tag{5.8}$$

The computational sequences for all three fracture propagation models have been mentioned in Appendix C.

5.4. Fracture Width Profile Model

In this section, the fracture width profile is discussed. The fracture width is assumed to have an elliptical profile which can be clearly observed in an infinite conductivity fracture. But, in this model the emphasis is on the width profile in case of a tip plug build up inside the fracture due to solids fill up. As discussed in Chapter 3, the injection of new solids with time reduces the fracture conductivity, which leads to a large pressure drop over the fracture. This causes the fracture to widen or expand and, increases its conductivity due to opening of existing wormholes in the plug. This is called the ballooning effect of the fracture that allows fracture to adjust its conductivity. In this model, the ballooning effect basically signifies large increment in fracture width due to the pressure drop over finite conductivity fracture. This is the objective as it increases the fracture volume significantly to accept more injected solids, propagate further and experience minimum loss in injectivity. The Figure5.4 below shows the expected width profile for a finite conductivity propagating fracture.

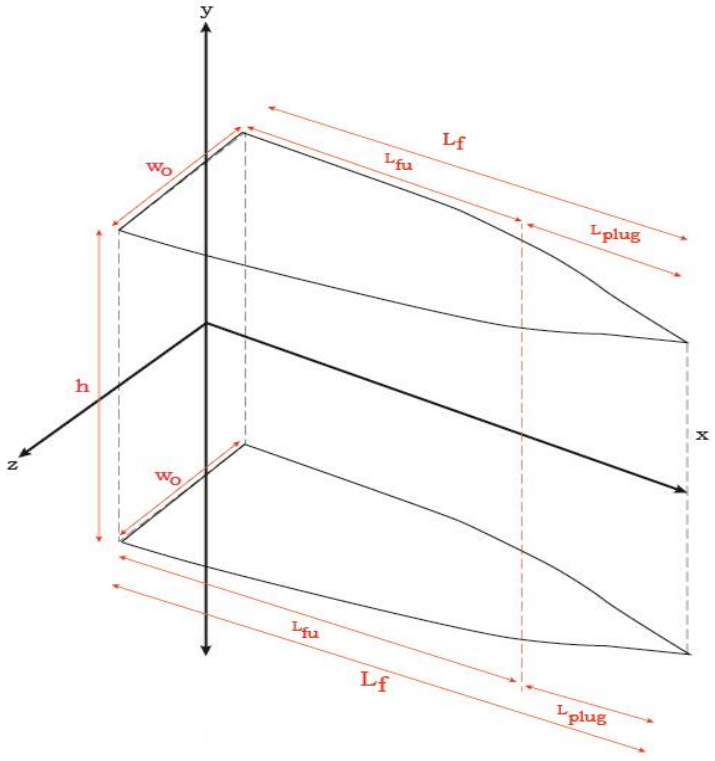

Fig 5.4: The Figure illustrates fracture width profile with a tip plug

The following Equations have been incorporated in the model under assumptions of a symmetric fracture,

$$w_f(x) = w\Delta p(x) - \ w_{S1}(x) - w_{S2}(x) \tag{5.9}$$

where, $w_{S1}(x)$ and $w_{S2}(x)$ are corrections which slightly decrease the width of fracture due to consideration of backstress effects on fracture face.

$$w\Delta p(x) = \left(\frac{4\,X_f}{E'E(m)}\right)\left(P_{frac} - \Delta\sigma_{pT}\right)\sqrt{1-\left(\frac{x}{X_f}\right)^2} \tag{5.10}$$

Where, $E' = \frac{E}{1-\nu^2}$, E = Young's modulus and $E(m) = \frac{\pi}{2}$

The correction terms are calculated using the net pressure in the following way,

$$w_{S1}(x) = \frac{2X_f S_1}{E'E(m)}\left\{\left(\left(1-\left(\frac{2}{\pi}\right)\arcsin(f_1)\right)\sqrt{1-\left(\frac{x}{X_f}\right)^2}\right) - \left(\left(\frac{2}{\pi}\right)\left(f_1-\left(\frac{x}{X_f}\right)\right)\operatorname{acosh}\left(\frac{1-f_1\frac{x}{X_f}}{\left|\left(\frac{x}{X_f}\right)-f_1\right|}\right)\right)\right\} \tag{5.11}$$

$$w_{S2}(x) = \frac{2X_f S_2}{E'E(m)}\left\{\left(\left(1-\left(\frac{2}{\pi}\right)\arcsin(f_2)\right)\sqrt{1-\left(\frac{x}{X_f}\right)^2}\right) - \left(\left(\frac{2}{\pi}\right)*\left(f_2+\left(\frac{x}{X_f}\right)\right)\operatorname{acosh}\left(\frac{1+f_2*\frac{x}{X_f}}{\left|\left(\frac{x}{X_f}\right)+f_2\right|}\right)\right)\right\} \tag{5.12}$$

Where, $S_1 = S_2 = \left(P_{frac} - \left(\sigma_i + \Delta\sigma_{pT}\right)\right)$ *and* $f_1 = f_2 = \frac{X_{fu}}{X_f}$ (since, symmetric case assumed)

For a fracture half-length X_f, w_{S2}(x) correction due to the other half of fracture is also included because pressure on the left half of fracture also affects the width on the right half-length (used in the model). Here, f_1 and f_2 are vertical upper and lower stress contrast which are basically equal to ratio of unplugged fracture half-length to total fracture half-length.

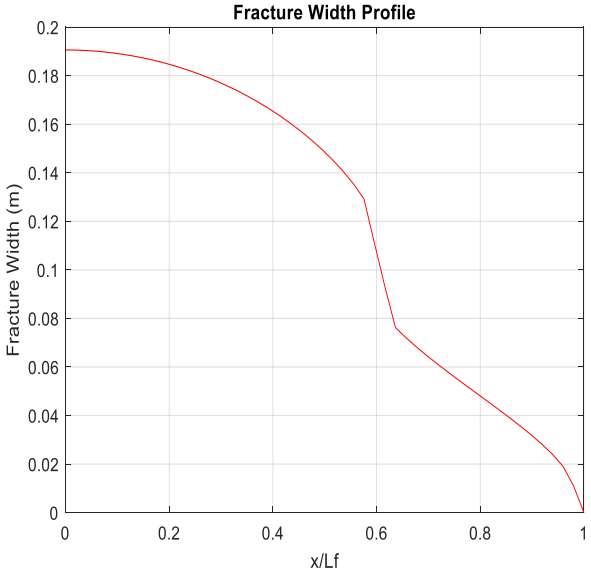

Fig 5.5: Fracture width profile from model for a static frac

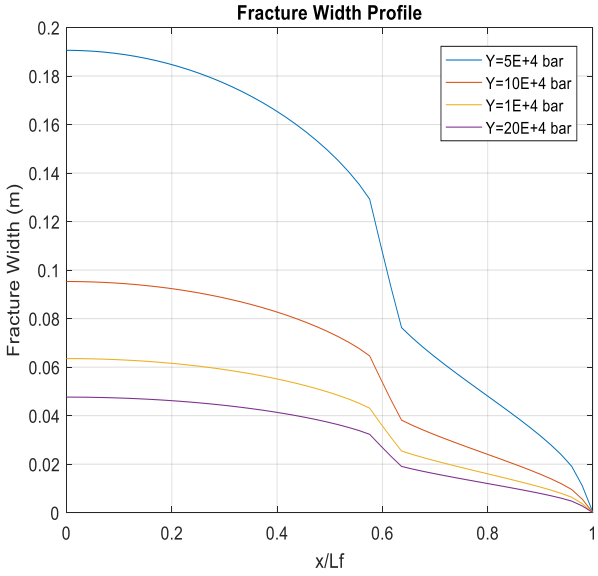

Fig 5.6: Frac width profile with different Young's modulus

The above graphs are obtained from the model after implementing the above-mentioned equations. Figure5.5 shows the width profile in a static fracture with tip plug after 100 days. It is clearly seen that the plug starts at $x = 60\,m$ in a 100m fracture for example. Figure5.6 on the other hand, illustrates the dependency of fracture width on Plain Strain Young's modulus of adjacent formations. This means that, the higher the Young's modulus, the more is the stiffness of the rock and thus, it causes lesser width expansion of the fracture.

6

Results & Discussions

In this Chapter, the results obtained from the infinite and finite conductivity fracture pressure model, stress model and fracture propagation model have been discussed. For completeness and clarity, relevant results from Koning's model, WF model based on Koning's work and SLOFRAC software (adapted from Shell) have also been discussed briefly in the respective sections.

6.1. Infinite Conductivity Fracture

6.1.1. Pressure solution around fracture

In this section, the pressure profile for three zones around the fracture and in the fracture, are illustrated. Also, comparison of poro-elastic stresses at the fracture wall with Koning's results (Table 3-I[1]) for numerical and analytical model have been discussed.

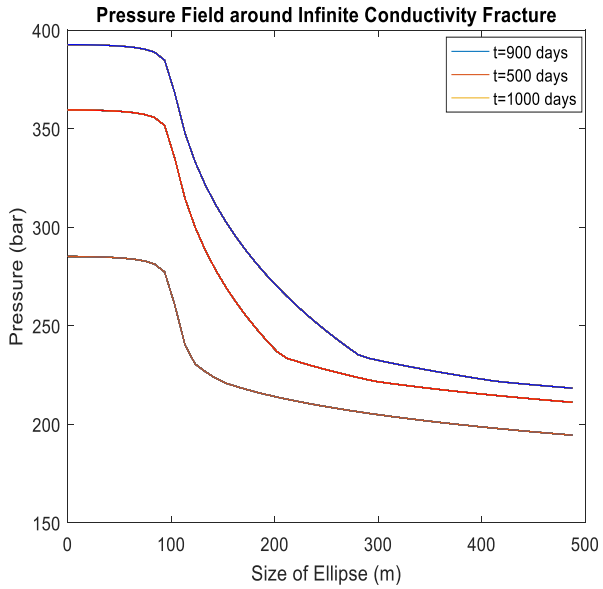

Fig 6.1: P(ξ) vs. ξ for 3 zones around static fracture

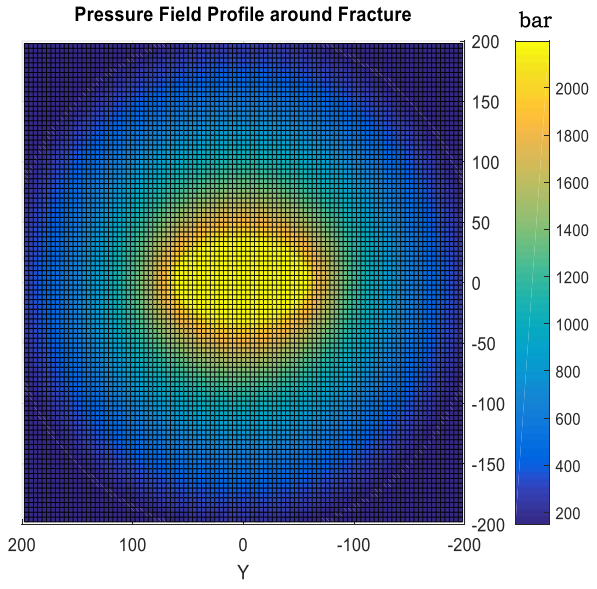

Fig 6.2: P(ξ) field for 3 zones around static fracture in 2D

In Figure6.1, the pressure profile around an infinite conductivity fracture is shown. It clearly illustrates behaviour of Darcy pressure wave upon cold water injection. The initial pressure drop is in the cold zone where we have maximum viscosity value. When this cold water comes in contact with the formation rock, it immediately gets warm and a sharp change in the pressure wave at the boundary between zone 1 and zone 2 is observed. This ΔP(ξ) satisfies the Laplace Equation (3.9) and, boundary conditions (3.10) and (3.11). When the pressure transient reaches the oil zone boundary, another sharp change is observed and the pressure keeps declining until ΔP(ξ) is equal to zero or P(ξ) equals reservoir pressure P_{res}. In Figures 6.2 and 6.3, the similar concept is shown in different view for better understanding. The fracture length taken to produce these results is 50m and constant fracture height is 50m. The simulation parameters are discussed in detail in Appendix D. In Figure6.4, 6.5 and 6.6, the pressure wave increase over time has been shown for a static fracture of length 50m and reservoir permeability of 100mD.

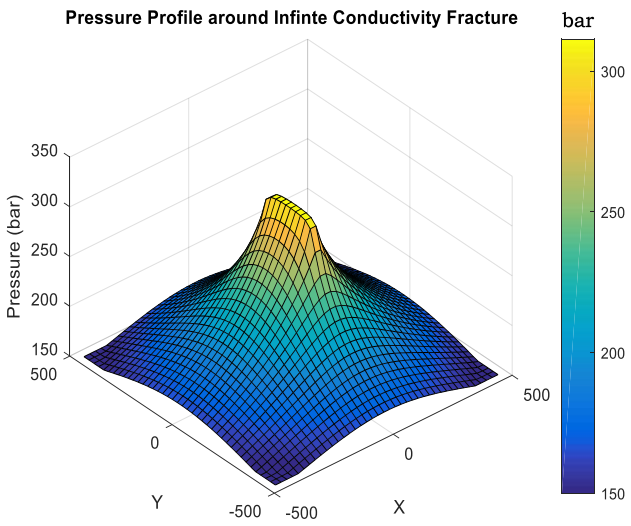

Fig 6.3: P(ξ) field for 3 zones around frac in 2D (top view)

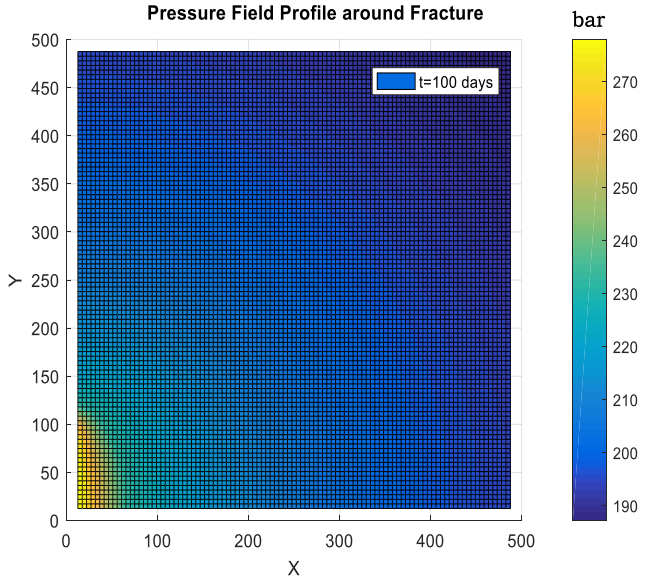

Fig 6.4: P(ξ) field (bar) for 3 zones 2D view after 100 days

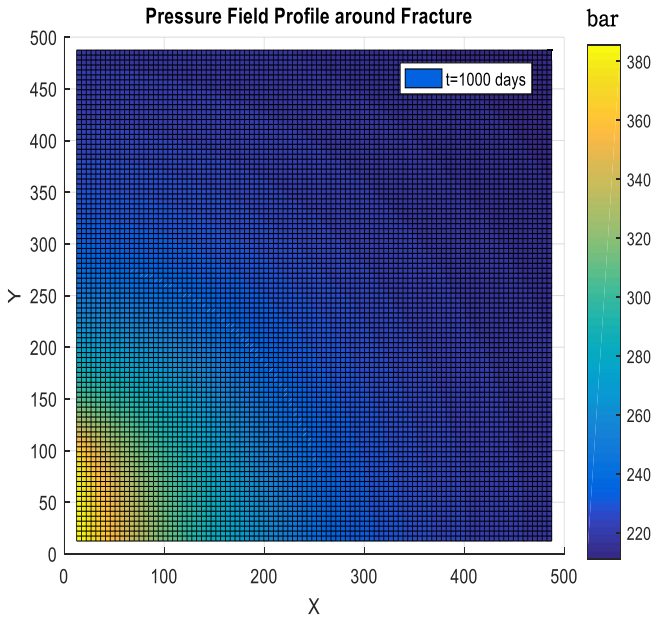

Fig 6.5: P(ξ) field (bar) for 3 zones 2D view after 1000days

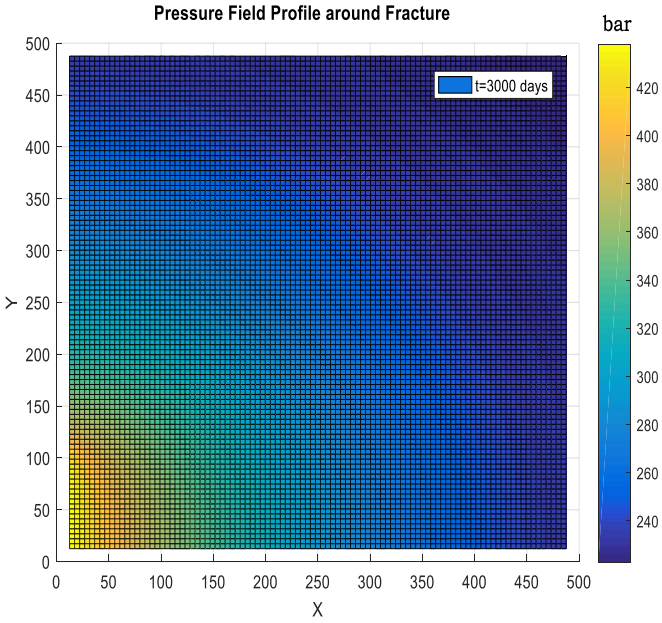

Fig 6.6: P(ξ) field (bar) for 3 zones 2D view after 3000days

6.1.2. Pressure solution in the fracture

As discussed in Chapter 3, the fracture pressure profile for an infinite conductivity fracture will give a constant pressure solution. There is no damage due to clean water injection and permeability is infinity throughout the fracture length. The main focus of this thesis is on fracture pressure with damage inclusion, and so this section has not been discussed in detail. However, results for infinite conductivity fracture have been included in Chapter 6 for completeness.

6.1.3. Poro-elastic backstress solution in fracture (analytically and numerically)

In this section, numerical and analytical calculations of poro-elastic stress changes at fracture face have been discussed. For completeness, firstly the results given by Koning (Table 3-I[1]) have been recreated in this model, for a range of dimensionless heights $h_D = \frac{h}{2R_e}$ from 0.01 to 1.0 and, for a range of $\frac{X_f}{h}$ ratios from 0.01 to 10.0. The results of comparative analysis of both sets of results have been presented in tabular form in Table 6.1 and 6.2 below. The table shows that the analytical results when $\frac{X_f}{h} \leq 1.0$ for $\Delta\sigma_{ypD}$ are within 1% accuracy of the numerical results whereas for $\Delta\sigma_{xpD}$ they are within 5% accuracy approximately. The

accuracy reduces for the other two cases in the table mainly because the method derived in Koning's thesis for evaluation of stress was developed to be valid for small $\frac{X_f}{h}$ ratios. However, the accuracy is still within 10%, which is acceptable. So, for practical purposes, for $\frac{X_f}{h} \leq 1.0$ the method used in the model is sufficiently accurate.

For stress along the fracture wall $\Delta\sigma_{xpD}$ from Table 6.1 we get,

$h/(2R_e)$	X_f/h	Num. Koning	Num. model	Num. 3 zones	Anal. Koning	Anal. model	Anal. 3 zones
0.01	0.01	6.82	6.70	6.85	6.82	6.81	6.75
	0.1	5.66	5.69	5.30	5.66	5.65	5.60
	1.0	4.32	4.30	4.20	4.42	4.41	4.40
	10	2.28	2.29	2.44	2.51	2.51	2.51
0.1	0.01	4.56	4.59	4.43	4.56	4.56	4.45
	0.1	3.40	3.41	3.21	3.41	3.41	3.29
	1.0	2.06	2.06	2.47	2.16	2.16	2.10
1.0	0.01	2.65	2.60	2.80	2.65	2.64	2.55
	0.1	1.49	1.48	1.44	1.49	1.49	1.40

For stress perpendicular to the fracture wall $\Delta\sigma_{ypD}$ from Table 6.2 we get,

$h/(2R_e)$	X_f/h	Num. Koning	Num. model	Num. 3 zones	Anal. Koning	Anal. model	Anal. 3 zones
0.01	0.01	6.32	6.31	6.10	6.32	6.316	6.25
	0.1	5.16	5.20	4.80	5.16	5.16	5.10
	1.0	3.93	3.96	3.86	3.92	3.92	3.91
	10	2.17	2.12	2.03	2.01	2.005	2.00
0.1	0.01	4.06	4.08	3.50	4.06	4.058	3.95
	0.1	2.90	2.95	2.78	2.91	2.90	2.82
	1.0	1.67	2.70	2.10	1.66	1.66	1.61
1.0	0.01	2.15	2.20	2.14	2.15	2.14	2.05
	0.1	0.996	1.10	0.85	0.994	0.98	0.92

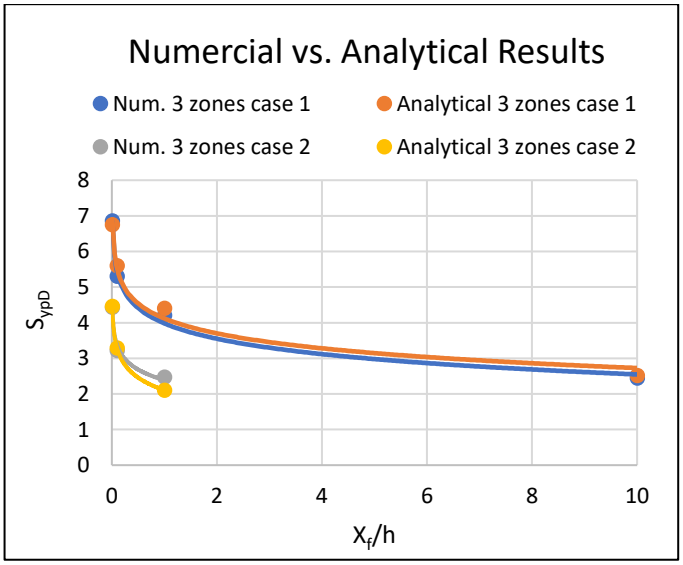

Fig 6.7: Numerical vs Analytical results for this model

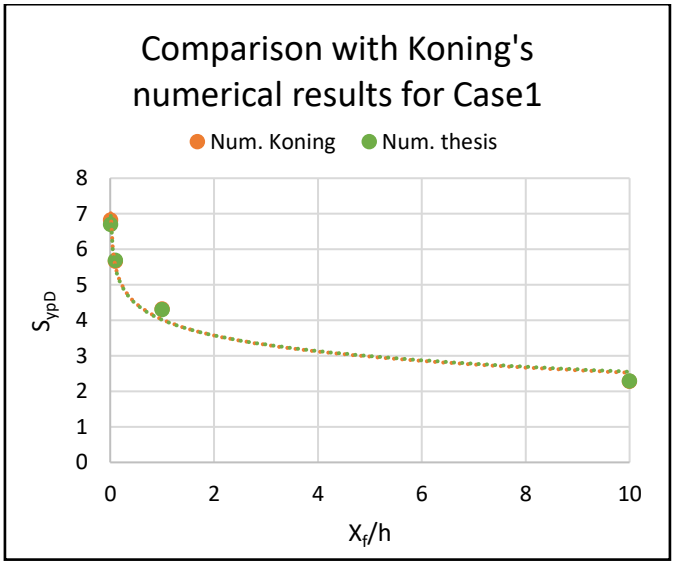

Fig 6.8: Comparison with Koning's Num. results for case 1

The permeability and viscosity input values for the above model cases are tabulated below for reservoir height h equal to 120m as an example. It shows the input parameters for mobility $\left(\lambda = \frac{k.k_r}{\mu}\right)$ in each of the three cases for different $\frac{X_f}{h}$ ratios from Table 6.3 are,

X_f [m]	X_f/h	K_1 (m^2)	K_2 (m^2)	K_3 (m^2)	μ_1 (Pa.s)	μ_2 (Pa.s)	μ_3 (Pa.s)
1.2	0.01	5E-13	4E-13	1E-13	1E-3	6E-4	8E-4
12	0.1	5E-13	4E-13	1E-13	1E-3	6E-4	8E-4
120	1.0	5E-13	4E-13	1E-13	1E-3	6E-4	8E-4
1200	10	5E-13	4E-13	1E-13	1E-3	6E-4	8E-4
1.2	0.01	5E-14	4E-14	1E-14	1E-3	6E-4	8E-4
12	0.1	5E-14	4E-14	1E-14	1E-3	6E-4	8E-4
120	1.0	5E-14	4E-14	1E-14	1E-3	6E-4	8E-4
1.2	0.01	5E-15	4E-15	1E-15	1E-3	6E-4	8E-4
12	0.1	5E-14	4E-14	1E-14	1E-3	6E-4	8E-4

As mentioned in section 6.1.2, the poro-elastic backstress due to pore pressure inflation on fracture wall for an infinite conductivity fracture gives a uniform solution as shown in Figures 6.9 and 6.10. It shows the stress calculated numerically on fracture face by superposition principle from pressure field around the fracture in a 40 x 40 and 100 x 100 grid mesh respectively. The input parameters in both case are different.

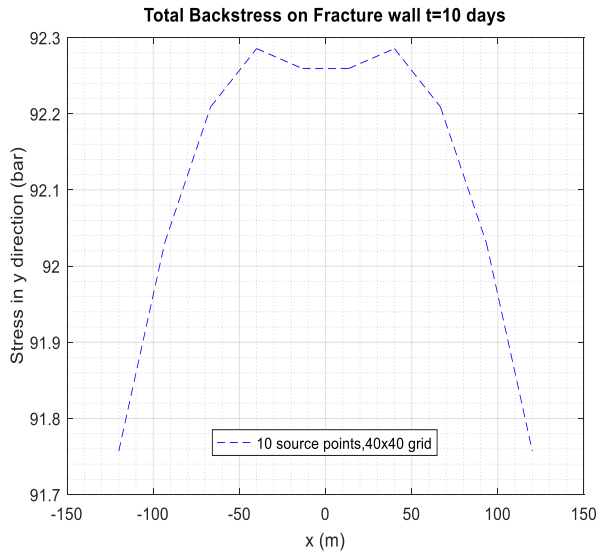

Fig 6.9: Numerical constant backstress $\Delta\sigma_{yp}$~92 bars

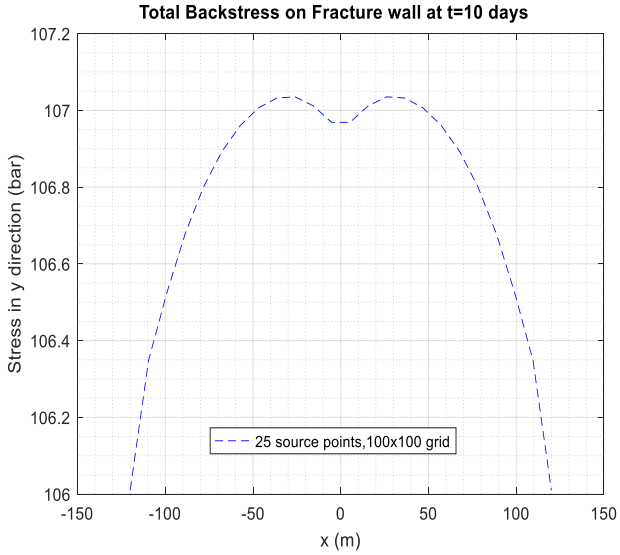

Fig 6.10: Numerical constant backstress $\Delta\sigma_{yp}$~106 bars

6.2. Finite Conductivity Fracture

In this section, the pressure profile for three zones around the finite conductivity fracture and in the fracture are illustrated. Also, poro-elastic and thermo-elastic stresses at fracture wall both numerically and analytically have been discussed.

6.2.1. Pressure solution around fracture

As discussed in Chapter 3, the non-zero pressure drop over fracture implies that there is no elliptical symmetry of pressure solution around the fracture. A fracture step function is taken as an arbitrary fracture permeability profile, using which the problem is solved semi-analytically. In order to solve the full Laplace Equation, truncated Fourier series is used. The detailed calculation of Fourier coefficients is given in Appendix A.

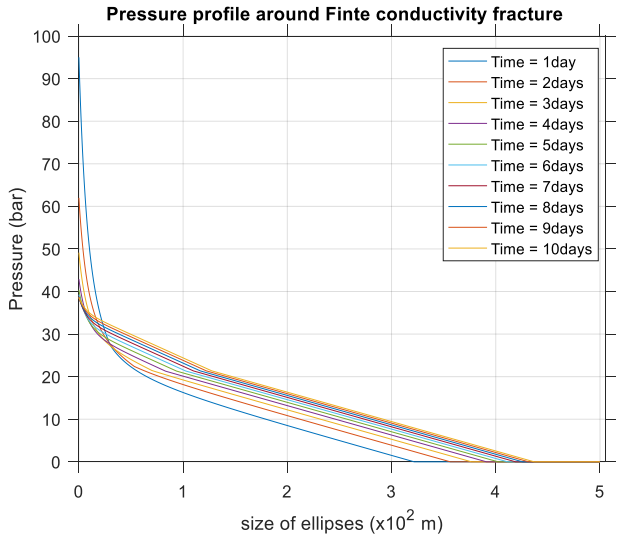

(a)

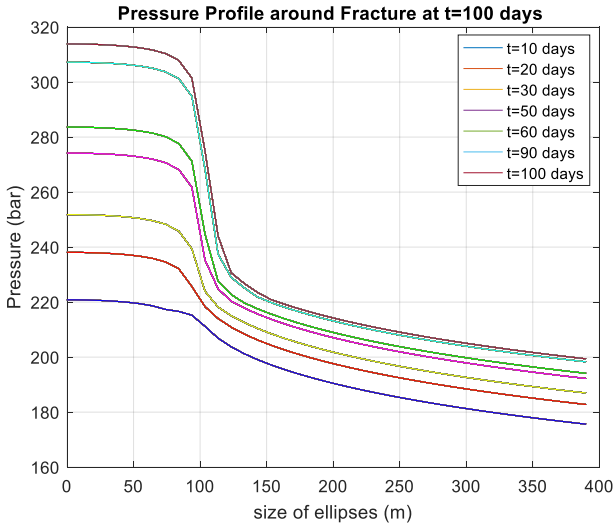

(b)

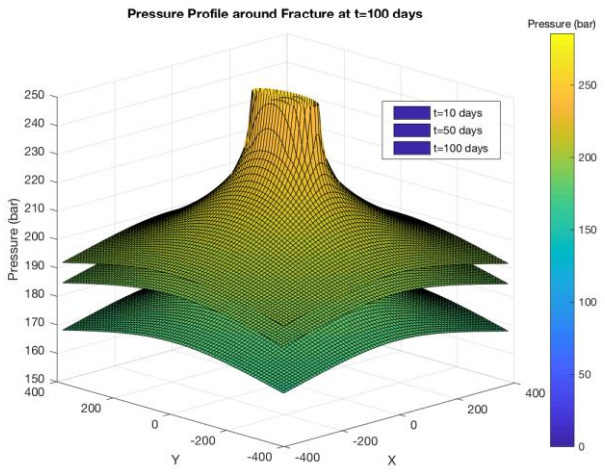

(c)

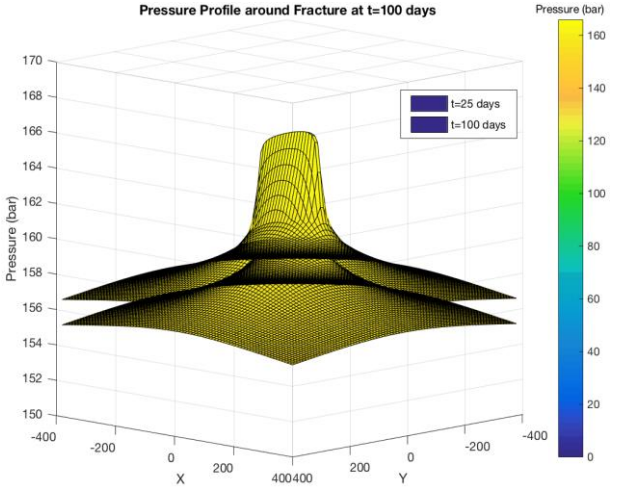

(d)

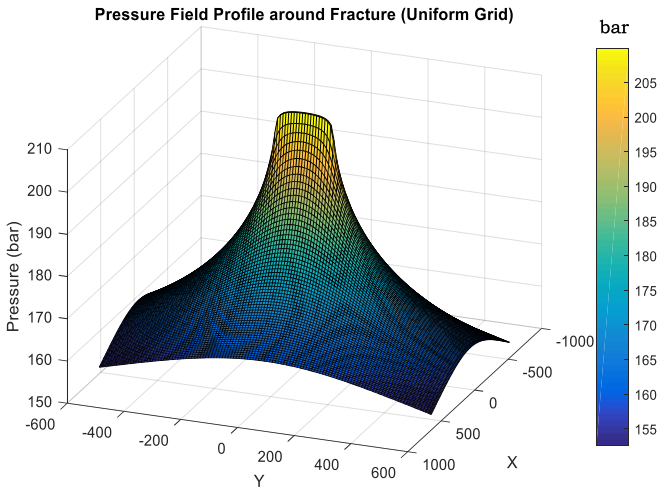

(e)

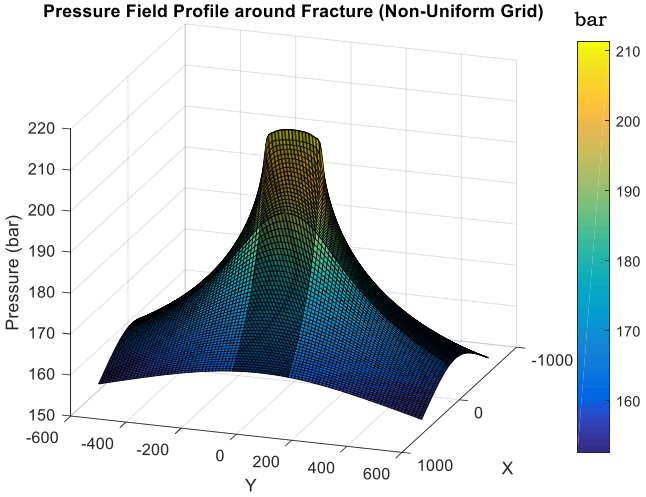

(f)

Fig 6.11: Pressure profile around the finite conductivity fracture P(ξ) with (a) Two zones and η_{12}=0.05, (b) Three zones and η_{12}=0.05, (c) Three zones in 3D view with k=100 mD (η_{12}=0.9), (d) Three zones in 3D view with k=1D (η_{12}=0.9), Three zones in 3D view with k=100mD and (e) Uniform grid distribution whereas, (f) Non-uniform grid distribution.

In the above Figures, the pressure has been plotted against size of the ellipses from zone 1 to zone 3 for different x_{12} *or* η_{12} positions. We see pressure rising with time due to continued injection at constant rate. This pressure declines away from the fracture until it reaches the reservoir pressure (150 bars) beyond zone 3 boundary. Also, in Figure6.11(c), $k_{f2}\,(1D) > k(100mD)$ whereas in Figure6.11(d), $k(1D) > k_{f2}(100mD)$ which clearly shows the effect of formation permeability and plug permeability on energy of the system. Also, it is to be noted that $\tan(\eta_{12}) = \left(\frac{cosh\xi}{sinh\xi}\right)\frac{y}{x}$. Figures6.11(e) and (f) show that non-uniformity of grid distribution with smaller grids near the fracture doesn't show any effect on near fracture pressure profile.

6.2.2. Pressure solution in the fracture

As discussed in Chapter 3, $\Delta p_f(\eta)$ *or* $\Delta p_f(x)$ is the fluid pressure profile within the fracture or the fracture pressure. It is calculated at $\xi = 0$ by contributions from pressure in fracture and formation adjacent to the fracture. Again, a permeability step function $k_f(\eta)$ is taken as an arbitrary fracture permeability profile. The fracture pressure is calculated both analytically and numerically. It should be noted that although $\Delta p_f(x)$ is expected to be uniform over unplugged part, it is now a function of x coordinate or η in the plugged part. Also, the comparison plot of $\Delta p_f(x)$ with and without external filter-cake of thickness $b(x)$ is presented below. The detailed calculation of Fourier sum coefficients is given in Appendix A.

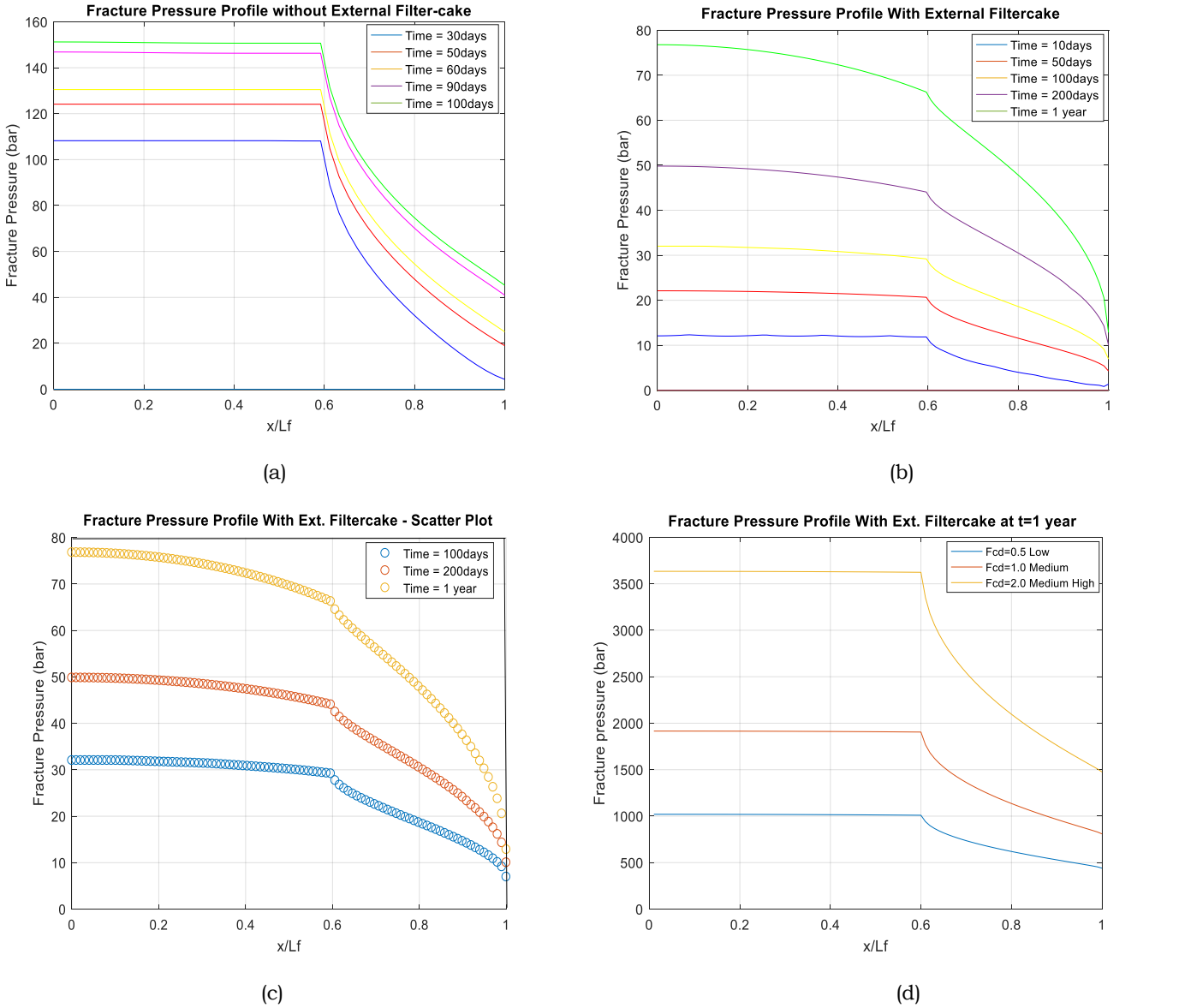

Fig 6.12: Fracture pressure profile $\Delta p_f(\eta)$ with tip plug, constant fracture width and (a) Without external filter-cake, (b) With external filter-cake, (c) With external filter-cake in a scatter plot showing 100 grid points on the fracture, and (d) With external filter-cake for different dimensionless fracture conductivity values after t=1 year. The filter-cake permeability used is $k_e = 1\mu d$.

As discussed in Chapter 3, the formation of an impermeable tip plug behind the fracture tip is more realistic than a uniform fracture permeability scenario, especially over prolonged period of injection of contaminated water. This observation is proven with more evidence in section 6.4 using figures explaining the effects of presence of tip plug on wellhead pressure and well injectivity.

In the above plots, fracture pressure profile has been plotted along the fracture half-length assuming constant fracture width w_0 (for simplicity) for various cases. In Figure6.12(a) the fracture pressure $\Delta p_f(\eta)$ is plotted against x/X_f, and it is seen that p_f remains constant in the unplugged part due to uniform permeability k_{f1}, but drops as soon as x exceeds unplugged length X_{fu}. In the plugged section, frac permeability k_{f2} is also taken to be uniform but it's much lower (close to formation permeability) due to very small sized solids deposition at tip. This is primarily the reason for this pressure trend. In Figure6.12(b) however, there is presence of an elliptical external filter-cake on fracture face due to which a continuous decrease in p_f is observed even behind the plug. The pressure in unplugged length isn't constant anymore due to presence of an external filter-cake caused by solids deposition on fracture wall. Figure6.12(c) demonstrates the number of fracture grid points or source points used to estimate the pressure profile. In this case 100 grid points are used. Figure6.12(d) is an interesting Figure as it is plotted for different dimensionless fracture conductivities ($F_{cd} = (k_{f2} * w_0)/(k_1 * X_f)$) after 1 year of injection. It is to be noted that external filter-cake is still present in this case, but clearly doesn't affect the fracture pressure much. This is because to obtain F_{cd} value of 2.0 and less, significantly lower formation permeability is used. This shows that formation permeability also has significant effect on pressure in fracture caused due to $1\mu D$ external filter-cake. So, it's observed that a lower permeability adjacent formation reduces pressure drop over external cake.

6.2.3. Poro-elastic backstress calculation on fracture face

As discussed in Chapter 4, for poro-elastic stress changes along the fracture length, an inclusion with a constant pressure can't be assumed, unlike thermo-elastic stress changes. The pressure disturbance extends to a large distance away from facture and falls off slowly to zero. Koning[1] suggested that for such a pressure disturbance, the stress change due to pore pressure inflation will be in the case of a plane strain[1]. The poro-elastic backstress on fracture face for an infinite conductivity fracture has already been discussed in section 6.1. In this section, results for poro-elastic backstress on a finite conductivity fracture face is discussed in detail. Also, comparison between total stress and computed fracture pressure with and without an external filter-cake is discussed.

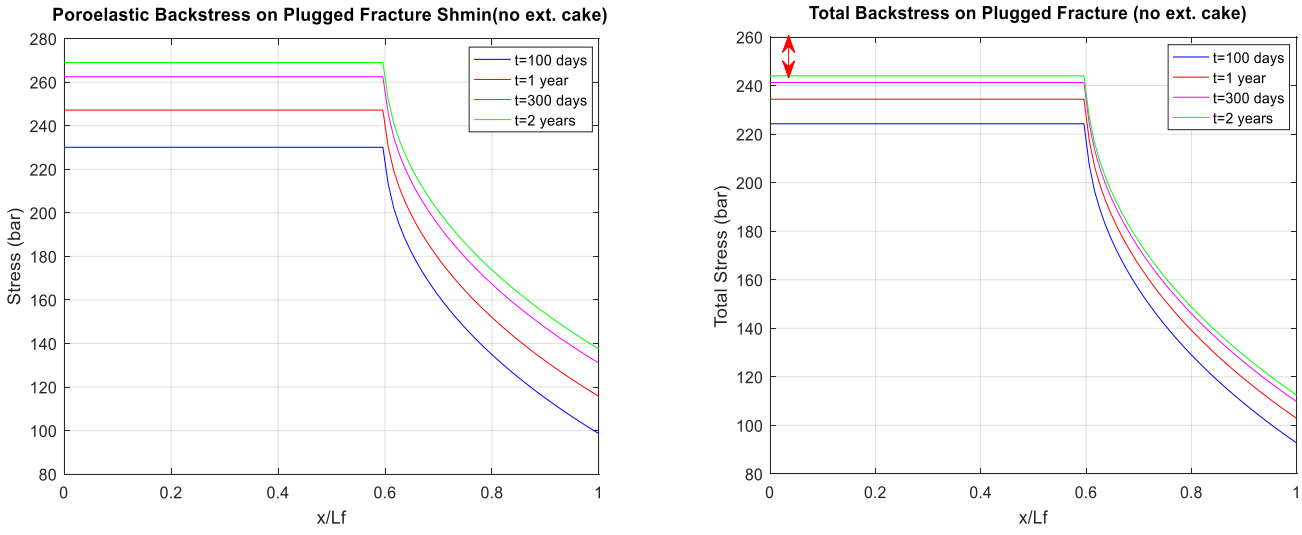

(a) (b)

Fig 6.13: (a) Poro-elastic backstress and, (b) Total stress on fracture with tip plug after two years of constant injection

In the above Figure6.13, the poro-elastic backstress on fracture face has been calculated using analytical expressions derived by Koning[1] in the unplugged part ($\frac{x}{X_f} \leq 0.6$) whereas in plugged part ($\frac{x}{X_f} > 0.6$), the stress is dependent on x-coordinate as given in Appendix B of paper by Hoek *et al.*[2]. The analytically approximated expression used here is achieved by using an infinite conductivity fracture with length equal to the

unplugged half-length X_{fu} instead of X_f. In Figure6.13(b), a similar plot to 6.13(a) is plotted but now total stress has been calculated (poro-elastic + thermo-elastic stresses). It is observed that the thermal effect of cold water injection has a reducing effect on net stress due to rock contraction. Also, if an external filter-cake is present then, filter-cake thickness isn't zero at $x = X_{fu}$ (i.e. "tip" of infinite conductivity fracture[2]). Therefore, an approximate expression is also derived in work of Hoek *et al.*[2] to account for the larger pressure drop over external filter-cake.

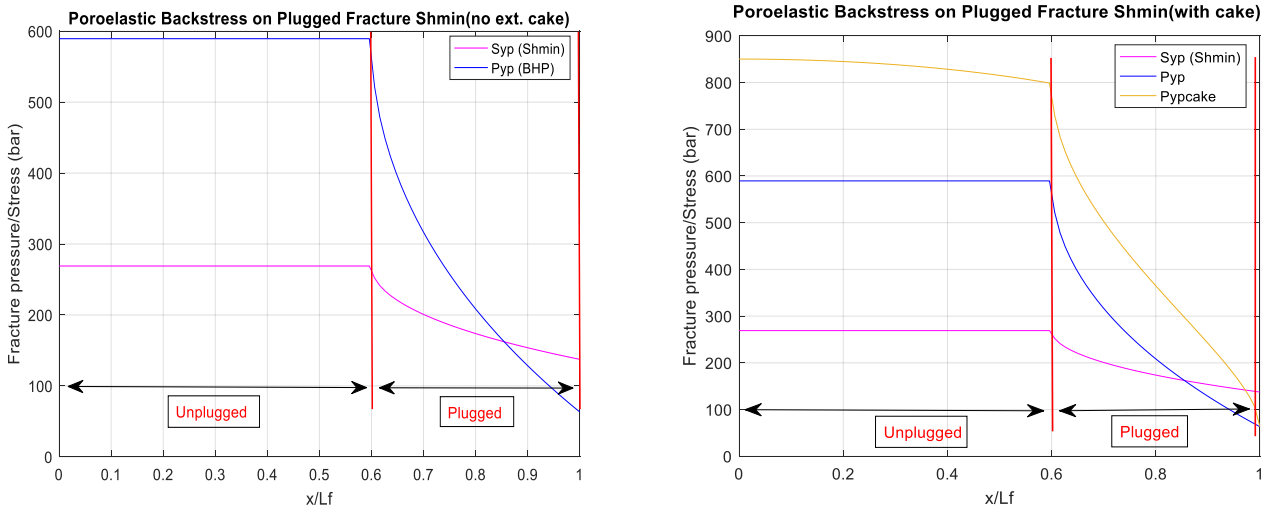

(a) (b)

Fig 6.14: Poro-elastic backstress and computed fracture pressure (a) Without external filter-cake and, (b) With external filter-cake are plotted, as a function of the coordinate x.

Figure6.14 shows an example of fracture pressure and poro-elastic backstress profiles computed analytically. In Figure6.14(a), we observe that the net pressure ($P_{net} = P_f - S_{hmin}$) becomes negative in the plugged region. This is because of lesser decrease in stress than P_f in plugged part. A negative net pressure obstructs the progression of fracture under dynamic conditions. It is observed in this example mainly because of two reasons, (i)Low formation permeability~10mD, and (ii)Very high $\frac{X_f}{h}$ ratio. Both, low permeability and $\frac{h}{X_f} < 1$ cause larger pressure drop compared to stress and thus, negative net pressure is observed. Similarly, in Figure6.14(b), we observe the same phenomenon in presence of an external filter-cake. The additional pressure drop over filter-cake can also be observed along with the elliptical filter-cake profile (yellow curve) clearly.

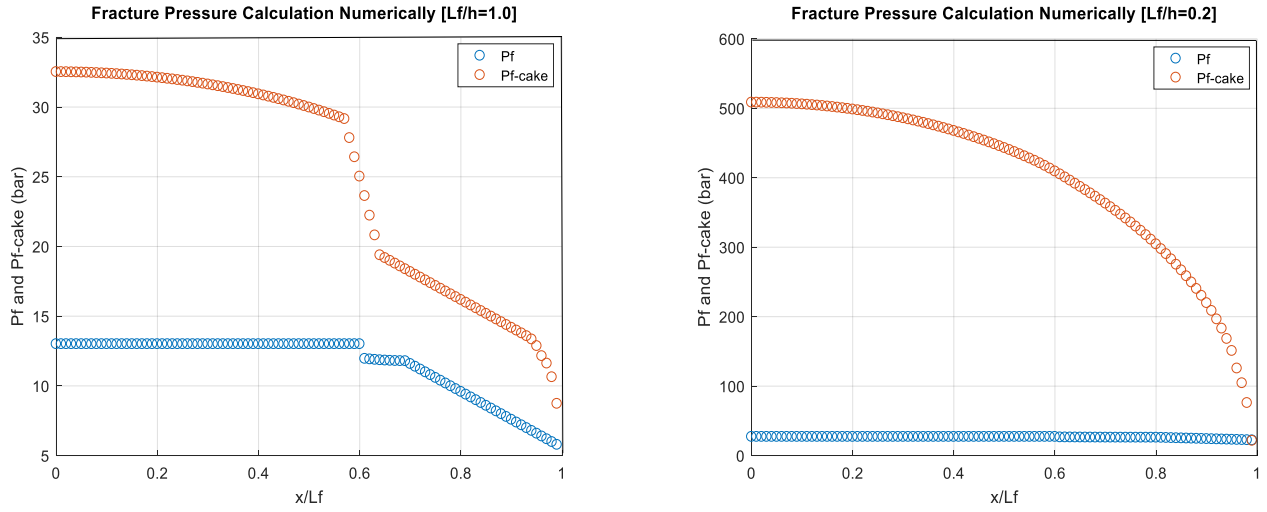

(a) (b)

Fig 6.15: Fracture pressure with and without filter-cake calculated numerically with 100 source points on fracture for (a) $\frac{Xf}{h} = 1.0$ and, (b) $\frac{Xf}{h} < 1.0$.

In the Figure6.15, we observe the effect of X_f/h ratio on the estimated fracture pressure in numerical model. Figure6.15 (b) is particularly noticeable w.r.t the fact that fracture pressure drops only few bars whereas, it drops a few hundred bars in presence of an external filter-cake. This is because of the very small length of fracture, which is not enough to form a significant internal plug. Therefore, despite of a larger pressure drop, a sharp drop in not observed in P_{fcake} case (orange curve), unlike in Figure6.15 (a).

As discussed in Chapter 4, the changes in reservoir pressure and temperature due to cold water injection lead to change in state of stress in the adjacent formation. Increase in pore pressure causes poro-elastic increase in backstress and formation cooling causes thermo-elastic decrease in backstress. The overall effect is given by Equation (4.17). This has been calculated numerically as well using Equation (4.9) to present an extensive analysis of the stress changes as well as validate analytical calculations. Koning[1] presented this calculation in Appendix 3-B of his thesis, in which he calculated changes in stress due to steady state changes in pressure and temperature, based on application of Hooke's law for linear and isotopic medium[7]. The results for numerical poro-elastic stress calculations are given below in Figure6.16.

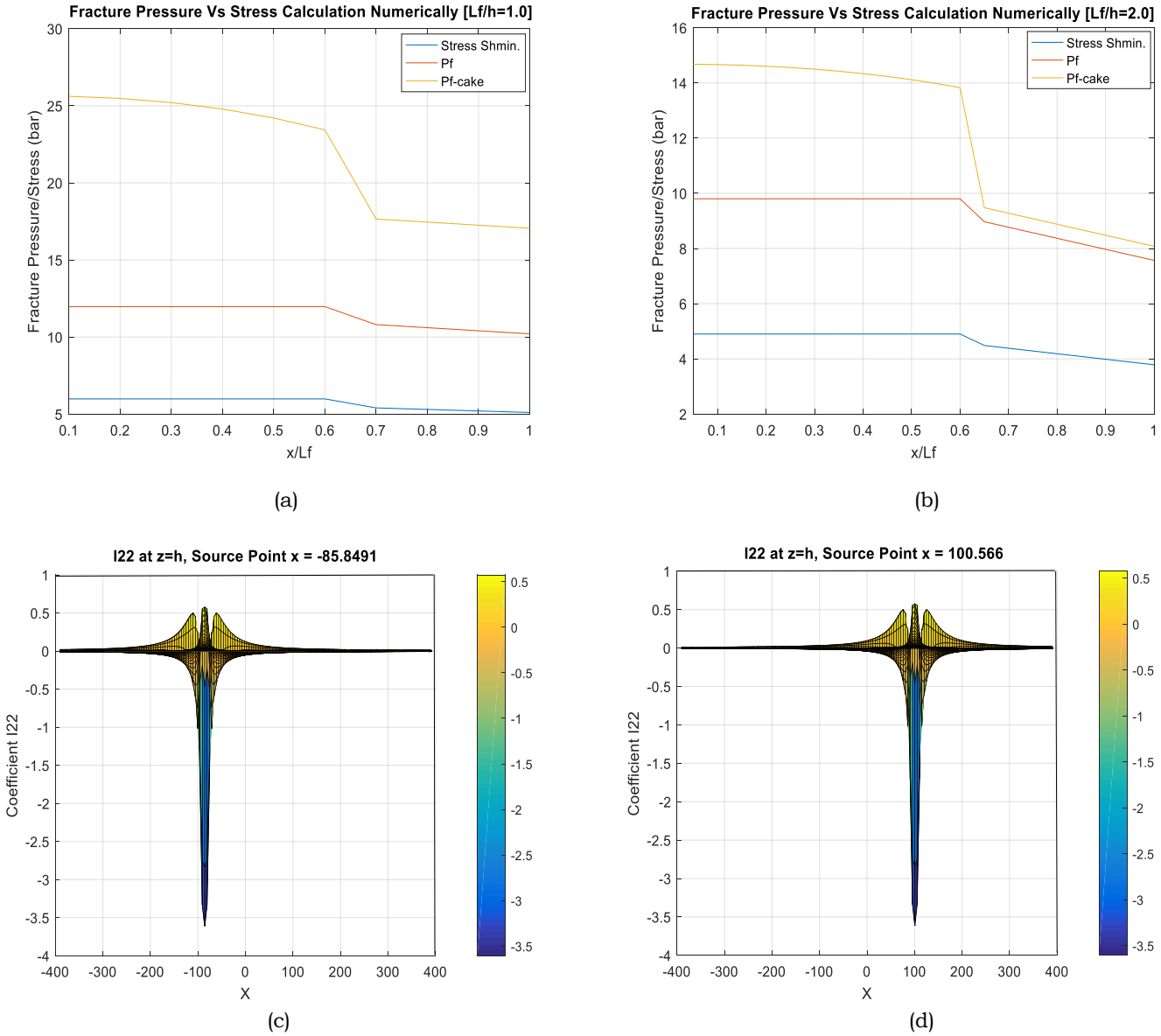

Fig 6.16: The plots show results of poro-elastic stress calculation Syp numerically. In (a) a comparative plot of fracture pressure P_f vs. $P_{f\text{-cake}}$ vs. Stress for $\frac{X_f}{h} = 1.0$ case after $t = 7$ days of injection, whereas in (b) a comparative plot of fracture pressure P_f vs. $P_{f\text{-cake}}$ vs. Stress for $\frac{X_f}{h} = 2.0$ case after $t = 10$ days of injection. In Figures (c) and (d), the values of coefficient I_{22} obtained after volume integral calculation of stress are shown w.r.t position of the source point on the fracture as shown in titles of both figures.

It is clearly shown that the trend of results from the numerical model match the behaviour of results obtained from analytical model. As mentioned in Chapter 4 and later formulated in Appendix B, the volume integral for stress calculation is solved analytically[16] and the results obtained require calculation of two coefficients I_{11} *and* I_{22} for S_{xp} *and* S_{yp} estimation respectively. Also, as the pressure profile is constant over the height of the rectangular fracture, the integral over z-direction is neglected and the length a_3 of parallelepiped is replaced by $z = a_3 = h\ (or\ \frac{h}{2})$ where h is the reservoir height. This is also indicated in title of Figures 6.16 (c) and (d).

6.2.4. Error Analysis between Analytical and Numerical Results

In this section, the error analysis of analytical and numerical results for fracture pressure in case of a low permeability tip plug has been presented for various $\frac{X_f}{h}$ ratios.

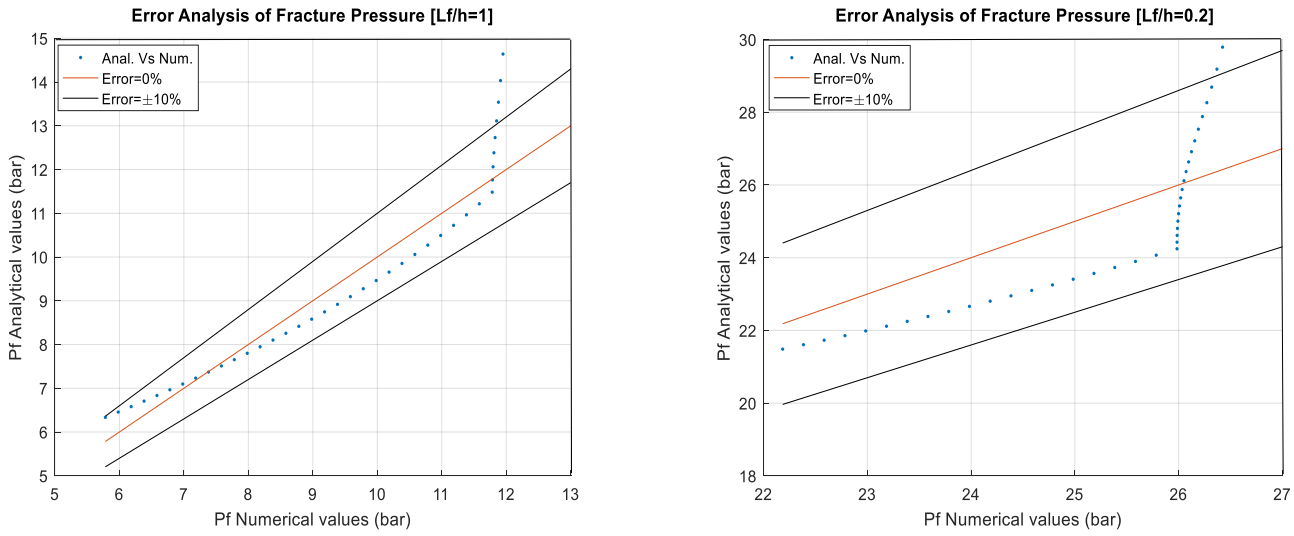

(a) (b)

Fig 6.17: Error analysis of numerical and analytical results of finite fracture pressure for (a) $\frac{X_f}{h} = 1.0$ and, (b) $\frac{X_f}{h} < 1.0$.

The permeability inputs for this case are $k_{f1} = 1e^{-2}m^2, k_{f2} = 1e^{-12}\ m^2\ and\ k = 1e^{-12}\ m^2$. It is shown that the numerical results are mostly within 5-7% of the analytical results for $\frac{X_f}{h} \leq 1$. For cases of $\frac{X_f}{h} > 1$, especially when X_f is 10 times larger than h, the error is >10%. The reason for this is because the analytical expressions modelled represents an approximation to low-permeability tip plugs given in Appendix B[2]. This is done by treating unplugged length as infinite conductivity fracture and using corresponding expressions[1] for it whereas, for numerical case, the fracture pressure on entire fracture face (unplugged + plugged lengths) is calculated using the pore pressure field in the adjacent formations.

6.2.5. Thermo-elastic backstress on fracture face

In this section, result of thermo-elastic stress change on the fracture face described in section 4.3 has been briefly discussed. The results in previous sections of this Chapter already include effect of thermo-elastic changes. Thermo-elastic stresses can be calculated from the theory of inclusions in an elastic solid which comes from the Lauwerier solution. It shows that after a relatively short period of time temperature change (ΔT) can be approximated using a step function. Since, cold water is being injected, inside the cold front zone a uniform injection temperature T_{inj} is taken, and outside it the reservoir is assumed to still be at initial temperature equal to reservoir temperature (T_{res}) such that, $\Delta T = T_{inj} - T_{res}$. The Figure6.18(a) below, shows result based on this concept and calculated from expressions derived by Perkins *et al.*[8] which are also described in Appendix 3-C by Koning[1]. Figure6.18(b) shows the computed dimensionless stress in y direction i.e. along the minor axis, for elliptical inclusions of various shapes. If the elliptical inclusion or penetration is tall w.r.t the minor axis of ellipse, there will be a stress difference for elongated ellipses. On other hand, for inclusions that are short w.r.t the minor axis, stress change will be isotropic. It is to be noted that, this situation is different in case of poro-elastic backstress where we haven't assumed an inclusion with a constant pressure.

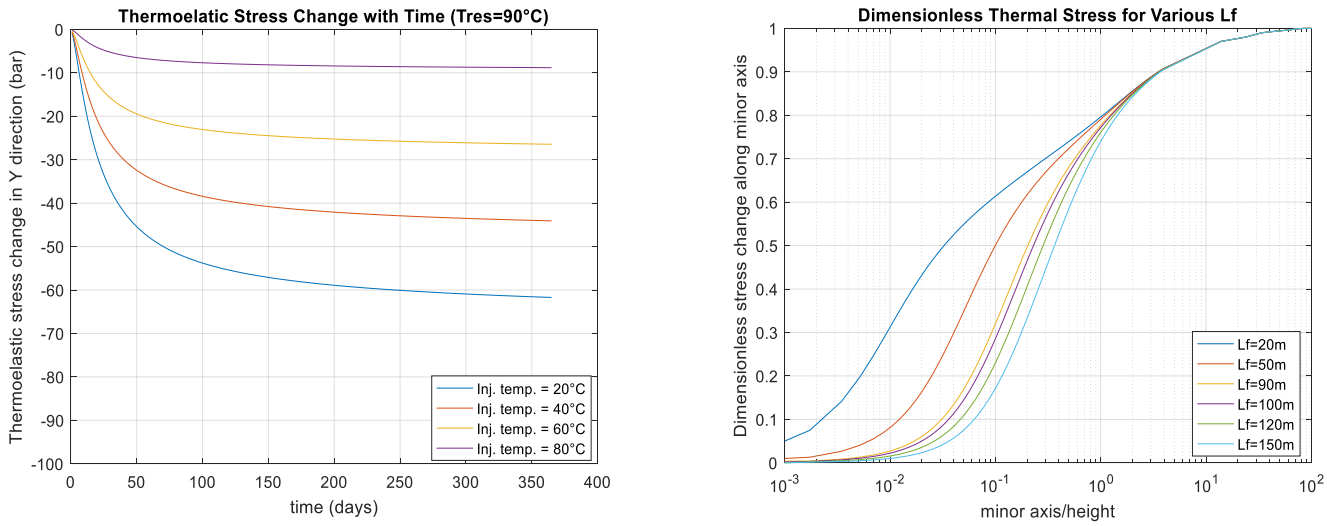

(a) (b)

Fig 6.18: (a) Thermo-elastic stress profile on fracture face for various injection water temperatures and T_{res} = 90℃ and, (b) Thermal stress change in an inclusion for various X_f/h ratios showing that the stress change grows when the fluid front grows to become much larger than reservoir height.

6.3. Fracture Propagation Solution

In this section, the results for fracture propagation models (dynamic case) are discussed. As discussed in Chapter 5, for the fracture tip model 1, the fracture length is iterated using the fracture propagation criterias given by Equation (5.3) such that, the evaluated stress intensity factor K_I at each time step converges with the constant fracture toughness K_{Ic} (user input). The integration in Equation (5.3) is carried out using trapezoidal method.

As discussed earlier, the following parameters are estimated to calculate the fracture length (X_f): Reservoir pressure at start of injection (P_{res}), Minimum in-situ stress before injection ($\sigma_{min,initial}$) which is an important parameter and is usually estimated from Step rate test, Total stress $(\Delta\sigma_{pT})$ on fracture face due to effects of pore pressure inflation and formation cooling, Poro-elastic coefficient (A_p) which is calculated from Biot coefficient and Poisson's ratio, Transmissivity ($k.h$) of the formation where permeability (k) must be estimated from well tests since core data are often not accurate reperesentative of large scale permeabilitites, Drainage radius (R_e) and, Fracture tip pressure (σ_{tip}). These parameters are inputed in Equation (5.3).

The results in Figure6.19 are obtained from the contant fracture toughness model for a constant fracture width w_0 profile. So, under the condition of volume of fracture being equal to volume of injected solids at any time, only the fracture length grows in this case until the entire fracture fills up with solids, and not the width. In Figure6.19(a), the model runs for over 6 months before X_f stops growing as length of plug becomes equal to length of fracture. In Figure6.19(b), the model runs for less than 2 months. This is because of the total suspended solids injected is 3 times more compared to case 1. Similarly, in 6.19(c) the model runs for almost 8 years as TSS is only 1 ppm. This shows the effect contaminents present in the injected fluid have on the duration of injection and thus, it can have a major say on the life span of the injection well.

In Figure6.19(c) and (d), a comparison is made between favourable and unfavourable mobility ratio (M). In 6.19(c), M<1 which is favourable condition but in 6.19(d) when M>1, the observation is different. The initial shoot up in X_f is because of the sudden pressure transient wave effect at start of model run whereas the slight dip that follows is because of the fact that a more viscous fluid is being pushed, that reduces X_f value. X_f then increases because of the external filter-cake effect that reduces leak-off and fracture propagates again. If TSS is zero in 6.19(d) then, the X_f curve will close completely and fracture will not propagate again. This could also be an artefact in the model's initial outputs. To validate this theory, results for similar case have been obtained from SLOFRAC (adapted from Shell) model as an example shown in Figure6.20.

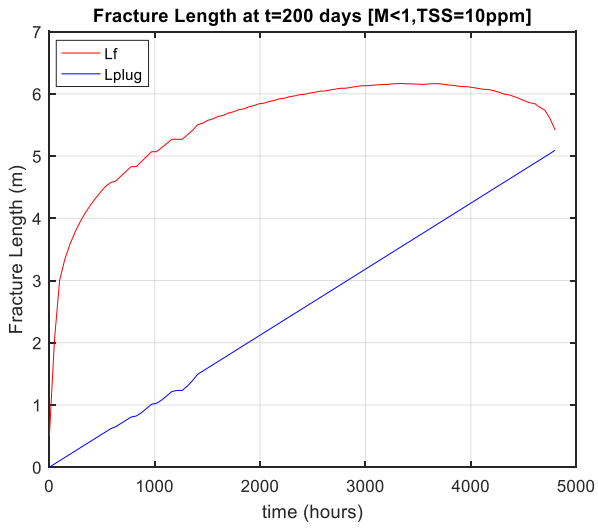

(a)

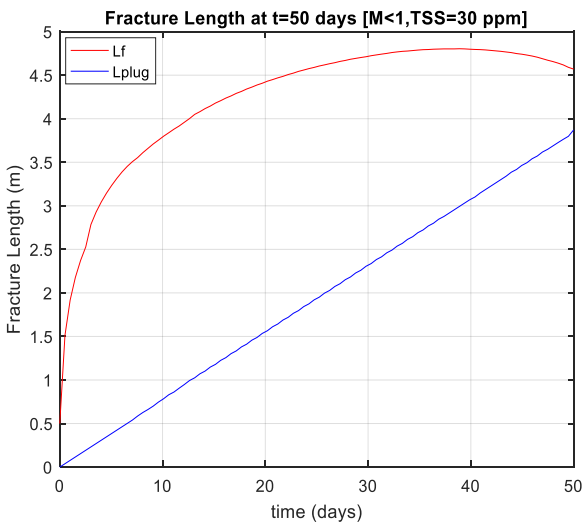

(b)

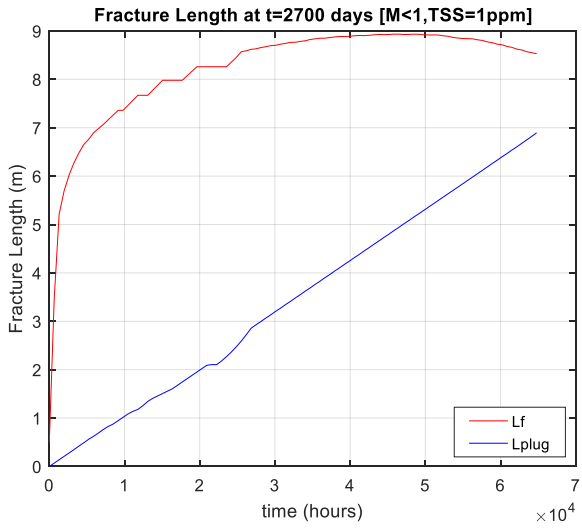

(c)

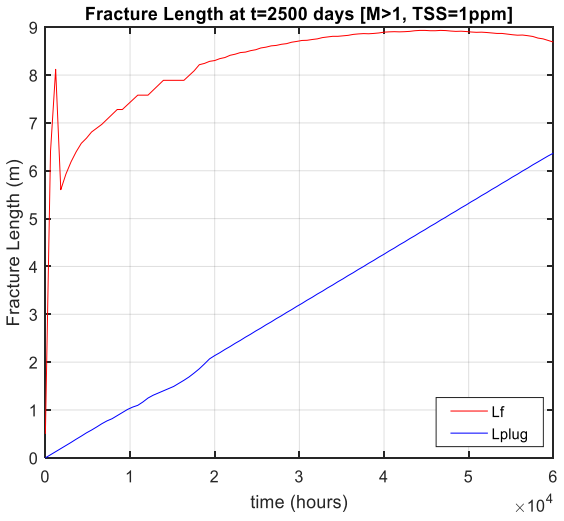

(d)

Fig 6.19: The results of analytical fracture propagation model with constant width for various degree of damage w.r.t the amount of TSS in injected water which are (a) 10 ppm, (b) 30 ppm and, (c) 1 ppm. In plot (d), the effect of an unfavourable mobility ratio (>1) is shown for case in (c).

In Figure6.20, the model used in SLOFRAC simulator gives results for case of M>1 i.e. an unfavourable mobility condition. The model is built for waterflooding under fracturing conditions using the Koning's formulations[1]. The novelty of the simple simulator is to estimate injection pressure and fracture length in very short time. Figure6.20(b) represents the conditions shown in Figure6.19(d) whereas, Figure6.20(a) shows the scenario that would occur when there is no fraction of oil/solids in injected water. So, in absence of any TSS, the effect of highly viscous fluid ahead of the front will cause gradual shrinkage of fracture as shown by blue curve in Figure6.20(a). Clearly, a closing X_f curve is indicative of such phenomena.

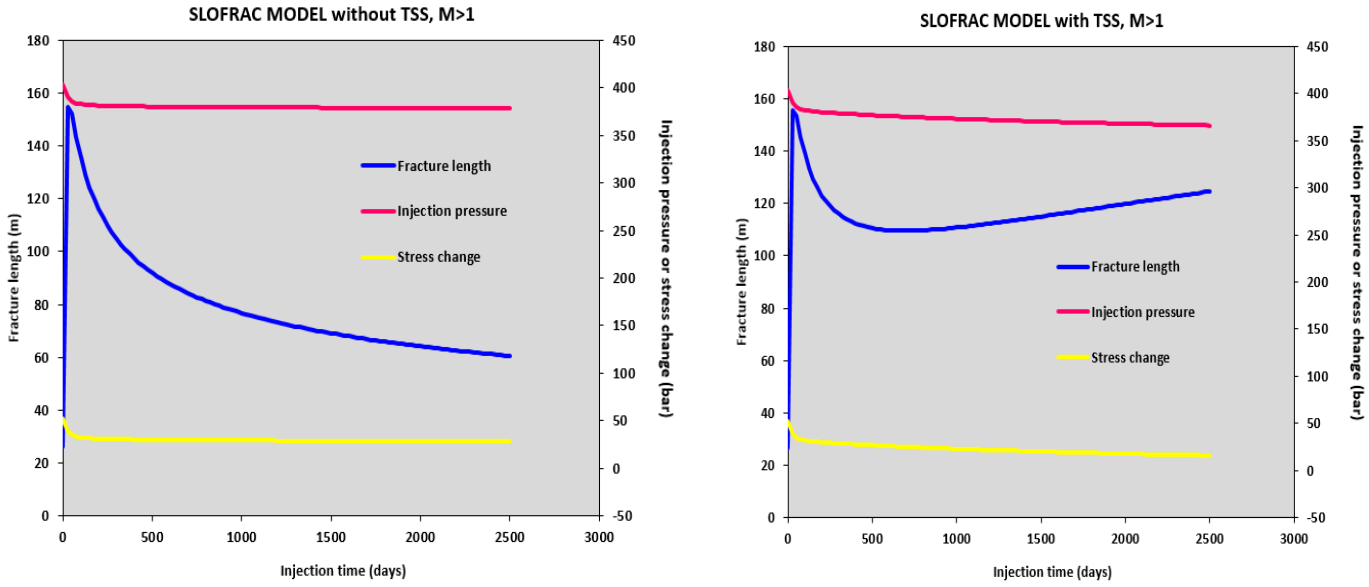

(a) (b)

Fig 6.20: Results from SLOFRAC model (adapted from Shell) for two cases where M>1 (unfavourable) (a) Without TSS fraction and, (b) With TSS fraction in injection fluid.

In material science, fracture toughness K_{Ic} represents the ability of a material containing a crack to resist fracturing[17]. In K_{Ic}, the subscript 'I' means mode I in which crack opens under a normal tensile stress perpendicular to the crack (minimum horizontal stress). It is basically a quantitative way of expressing material's resistance to fracturing. In Figure6.21(a), the tolerance error is estimated as difference between K_I and constant input value K_{Ic} and, is plotted with time for 100 days of iteration whereas, in Figure6.21(b), the tolerance error estimated as difference between K_I and increasing $K_{Ic,eff}$ and, is plotted with time for 10 days of injection. This is because Figure6.21(b) is obtained from fracture tip model 2 where K_{Ic} is not constant. Here, if the error is less than 0.1 i.e. K_I approaches K_{Ic} value, then the fracture length will converge and grow over time. Newton Raphson Method is used for convergence is common for all three fracture tip models discussed in this thesis.

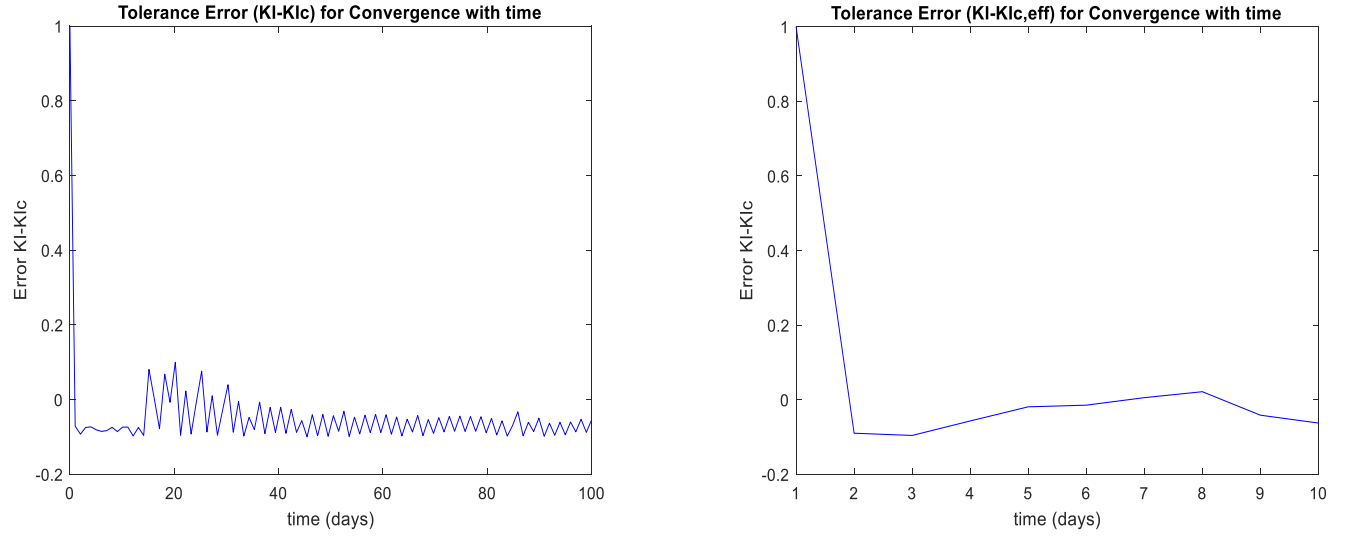

(b) (b)

Fig 6.21: (a) Tolerance Error $(K_I - K_{Ic})$ vs. time for fracture tip model 1 and, (b) Tolerance Error $(K_I - K_{Ic,eff})$ vs. time for fracture tip model 2. The fracture length converges if error is ≤ 0.1 in this case.

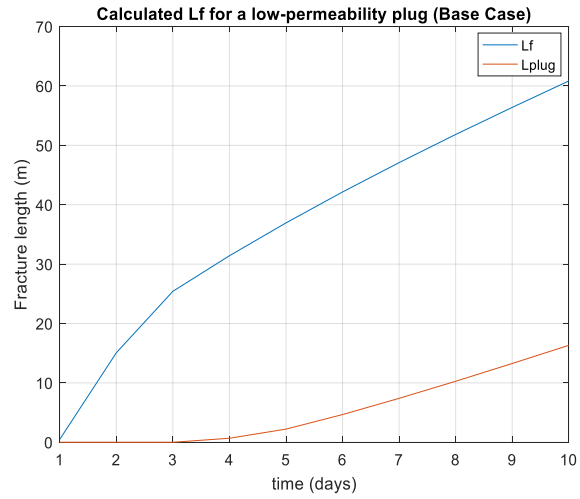

(a)

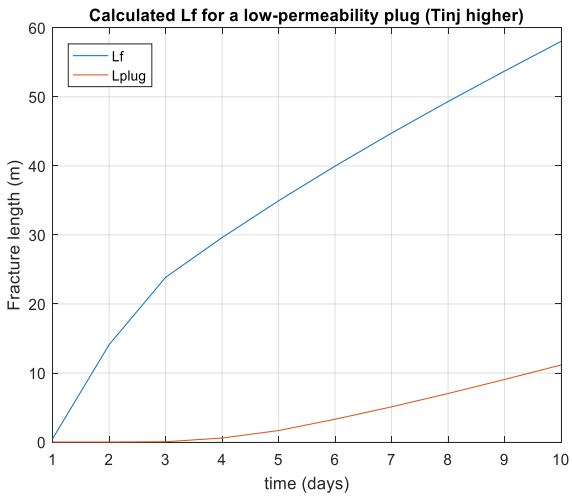

(b)

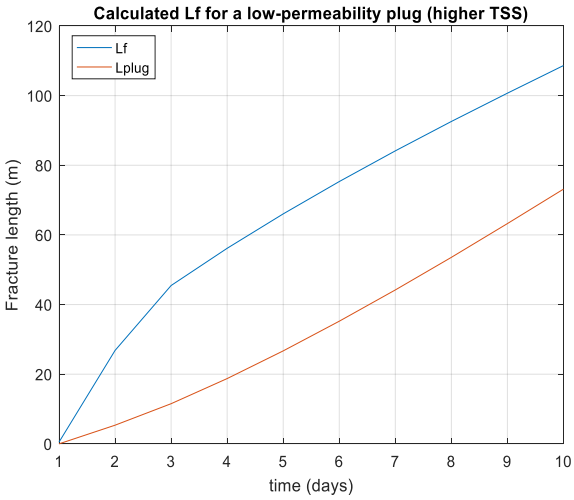

(c)

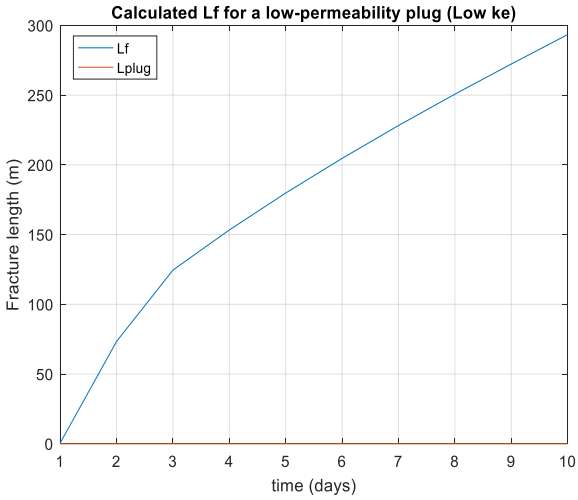

(d)

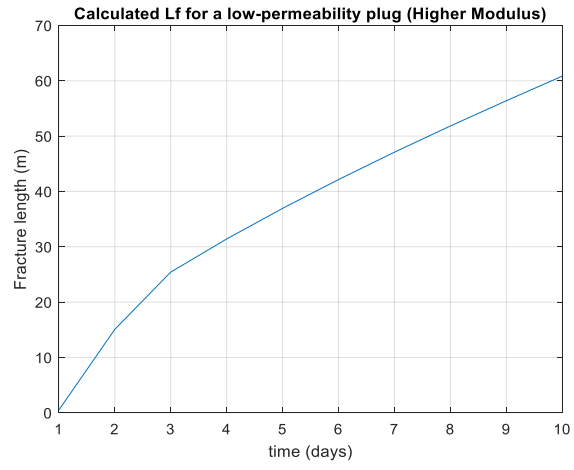

(e)

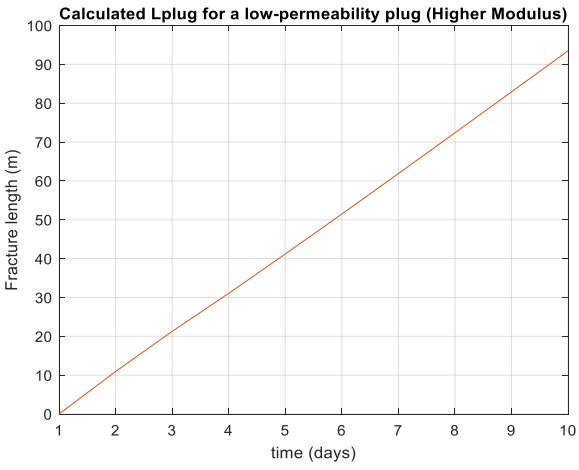

(f)

Fig 6.22: (a) Represents Base case for Tip Model with $K_{Ic} = 10\ bar\sqrt{(m)}$. Effect on X_f *and* L_{plug} with time due to change in (b) T_{inj}, (c) TSS, (d) Filter-cake permeability k_e and, (e) Young's modulus. (f) Shows the effect of high modulus on L_{plug}.

It is clear so far that fracture propagation is a self-generated recovery process in the system which is a consequence of damage caused to the system. In the set of results discussed in Figure6.22, the ballooning

effect has been modelled by including the dynamic elliptical fracture width profile unlike a constant fracture width mentioned earlier in Figure6.19. As we know, for the formation of plug, the volume of injected solids should exceed or equal the volume of fracture. In this model, this event is accompanied by increase in length of the fracture and widening of the fracture, so that the fracture can self-adjust its conductivity and volume to accommodate further newly injected solids in the next time step. It is to be noted that, if volume of fracture is more than volume of solids injected, the plug will not form despite fracture growing in length. This phenomenon is observed in the initial days of water injection where fracture volume is always more than volume of TSS.

The following trends can be proposed from the above results: -

- Figure6.22(a) represents the base case scenario for the fracture tip model 1. The main values input for the calculation of base case are $(i)\ k = 1D,\ (ii)\ TSS = 30ppm, (iii)\ k_e = 10\mu D, (iv)\ T_{inj} = 10℃\ or\ \Delta T = -70℃\ and, (v)\ E = 5E + 4\ bar$. The numerical model in each case is run for 10 days.
- Fracture size tends to increase in case of a low injection water temperature (T_{inj}) as shown in Figure6.22(b). This implies that the effect of $\Delta T = T_{inj} - T_{res}$ will be higher i.e. higher thermo-elastic backstress[18-20]. For cold water injection, thermo-elastic stress has a negative effect on net backstress on the fracture face. Therefore, the resulting higher net pressure ($P_{net} = P_{frac} - \Delta\sigma_{ypT}$) allows fracture to grow more over time.
- Fracture length tends to increase in case of high total suspended solids present in the injected water as shown in Figure6.22(c). The injection of more solids causes more damage to system and leads to formation of larger tip plug over prolonged period of injection, that balloons the fracture even more over time.
- The fracture length increases a lot if the permeability of external filter-cake is lower for the same TSS. This can be observed in Figure6.22(d), where $k_e = 1\mu D$ that leads to very large increase in X_f in same amount of time as in Figure6.22(a). The low filter-cake permeability leads to larger pressure drop over the fracture leading to more widening of the fracture. This may open the wormholes in the plug resulting in increase in net fracture conductivity. This allows more solids to be injected and increases the facture length over time and in turn the fracture volume as well. Also, the leak-off is lower due to formation of a low permeability filter-cake layer on fracture face. It is to be noted that $V_{frac} > V_{solids}$ as a result, and thus there is no plug formation seen.
- The Young's modulus appears to have hardly any effect on the fracture size. However, change in E has significant effect on the injection pressure. This is because the same fracture length X_f is observed for modulus of $5\ GPa$ & $10\ GPa$ in Figures 6.22(a) and 6.22(e). But, the length of tip plug is much more for a high modulus as seen in 6.22(f). This could be due to higher TSS accumulating inside the fracture for formation of higher stiffness. Also, for a high modulus case, the widening of fracture is less which is also responsible for lesser fracture growth.

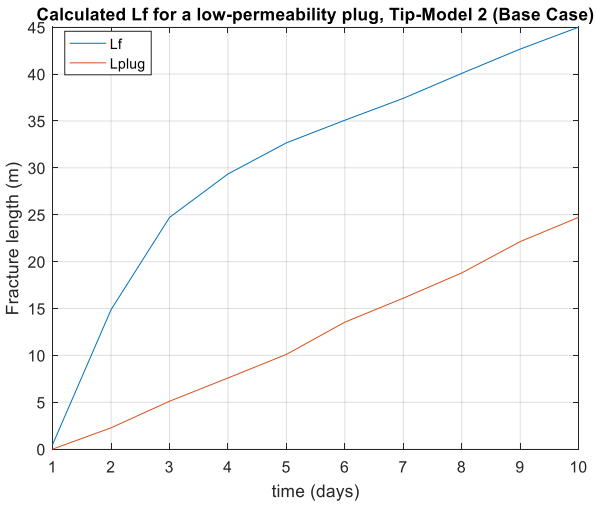

(a)

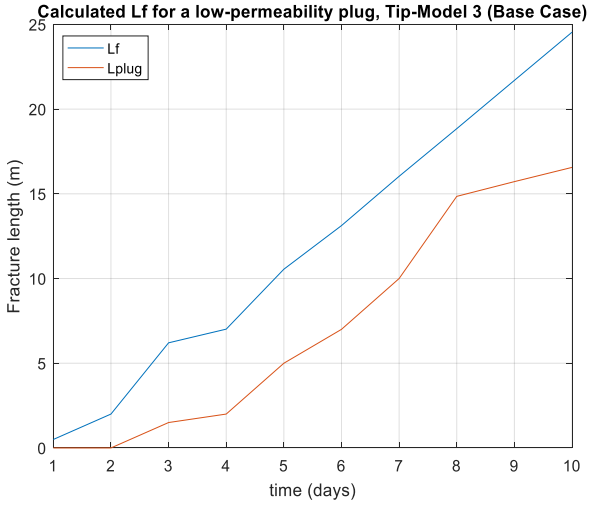

(b)

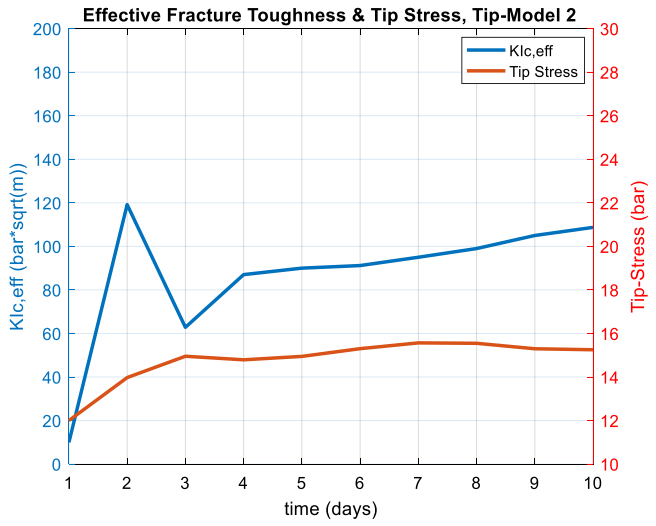

(c)

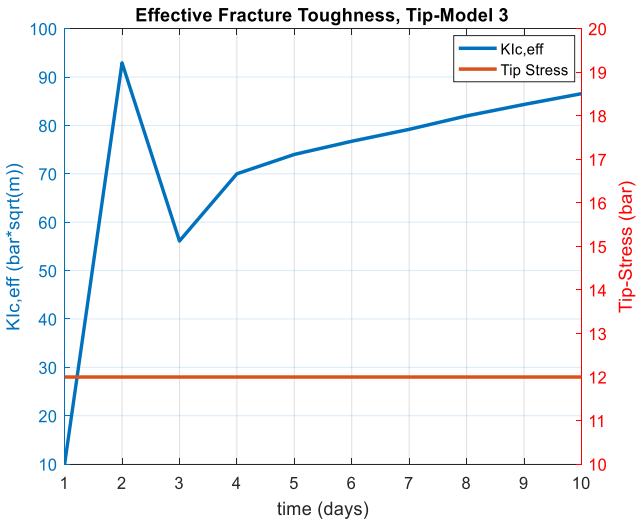

(d)

Fig 6.23: X_f and L_{plug} for (a) Fracture Tip Model 2 and, (b) Fracture Tip Model 3. (c) Increasing Effective Fracture Toughness and Tip Stress with increasing X_f for Tip Model 2 and, (d) Increasing Effective Fracture Toughness with increasing for a constant Tip Stress in Tip Model 3.

In this thesis, other two fracture tip models have also been executed apart from the constant fracture toughness model. They have also been described in detail in Chapter 5 earlier. In the results discussed above, the fracture length X_f and effective fracture toughness $K_{Ic,eff}$ obtained from fracture tip model with increasing tip stress (Model 2) and with constant tip stress (Model 3) respectively have been shown.

From Figure6.23 (a) and (b), it is observed that for the same injection time, model 2 and model 3 predict less fracture growth as compared to model 1. But, the main problem with model 1 is that the tip stress reduces with increasing X_f. On the other hand, in model 2 the tip stress gradually increases with increasing X_f as shown in Figure6.23(c). Fracture tip model 3 assumes a constant Tip Stress and so, only effective fracture toughness increases with X_f in this case as shown in Figure6.23(d). The same trend is also illustrated in Figure6.24 for different changing parameters namely $\Delta T, E,$ TSS and, k_e. It was also observed during computation of the numerical models that the iteration scheme was fastest in case of Model 3. This could be because the effective fracture toughness $K_{Ic,eff}$ increased at a fixed rate with every time step unlike other two models. This certainly makes the iteration scheme faster. Also, it is to be noted that the initial sharp increase in X_f observed is simply an artefact in the model.

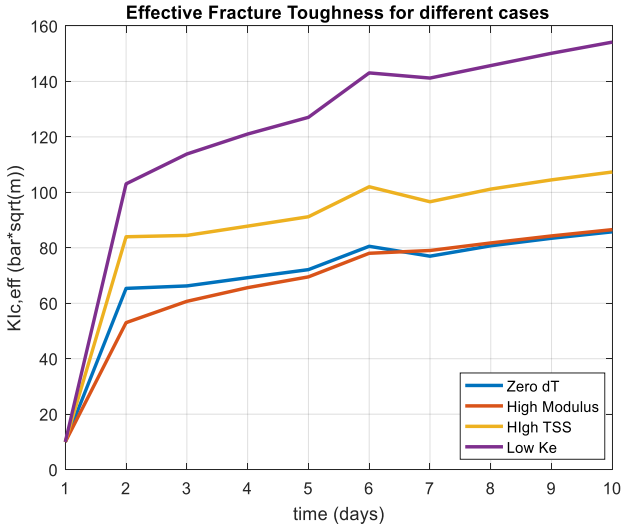

Fig 6.24: Represents the Effective Fracture Toughness calculated by changing different parameters. It illustrates the increasing $K_{Ic,eff}$ with increasing fracture length X_f.

6.4. Wellhead Pressure & Well Injectivity Analysis

In the section, the computed well head pressure as a function of injection time will be discussed. The WHP has been evaluated from bottom-hole injection pressure obtained from the numerical model. The assumption of no frictional losses has been made, which implies that (BHP-WHP) value gives the hydrostatic pressure. The results are obtained for an impermeable tip plug case for initial WHP~100bar. These results can also be compared to the computed WHP under assumption of uniform permeability profile in work of Hoek *et al.*[2]. This is shown in Figure6.25.

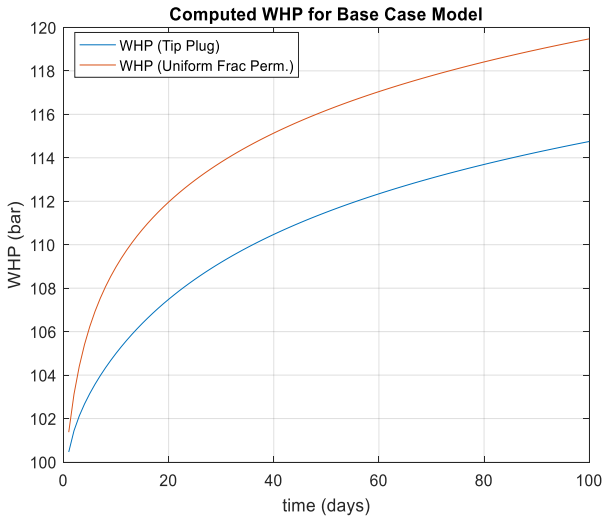

Fig 6.25: Comparative Plot for Calculated Wellhead Pressure (bar) between base case model with a tip plug and base case model with uniform fracture permeability.

The computed WHP in case of tip plug is basically minimum value (lower bound) of the range of WHP obtained. The upper bound of WHP is obtained for uniform fracture permeability profile where the fracture permeability (k_f) is iterated until fracture volume equals the solids volume. The Figure6.25 shows calculated WHP after 100 days of injection. It is observed that the injection pressure in case of a low permeability tip plug can be several times lower than in case of a uniform finite permeability fracture. Also, for most cases it has been observed that the gradual decline in well injectivities ($Q_{inj}/(BHP - P_{res})$) is lesser over time in case of a low permeability tip plug. This makes presence of a tip plug in a finite conductivity fracture a more realistic possibility over prolonged periods of injection.

Therefore, the following trends can be proposed from the above results: -

- Well injectivity initially does not depend on solids loading or amount of TSS in injected water. This is due to rapid growth of fracture initially in the model computations such that the fracture volume in initial stages is enough to accommodate all solids without any increase in the fracture width or ballooning effect. The initial injectivity depends mostly on T_{inj} and k_e as they significantly effect propagation pressure.
- Well injectivity will increase in case of low T_{inj} and k_e. This is because the increase in fracture sizes in both cases that leads to larger fracture volumes as discussed in section 6.3. So, lesser bottom-hole injection pressure will be required to balloon the fractures to accommodate more solids.
- Well Injectivity depends inversely on Young's modulus. It is observed that for a high modulus i.e. for high formation stiffness, more injection pressure is needed to balloon the fracture, which explains the low well injectivity in such case.
- In addition to above points, it is also observed that the WHP does not increase a lot after long duration of injection. The work of Hoek *et al.*[2] also compares this observation with the results of uniform finite conductivity fracture model and concludes that the WHP in tip plug model is significantly lower over time. This means that the well injectivity in a tip plug model is much better as it barely decreases. This argument is supported by the PWRI experience of BP in Prudhoe field[19], where they have been injecting produced water for over a decade without encountering any appreciable reduction in well injectivity.

7

Conclusions & Recommendations

7.1. Conclusions

In this thesis, a semi-analytical model is presented to predict growth of a finite conductivity fracture by constant injection of water containing suspended solids and oil droplets. The model can be used to forecast long term well injectivity and fracture size for water injection wells under fracturing conditions. The primary model condition implemented is that at any given time, the total fracture volume is equal to the total volume of injected solids. This is done to serve the purpose that the fracture is able to accommodate all injected solids, and propagate simultaneously. In order to allow the fracture to accommodate all solids in the injected water, it must be able to adjust its dimensions accordingly. Since, a rectangular elliptical fracture profile is used in this thesis, fracture length and width are main iteration parameters based on the above mentioned primary model condition. When the volume of fracture and volume of solids are equal, the fracture increases in length based on fracture propagation criterion mentioned in section 5.2, and it may or may not increase in width based on fracture width profile mentioned in section 5.4. The finite conductivity of the fracture depends on degree of internal plugging calculated using Equation (3.18), which is modelled to increase based on increase in X_f *and* $W_f(x,t)$ over time. The adjustment is done to minimise the energy of the system or pressure in this case, for stability.

The following conclusions are achieved based on the results laid out in Chapter 6,

1. Two-dimensional pseudo-radial pressure profile with elliptical discontinuities in fluid mobilities λ_i $(i = 1, 2 \,\&\, 3)$ has been calculated analytically for an infinite and finite conductivity fracture. It shows the elliptical symmetricity of pressure field around fracture depends on uniformity of fracture pressure.
2. Two-dimensional poro-elastic stress changes at fracture face has been calculated numerically assuming analytical pressure profile Δp constant along reservoir height and zero beyond elliptical reservoir boundary ξ_3. The main rock mechanical property in this model is the minimum horizontal stress changes perpendicular to fracture face $\sigma_{h,min}$. It's calculated using principle of superposition which is applied to calculate net poro-elastic backstress on fracture wall due to pore pressure in each grid block around the fracture.
3. The comparison of analytical poro-elastic stress results to Koning's results shows that, the analytical results are applicable for $\frac{X_f}{h} < 10$ condition. Moreover, there is very good agreement with Koning's numerical stress results too as shown in Tables 6.1 and 6.2.
4. Thermo-elastic stress change has been calculated analytically based on work of Perkins and Gonzalez[8]. It is assumed to be uniform on the fracture face unlike poro-elastic stress that varies with each source point on the fracture along x.
5. Tip plugging damage mechanism begins once the external filter-cake has built up on the fracture face and, no newly injected solids can penetrate adjacent formation. So, the newly injected solids remain in the fracture and start to form a plug at the fracture tip. This causes reduction in fracture permeability, and results in larger pressure drop over the fracture. This leads to ballooning of the fracture i.e. width increase, which opens wormholes in the external filter-cake and tip plug. So, a situation transpires in which the fracture conductivity adjusts itself such that, the fracture volume increases to accommodate newly injected solids in the fracture.

6. Impermeable tip plug behind the fracture tip along with infinite conductivity unplugged zone behind the tip plug is taken as total fracture conductivity profile. In this case, pressure drop over the fracture is concentrated behind the tip unlike in case of a uniform permeability fracture profile where it is uniformly spread over the entire fracture length. It is concluded that, in case of a tip plug present more volume of fracture can be achieved at lower injection pressure. Also, it is a more realistic possibility between the two scenarios.
7. The fracture tip propagation models are built on the fracture toughness criterion. The main condition is that at any given time, volume of fracture is equal to volume of solids injected. Once they are equal, the model shows that, fracture increase in length and width accordingly to increase its volume and accommodate more solids. This process necessarily doesn't result in significant increase in injection pressure. Also, the model iteration scheme tries to minimise the $(K_I - K_{Ic})$ *or* $(K_I - K_{Ic,eff})$ error value depending on the type of fracture tip model, with objective of X_f to converge.
8. In this model, the presence of tip plug suggests that over time there is lesser loss of well injectivity in comparison to when a clean water is injected where fracture conductivity tends to be infinite.
9. In this model, the computed fracture length X_f is relatively insensitive to the degree of internal plugging of fracture. It depends mainly on injected water temperature, filter-cake permeability, net stress conditions and fracture toughness.
10. Implementation of all three fracture tip models shows that, method of calculating effective fracture toughness for each time step along with either increasing tip stress (Model 2) or a constant tip stress (Model 3) is more realistic approach than a constant fracture toughness model (Model1).

7.2. Recommendations for Future Work

Despite the results obtained and conclusions reached, there can be further work done to improve the present model. The following recommendations are suggested for future work that can be carried out: -

1. The fracture width profile in the dynamic model for the fracture propagation case has been taken under several assumptions. The width profile can be modelled in a more detailed manner by using traditional 2D hydraulic fracturing models like PKN by Perkins, Kern and Nordgren[8] and KGD by Khristianovic, Zheltov (1955) & Geertsma, de Klerk (1969)[12]. Both these models have their own unique geometry but PKN model is more closely related to model description in this thesis as it also assumes fracture with constant height and elliptical cross-section in both horizontal and vertical plane. Also, fluid loss is included in PKN model as well which is neglected in this model.
2. The fracture propagation in this model is mainly based on the fracture tip model in which fracture toughness, K_{Ic} is assumed to a constant (material property). In the calculation that follows, the tip-stress reduces with increase in fracture length to zero over several days of injection. This is often not observed in practise rather a typically high or growing tip-stress is observed in time. So, two more fracture tip models have also been suggested in section 5.3 which give an effective fracture toughness that increases with fracture length. Therefore, this method can be worked on and included in this model in more detailed manner.
3. The poro-elastic stress calculation in this model has been done by dividing the reservoir into Cartesian grid blocks or parallelepipeds under assumption that, the pressure profile is constant over the reservoir height. This reduces the volume integral given in Chapter 4 into a 2D surface integral. So, for more detailed analysis of stress, in next stage a 3D model could be generated that estimates backstress on each point in the entire 3D rectangular fracture.
4. The plan view in this model is mentioned in Figure2.5, which also describes multiple zones around a fracture during produced water re-injection[2]. But, in this thesis only damage caused to fracture namely external filter-cake formation and internal plugging have been included. The damage zone is analogous to rest of the zones but it also could be significant w.r.t the injected solids and oil that deeply penetrates the formation, forming an internal filter-cake. In this model, all the injected solids and oils (TSS) are assumed to form external cake and internal tip plug.
5. In the volume integral of poro-elastic stress calculation, the numerical accuracy depends on how accurate is the pressure solution at that point. So, in case of numerical model, the grid size (memory of system) and the time requirements (cost) can compete with the resolution needed[7] to solve this volume integral accurately. Also, this problem may become more challenging due to presence of many

'for' loops in the model that increase the run time by many folds. So, solving the stress calculation in an interface like C/C++ is advised to save time more than anything else.

6. In this thesis, the plug permeability is taken to be k_{f2} and plug volume to be $\left(V_{plug} = TSS.i_w.t\right)$. This is assuming 100% water leak-off to formations and all TSS forming external filter-cake and internal plug. But, if leak-off occurs through the wormholes in the plug as well i.e. if porosity of plug is considered, then a correction factor can be applied to the plug volume like $V_{plug'} = \frac{V_{plug}}{1-\emptyset}$.
7. According to Equation (5.2), if $K_I < K_{Ic}$, then no shrinkage or propagation takes place. But, another concept called Quasi-static crack propagation where fracture continues to grow even when $K_I < K_{Ic}$ can be included in the model to understand behaviour of rocks that might behave in this unique way.
8. From conclusions 5 and 7 in section 7.1, it is seen that, the tip plug is formed when volume of solids equals volume of fracture. This is accompanied by fracture volume increase due to ballooning effect. In this model, the consequence of this effect on the fracture propagation equation has not been included. The increased pressure drop over the fracture due to reduction in fracture conductivity must effect the ΔP_{frac} and stress conditions. Therefore, the fracture propagation equation given by Equation (5.3) needs to be adjusted in the model at the time steps when $V_{solids} \geq V_{frac}$, to include effects of change in injection pressure.

References

[1] Koning, E.J.L. (1988). Waterflooding under fracturing conditions, Ph.D. Thesis, Technical University of Delft.
[2] Van den Hoek, P. J., Matsuura, T., de Kroon, M., & Gheissary, G., Shell Intl. E&P (1999, August 1). Simulation of Produced Water Reinjection Under Fracturing Conditions. SPE 57385.
[3] Suri, A., & Sharma, M.M. (2007). A model for water injection into frac-packed wells. SPE 110084.
[4] Abou-Sayed, A. S., & Zaki, K. S. (2005, January 1). A Mechanistic Model for Formation Damage and Fracture Propagation During Water Injection. SPE 94606.
[5] Van den Hoek, P. J., Hustedt, B., Sobera, M., Mahani, H., Masfry, R. A., Snippe, J., & Zwarts, D. (2008, January 1). Dynamic Induced Fractures in Waterflooding and EOR (Russian). SPE 115204.
[6] Van den Hoek, P. J., Matsuura, T., de Kroon, M., & Gheissary, G. (1996, January 1). Simulation of Produced Water Re-Injection Under Fracturing Conditions. SPE 36846.
[7] Ovens, J., & Niko, H. (1993, January 1). A New Model for Well Testing in Water Injection Wells Under Fracturing Conditions. SPE 26425.
[8] Perkins, T.K., & Gonzalez, J.A. (February 1985). The effect of Thermo-elastic Stresses on Injection Well Fracturing. SPE Journal.
[9] Koning, E. J. L., & Niko, H. (1985, January 1). Fractured Water-Injection Wells: A Pressure Falloff Test for Determining Fracture Dimensions. SPE 14458.
[10] Saripalli, K. P., Bryant, S. L., & Sharma, M. M. (1999, January 1). Role of Fracture Face and Formation Plugging in Injection Well Fracturing and Injectivity Decline. SPE 52731.
[11] Ji, L., Settari, A. T., Sullivan, R. B., & Orr, D. (2004, January 1). Methods for Modeling Dynamic Fractures in Coupled Reservoir and Geomechanics Simulation. SPE 90874.
[12] Jun Ge, B.S. (December 2009). Modelling and Analysis of Reservoir Response to Stimulation by Water Injection, M.Sc Thesis, Texas A&M University.
[13] Perkins, T. K., & Gonzalez, J. A. (1985, February 1). The Effect of Thermo-elastic Stresses on Injection Well Fracturing. SPE 11332-PA.
[14] Feng, Y., Jones, J. F., & Gray, K. E. (2016, May 1). A Review on Fracture-Initiation and -Propagation Pressures for Lost Circulation and Wellbore Strengthening. SPE 181747-PA.
[15] Riley, M.F. (1991). Finite Conductivity Fractures in Elliptical Coordinates, Ph.D. Thesis, Stanford University.
[16] Nowacki, S., (1962). Thermo-elasticity.
[17] Hertzberg, Richard W., (December 1995). Deformation and Fracture Mechanics of Engineering Materials (4 ed.). Wiley
[18] Paige, T., and Ferguson, M. Water Injection: Practical Experience and Future Potential, presented at the 1993 Offshore Water and Environmental Seminar, London, 29-30 March.
[19] Martins, J.P. *et al.*.: Long Term Performance of Injection Wells at Prudhoe Bay: The Observed effects of Thermal Fracturing and Produced Water Re-Injection. SPE 28936.
[20] Paige, R.W. *et al.*.: Optimising Water Injection Performance. SPE 29774.
[21] Muskat. M., The flow of homogenous fluids through porous media.
[22] Carter, R.D., Optimum fluid characteristics for fracture extension.
[23] Hagoort, J., Weatherill, B.D. & Settari, A., Modelling the propagation of waterflood-induced fractures.
[24] Gringarten, A.C., Ramey, H.J. & Raghavan, R., Unsteady-state pressure distribution created by a well with single infinite conductivity vertical fracture.

Nomenclature

A = major axis of ellipse

a_c = major axis of cold front

a_F = major axis of flood front

A_p = poro-elastic constant

A_T = thermo-elastic constant

a_{in}, b_{in} = Fourier coefficients in i^{th} zone

b = external filter-cake thickness, m

b_0 = external filter-cake thickness at fracture mouth, m

b = minor axis of ellipse

b_c = minor axis of cold front

b_F =minor axis of flood front

c_b = compressibility of bulk rock, /bar

c_g = compressibility of rock grains, /bar

c_t = total pore compressibility, /bar

C_o = heat capacity of fluid-filled reservoir rock, kg/m^3 °C

C_g = heat capacity of cap and base rock, kg/m^3 °C

C_w = heat capacity of injection water, kg/m^3 °C

$e_c = b_c/a_c$

$e_F = a_F/b_F$

erf = error function

erfc = complementary error function

f = fraction of oil & solids in water that deeply penetrates into the formation

$G(X_f,h)$ = fracture geometry factor in propagation criterion

h = reservoir height, m

i_w = total water injection rate, m^3/day

k_i = effective permeability in i^{th} zone, m^2

k_{ro} = relative permeability of oil (ko/k)

k_{rw} = relative permeability of water (kw/k)

k_e = external filter-cake permeability, m^2

$k_f(x)$ = fracture permeability profile, m^2

K_I = stress intensity factor, bar$\sqrt{m}$

K_{Ic} =critical stress intensity factor/ fracture toughness, bar$\sqrt{m}$

X_f or L_f = fracture half-length, m

X_{fu} or L_{fu} = fracture half-length of unplugged part, m

L_p = fracture length of plugged part (X_f-X_{fu}) or (L_f-L_{fu}), m

N = number of Fourier coefficients

N1 = total number of days injected

P = Pressure around the fracture, bar

P_{res} = initial reservoir pressure, bar

ΔP = P-P_{res}, pressure around the fracture, bar

ΔP_f = fluid pressure in fracture, bar

ΔP_{fp} = fluid pressure in plugged part of fracture, bar

ΔP_{fu} = fluid pressure in unplugged part of fracture, bar

ΔP_e = pressure drop over external filter-cake, bar

ql = total leak-off rate from fracture into reservoir, m^3/day

r_w = wellbore radius, m

R_e = radius of external boundary, m

rho_g = density of rock, kg/m^3

rho_o = density of oil, kg/m^3

rho_w = density of water, kg/m^3

σ_{ini} = initial total minimum in-situ stress, bar

$\sigma_{h,min}$ = min. horizontal reservoir rock stress, bar

σ_p = poro-elastic backstress on fracture face, bar

σ_{pp} = poro-elastic backstress on plugged part, bar

σ_{pfu} = poro-elastic backstress on unplugged part, bar

σ_T = thermo-elastic backstress, bar

σ_{pT} = sum of poro-elastic and thermo-elastic backstress, bar

S_{or} = residual oil saturation, %

S_{wi} = connate water saturation, %

t = injection time, days

T_{inj} = injection temperature, ℃

ΔT = T_{inj}-T_{res}, change in temperature with respect to initial temperature, ℃

V_{frac} = fracture volume, m^3

w_0 = fracture width at fracture mouth, m

w(x) = fracture width profile, m

W_i = total injected water volume, m^3

x, y = Cartesian coordinates, m

ξ_i = ξ coordinate of boundary between zones i and i+1

Greek

a_p = linear poro-elastic expansion coefficient

a_S = thermal diffusivity of cap and base rock

a_T= linear thermal expansion coefficient

ξ_{ij} = Kronecker delta

η = hydraulic diffusivity

λ_i = fluid mobility of i^{th} zone

μ_i = viscosity of i^{th} zone

Φ = porosity, %

ξ, η = elliptical coordinates

ξ_u, η_u = elliptical coordinates using X_{fu}

Subscripts

1 cold fluid zone

2 warm fluid zone

3 oil zone

D dimensionless

c cold front

F flood front

Appendix A

The Appendix provides the calculations of pressure field solution in and around a finite conductivity fracture. The fracture fully penetrates permeable formation and is assumed to be bounded by impermeable layers. The concepts are discussed in detail in Chapter 3 earlier. The calculations given in the appendix are based on work of Hoek *et al.*[2].

A.1. Calculation of Pressure Solution in and Around a Finite Conductivity Fracture

A semi-analytical model has been developed to solve for the pressure field in and around the finite conductivity fracture. In this case, the pressure drop over the fracture will be nonzero due to non-uniform fracture pressure, that will disturb the elliptical symmetry of pressure field around the fracture. The pressure profile Δp(ξ) must satisfy the full Laplace Equation given by Equation (3.19). Clearly, the pressure field depends on both the elliptical coordinates ξ and η.

The governing Equation is discussed in section 3.4 given by Equation (3.20). The boundary conditions used to solve the Laplace Equation are given by Equation (3.10) and (3.11). As mentioned earlier, Fourier series is used to express the pressure solution such that, the boundary conditions and elliptical symmetry in η are satisfied. The Fourier coefficients are required to model the pressure equations. So, the pressure solutions $\Delta p(\xi)$ given by Equation (3.20) are substituted into the boundary conditions followed by multiplication with $\cos(2\eta)$, and then it is integrated over η between $\left(0, \frac{\pi}{2}\right)$. This gives the five Fourier coefficients required to solve pressure Equations for the three zones around the fracture. They are given by Equation (3.21). In order to calculate all the unknown Fourier coefficients $a_{1n}, a_{2n}, b_{1n}, b_{2n}, and\ b_{3n}$, we only have four Equations derived by above mentioned calculations. A fifth Equation is derived by local fluid balance in the finite conductivity fracture[2].

A.1.1. Pressure solution without external filter-cake on fracture face

The 1D fracture is divided into uniform grids along the x-direction. According to the local fluid balance in the fracture,

$$Q_{local}(x) = Q_{inj} - Q_{\ leakoff} \tag{A.1}$$

where, $Q_{local}(x)$ means the fluid rate along fracture at position x, Q_{inj} is the constant injection flow rate also represented by i_w, and $Q_{\ leakoff}$ is the leak-off between (0, x). This has been expressed mathematically in work of Hoek *et al.*[2] by,

$$-\frac{1}{2}h.w(x).\frac{kf(x)}{\mu_1}.\frac{\partial \Delta pf(x)}{dx} = \frac{i_w}{4} + \int_0^x dx' \frac{k_1}{\mu_1} h \frac{\partial \Delta p_1(x', y)}{dy} | y = 0 \tag{A.2}$$

where, $\Delta p_f(x)$ is the fracture pressure due to fluid pressure inside the fracture, $w(x)$ represents the fracture width profile given in section 5.4 in Chapter 5, and $k_f(x)$ is the assumed fracture permeability profile (step function). If an elliptical fracture width profile is used, then $w(x)$ can also be expressed as,

$$w(x) = w0\sqrt{1 - \left(\frac{x}{X_f}\right)^2} \quad or, \qquad w(\eta) = w0\sin(\eta) \tag{A.3}$$

So, Equation (A.2) can be modified and expressed in elliptical coordinates as,

$$\frac{d\Delta p_f(\eta)}{d\eta} = \frac{2X_f}{w_0 k_f(\eta)} \left\{ \frac{\mu_1 i_w}{4h} - k_{\ 1} \int_{\frac{\pi}{2}}^{\eta} d\eta' \frac{\partial \Delta p_1(\xi, \eta')}{\partial \xi} | \xi = 0 \right\} \tag{A.4}$$

Equation (A.4) is now the main Equation for carrying out local fluid volume balance. To include the effect of absence of external filter-cake the following Equation is used,

$$\Delta p_f(\eta) = \Delta p_1(\xi = 0, \eta) \quad or, \quad \Delta p_f(x) = \Delta p_1(x, y = 0) \tag{A.5}$$

where, Δp_1 is the pressure drop in the adjacent formation to the fracture or cold zone.

Now, to solve for the coefficient b1m the following steps are executed,

Step 1: Equation (A.5) and 1st Equation of set of Equations (3.20) are substituted in Equation (A.4). This gives the following output,

$$-\sum_{m=1}^{\infty} 2m.\, d_{1m}\,.\sin(2m\eta) = \frac{2X_f}{w_0.\, k_f(\eta)} \left\{ \frac{\mu_1}{\mu}\, k\eta + k_1 \sum_{m=1}^{\infty} c_{1m} \sin(2m\eta) \right\} \tag{A.6}$$

where, we get two new coefficients which are defined by,

$$d_{1m} \equiv a_{1m} \cosh(2m\xi_1) + b_{1m} \sinh(2m\xi_1)\ ,\ \ c_{1m} \equiv a_{1m} \sinh(2m\xi_1) + b_{1m} \cosh(2m\xi_1) \tag{A.7}$$

Step 2: To calculate b_{1m}, Equation (A.7) is expressed only in terms of coefficient b_{1m}. This is done by substituting Equation (3.21) in Equation (A.7) and is given by,

$$\begin{aligned} d_{1m} &= \left(\tfrac{k_1}{k_2} \tanh[2m(\xi_2 - \xi_1)] \cosh(2m\xi_1) + \sinh(2m\xi_1)\right) b_{1m}\ , \\ c_{1m} &= \left(\frac{k_1}{k_2} \tanh[2m(\xi_2 - \xi_1)] \sinh(2m\xi_1) + \cosh(2m\xi_1)\right) b_{1m} \end{aligned} \tag{A.8}$$

Step 3: Equation (A.8) is substituted in the derived Equation from step 1. This gives an Equation which is only in terms of b1m.

$$\begin{aligned} -\sum_{m=1}^{\infty} 2m \left(\left(\frac{k_1}{k_2} \tanh[2m(\xi_2 - \xi_1)] \cosh(2m\xi_1) + \sinh(2m\xi_1) \right) b_{1m} \right) \sin(2m\eta) \\ = \frac{2X_f}{w_0 * k_f(\eta)} \left\{ \frac{\mu_1}{\mu}\, k\,\eta + k_1 \sum_{m=1}^{\infty} \left(\left(\frac{k_1}{k_2} \tanh[2m(\xi_2 - \xi_1)] \sinh(2m\xi_1) + \cosh(2m\xi_1) \right) b_{1m} \right) \sin(2m\eta) \right\} \end{aligned} \tag{A.9}$$

Step 4: Equation (A.9) is multiplied by $\sin(2n\eta)$ and is then integrated over $\eta = (0, \frac{\pi}{2})$. This provides the following result,

$$-\frac{\pi}{2} n\, d_{1n} = \frac{2X_f}{w_0} \frac{k}{\mu} \int_0^{\frac{\pi}{2}} d\eta \frac{\mu_1}{k_f(\eta)}\, \eta \sin(2n\eta) + \frac{2X_f}{w_0} \sum_{m=1}^{\infty} c_{1m} \int_0^{\frac{\pi}{2}} d\eta \frac{k_1}{k_f(\eta)} \sin(2m\eta) \sin(2n\eta) \tag{A.10}$$

The fracture permeability in this model is assumed by a step function given by Equation (3.18). This $k_f(\eta)$ is used along with d1m and c1m from Equation (A.8) to solve Equation (A.10) for b1m. The combination of Equation (A.10) and (A.8) gives a linear set of Equations relation of the form $Ax = B$ for the coefficient b_{1m}. So, the linear set of Equations is modelled in MATLAB to solve this with x equal to b_{1m}, B being a constant vector and, A being coefficient matrix of b_{1m}. Once b_{1m} is calculated, the other coefficients of Fourier sum are simply calculated using Equation (3.21).

From the above Equations, it can be deduced that for an infinite conductivity case, $k_f(\eta) \equiv \infty$ due to which the RHS in Equation (A.10) equals zero. Therefore, all three coefficients of Fourier sum b_{1m}, b_{2m}, a_{1m} are zero. Thus, Equation (3.20) reduces to Equation (3.12) for an infinite conductivity fracture.

A.1.2. Pressure solution with external filter-cake on fracture face

The external filter-cake layer on fracture face is built over time due to deposition of TSS. The filter-cake in this model is assumed to have elliptical thickness profile $b(x)$ given by Equation (3.14) and uniform filter-cake permeability k_e. The presence of external filter-cake results in additional pressure drop over the fracture. This pressure drop Δp_e is uniform for an infinite conductivity fracture because of uniform pore pressure distribution[1] $\Delta p(\xi)$ around the fracture given by Equation (3.12). The Δp_e is therefore given by,

$$\Delta p_e = \frac{\partial \Delta p(\xi)}{\partial \xi} | \xi = 0. b_0 \qquad (A.11)$$

But, for finite fracture conductivity case, due to the non-uniformity of pore pressure distribution around the fracture the pressure drop over the external filter-cake is now given by,

$$\Delta p_e = \left(\frac{\mathrm{k}_1}{k_e}\right)\left(\frac{b_0}{X_f}\right)\frac{\partial \Delta p_1(\xi, \eta)}{\partial \xi} | \xi = 0 \qquad (A.12)$$

So, the fracture permeability Equation (A.5) modifies to,

$$\Delta p_f(\eta) = \Delta p_1(\xi = 0, \eta) - \left(\frac{\mathrm{k}_1}{k_e}\right)\left(\frac{b_0}{X_f}\right)\frac{\partial \Delta p_1(\xi, \eta)}{\partial \xi} | \xi = 0 \ \ or, \qquad \Delta p_f(x) = \Delta p_1(x, y = 0) - \left(\frac{\mathrm{k}_1}{k_e}\right) b(x) \frac{\partial \Delta p_1(x, y)}{\partial y} | y = 0 \qquad (A.13)$$

where, $0 \leq \eta \leq \left(\frac{\pi}{2}\right)$

Now, to solve for the coefficient $\mathrm{b}_{1\mathrm{m}}$ the following steps are executed,

Step 1: Equation (A.13) and 1st Equation of set of Equations (3.20) are substituted in Equation (A.4). This gives the following output,

$$-\sum_{m=1}^{\infty} 2m\left(d_{1m} + 2m\left(\frac{\mathrm{k}_1}{k_e}\right)\left(\frac{b_0}{X_f}\right)c_{1m}\right)\sin(2m\eta) = \frac{2X_f}{w_0 . k_f(\eta)}\left\{\frac{\mu_1}{\mu}\, k\eta + k_1 \sum_{m=1}^{\infty} c_{1m}\sin(2m\eta)\right\} \qquad (A.14)$$

where, d_{1m} and c_{1m} are given by (A.8).

Step 2: Similar steps are followed again to deduce the linear set of Equations. However, the presence of external filter-cake slightly changes the linear set of Equations given by Equation (A.10).

$$-\frac{\pi}{2} n \left(d_{1n} + 2n\left(\frac{\mathrm{k}_1}{k_e}\right)\left(\frac{b_0}{X_f}\right)c_{1n}\right) = \frac{2X_f}{w_0}\frac{k}{\mu}\int_0^{\frac{\pi}{2}} d\eta \frac{\mu_1}{k_f(\eta)}\, \eta \sin(2n\eta) + \frac{2X_f}{w_0}\sum_{m=1}^{\infty} c_{1m} \int_0^{\frac{\pi}{2}} d\eta \frac{k_1}{k_f(\eta)} \sin(2m\eta)\sin(2n\eta) \qquad (A.15)$$

Therefore, a new linear set of Equations of the form $Ax = B$ is generated and modelled in MATLAB to evaluate the coefficient of Fourier sum b_{1m}, $\Delta p(\xi)$, and $\Delta p_f(\eta)$ using $k_f(\eta)$.

Appendix B

The Appendix provides the calculations of poro-elastic and thermo-elastic backstresses on fracture face. The concepts are discussed in detail in Chapter 4 earlier. The calculations of numerical model for poro-elastic backstress given in the appendix are based on Equations formulated by Koning[1] in Appendix 3-B of his thesis. The thermo-elastic backstress calculations for elliptical zones confocal with fracture tips are based on work Perkins and Gonzalez[8]. The thermo-elastic stress is calculated for uniform change in temperature. The temperature profile is assumed to be a step function. Inside the cold zone, a uniform temperature decrease is taken and outside the cold zone the initial reservoir temperature prevails.

B.1. Numerical Calculation of Poro-elastic backstress at the Fracture Wall

After the evaluation of pressure profiles or the pressure field around the fracture, the poro-elastic backstress is calculated numerically. The following general expression is given by Hoek *et al.*[2] to solve it,

$$\sigma_p(x) = A_p * \Delta p(x) + \frac{A_p}{4\pi}\frac{\partial^2}{\partial y^2}\iiint \frac{\Delta p(x')}{|x-x'|}\, d^3x' \qquad (B.1)$$

where, A_p is the poro-elastic constant.

In this model, the above volume integral is calculated only in two-dimensions along the length of fracture and perpendicular to the fracture throughout the reservoir. Since, the analytical pressure profile is constant along the reservoir height, the integral over the third dimension drops out. As discussed in Chapter, the reservoir or coordinate space has been divided into parallelepipeds with edges of length $2a_1$,$2a_2$,$2a_3$ in the x, y, z directions respectively. In this model, equal size grids have been used which means the edges are of equal length. The horizontal stress σ_{ijp} given by Equation (4.9) has been taken from Appendix 3-B of Koning's thesis[1]. The solution of integrals in Equation (4.9) are given by,

$$I_{ij}\,(u_1,u_2,u_3) = \int_{a_1}^{a_1} dk_{\,1}\int_{a_2}^{a_2} dk_{\,2}\int_{a_3}^{a_3} dk_{\,3}\frac{\partial^2}{\partial k_{\,i}\partial k_j}[(u_1-k_1)^2+(u_2-k_2)^2+(u_3-k_3)^2]^{-\left(\frac{1}{2}\right)} \qquad (B.2)$$

where, $u_1 = x_0 - x, u_2 = y_0 - y, u_3 = z_0 - z$ are the displacements in all three directions between the source point on the fracture and the field point in space. In Equation (B.2), I11 represents the coefficient integral of maximum horizontal stress $\Delta\sigma xp$ and I22 represents the coefficient integral of minimum horizontal stress $\Delta\sigma_{yp}$. In this thesis, only the minimum horizontal stress perpendicular to the fracture in of interest. The analytical calculation of I_{ij} is given by Nowacki[16]. For completeness I_{11} and I_{22} are given by,

$$\begin{aligned} I_{11} = {} & \operatorname{atan}\left(\frac{u_2-a_2}{u_1-a_1}\right)\frac{u_3-a_3}{r_{(+1,+2,+3)}} - \operatorname{atan}\left(\frac{u_2-a_2}{u_1-a_2}\right)\frac{u_3+a_3}{r_{(+1,+2,-3)}} - \operatorname{atan}\left(\frac{u_2+a_2}{u_1-a_1}\right)\frac{u_3-a_3}{r_{(+1,-2,+3)}} + \operatorname{atan}\left(\frac{u_2+a_2}{u_1-a_1}\right)\frac{u_3+a_3}{r_{(+1,-2,-3)}} \\ & - \operatorname{atan}\left(\frac{u_2-a_2}{u_1+a_1}\right)\frac{u_3-a_3}{r_{(-1,+2,+3)}} + \operatorname{atan}\left(\frac{u_2-a_2}{u_1+a_1}\right)\frac{u_3+a_3}{r_{(-1,+2,-3)}} + \operatorname{atan}\left(\frac{u_2+a_2}{u_1+a_1}\right)\frac{u_3-a_3}{r_{(-1,-2,+3)}} \\ & - \operatorname{atan}\left(\frac{u_2+a_2}{u_1+a_1}\right)\frac{u_3+a_3}{r_{(-1,-2,-3)}} \end{aligned} \qquad (B.3)$$

$$\begin{aligned} I_{22} = {} & \operatorname{atan}\left(\frac{u_1-a_1}{u_2-a_2}\right)\frac{u_3-a_3}{r_{(+1,+2,+3)}} - \operatorname{atan}\left(\frac{u_1-a_1}{u_2-a_2}\right)\frac{u_3+a_3}{r_{(+1,+2,-3)}} - \operatorname{atan}\left(\frac{u_1+a_1}{u_2-a_2}\right)\frac{u_3-a_3}{r_{(+1,-2,+3)}} + \operatorname{atan}\left(\frac{u_1+a_1}{u_2-a_2}\right)\frac{u_3+a_3}{r_{(+1,-2,-3)}} \\ & - \operatorname{atan}\left(\frac{u_1-a_1}{u_2+a_2}\right)\frac{u_3-a_3}{r_{(-1,+2,+3)}} + \operatorname{atan}\left(\frac{u_1-a_1}{u_2+a_2}\right)\frac{u_3+a_3}{r_{(-1,+2,-3)}} + \operatorname{atan}\left(\frac{u_1+a_1}{u_2+a_2}\right)\frac{u_3-a_3}{r_{(-1,-2,+3)}} \\ & - \operatorname{atan}\left(\frac{u_1+a_1}{u_2+a_2}\right)\frac{u_3+a_3}{r_{(-1,-2,-3)}} \end{aligned} \qquad (B.4)$$

where, $r_{(\mp1,\mp2,\mp3)} = [(u_1 \mp a_1)^2 + (u_2 \mp a_2)^2 + (u_3 \mp a_3)^2]^{\frac{1}{2}}$

Also, the coefficient I_{22} is obtained by interchanging $u_1 \leftrightarrow u_2$ and $a_1 \leftrightarrow a_2$ in coefficient I_{11}.

B.2. Calculation of Axes of Elliptical Fluid Fronts

In this section, the solution for the major and minor axes of elliptical temperature and flood fronts are calculated. The method incorporated by Perkins and Gonzalez[8] is used to obtain the axes values. The elliptical coordinates for thermal zone is calculated from heat balance whereas, for flood front it is calculated from volume balance.

First, the volume of an arbitrary elliptical front is given by,

$$V_i = \pi X_f^2 h \sinh(\xi_i) \cosh(\xi_i) \ , \qquad i = c, F \tag{B.5}$$

where, c= cold/temperature front zone and F= flood front zone

From heat balance, we get the volume of the cold front given by,

$$V_c = \frac{M_w}{M_r} q\, t \tag{B.6}$$

Where, M_w = Heat capacity of injected water and, M_r = Heat capacity of fluid filled reservoir rock.

We know, in the zone ahead of the cold zone and behind the flood front, connate water is mobile with oil at residual saturation i.e. $S_o = S_{or}$. The volume of flooded zone equals the volume of displaced mobile oil. So, the volume of waterflooded region includes the volumes of injection water and connate water[3]. From volume balance, we get the volume of the flood front by the following relation,

$$V_F = \frac{1}{\varphi(1 - S_{or} - S_{wc})} q\, t \tag{B.7}$$

We know, in elliptical system major axis is given by $a_i = X_f \cosh(\xi_i)$ and, minor axis is given by $b_i = X_f \sinh(\xi_i)$ from Equation (B.6) and (B.7) it follows that,

$$a_i = \frac{X_f}{2}\left(\sqrt{F_i} + \frac{1}{\sqrt{F_i}}\right) \text{ and, } \qquad b_i = \frac{X_f}{2}\left(\sqrt{F_i} - \frac{1}{\sqrt{F_i}}\right) \tag{B.8}$$

where,

$$F_i = \frac{2\ V_i}{\pi X_f^2 h} + 0.5\sqrt{\left(\frac{4\ V_i}{\pi X_f^2 h}\right)^2 + 4} \ , i = c, F \tag{B.9}$$

Appendix C

In this Appendix, the computational sequences implemented in MATLAB for all the fracture tip propagation models have been illustrated. The concepts of fracture propagation and fracture propagation criteria have been earlier discussed in Chapter 5 in detail. The models have been built for both analytical and numerical expressions for all three cases. Due to high computational time for numerical models, the results for analytical fracture propagation model have only been discussed in Chapter 6 for few cases.

The general fracture propagation Equation using which the above fracture tip models are solved is given by,

$$\frac{1}{\sqrt{\pi X_f}} \int_0^{X_f} dx \left[P_{frac}(q,t,X_f,h,x) - \sigma_i - \Delta\sigma_{pT}(q,t,X_f,h,x)\right]\sqrt{\frac{X_f+x}{X_f-x}} = G(X_f,h)\,K_{Ic} \qquad (C.1)$$

where, $G(X_f,h)$ is the Fracture Geometry Factor that depends on the length of the fracture. In this model, a slow growing fracture has been assumed for which $G(X_f,h) = 1$. Also, the integral in Equation (C.1) is evaluated using the Trapezoidal rule in MATLAB. In this model, the volume of fracture and volume of injected solids are also evaluated at each time step to estimate the plug length under the condition that $V_{solids} \geq V_{frac}$. The following Equations are used to do so,

$$V_{frac}(t) = \pi\ h \int_0^{X_f} X_f(x,t).w(x,t)\ dx \qquad (C.2)$$

$$V_{solids}(t) = TSS.i_w.t \qquad (C.3)$$

C.1. Fracture Tip Model with Constant Fracture Toughness, K_{Ic}

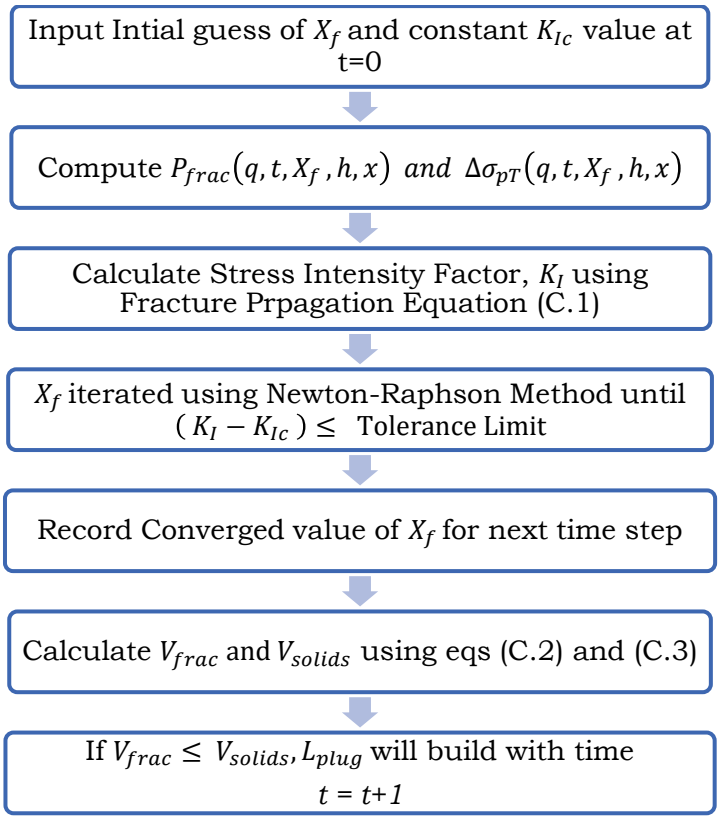

C.2. Fracture Tip Model with Increasing Tip-Stress, $\Delta\sigma_{tip}$

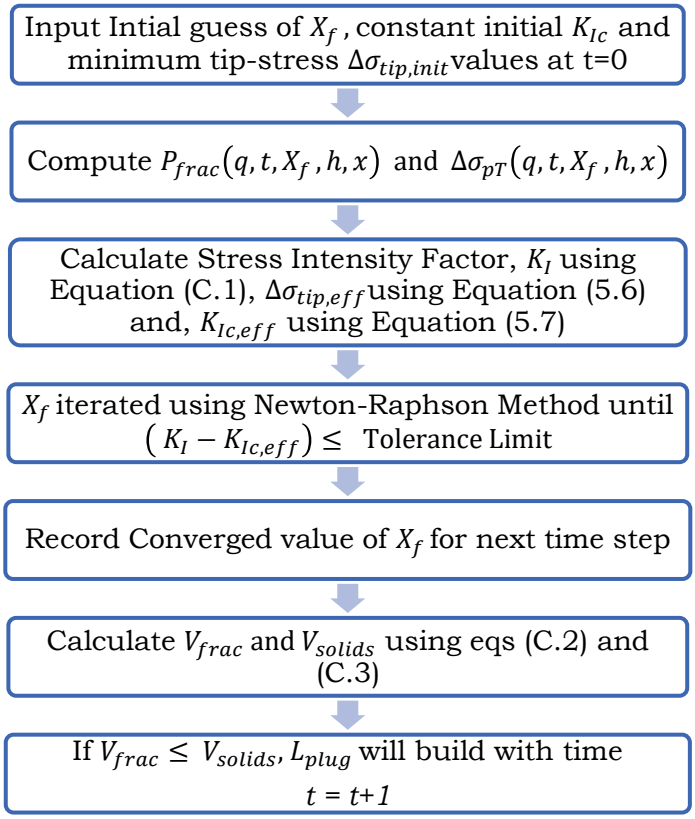

C.3. Fracture Tip Model with Constant Tip-Stress, $\Delta\sigma_{tip}$

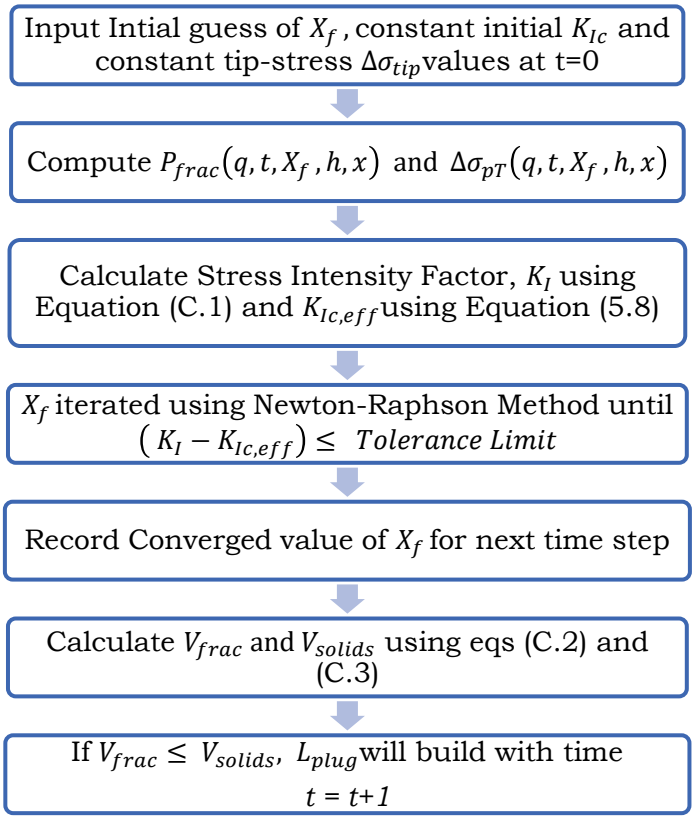

Appendix D

In this Appendix, the key simulation parameters model properties are defined for clarity of concept and complete understanding of the thesis and model's essential elements.

D.1. Simulation Parameters

NAME	DESCRIPTION
Depth (L)	Total Vertical Depth (TVD) of reservoir
Fracture Gradient (P/L)	Initial $\sigma_{h,min}$ gradient for fracture propagation
Hydrostatic Gradient (P/L)	$P_{bhp} = P_{whp} + P_{hyd} - \Delta p_{loss}$
Temperature Difference (ΔT)	$\Delta T = T_{inj} - T_{res}$
Maximum Drainage Radius (L)	$R_e = 1.5\sqrt{(\eta t)}$
Time Step (Δt)	$\Delta t = t_i + 1 - t_i$
Initial Fracture half-length (L)	X_{fi} = Initial guess
Injection Rate (L^3/t)	i_w = Constant Injection Rate

D.2. Rock Properties

NAME	DESCRIPTION
Reservoir Porosity (-)	$\emptyset$ = (Void Volume)/(Bulk Volume)
Young's Modulus of Formation (P)	E=Elasticity Modulus, Measure of Stiffness
Poisson's Ratio (-)	$\nu = -\frac{\text{Transverse Strain}}{\text{Longitudional Strain}}$ due to Axial compression
Tip Stress (P)	σ_{tip} = Stress at tip to overcome P_{frac}
Fracture Toughness ($P.L^{0.5}$)	$K_{Ic} = \sigma_{tip}\sqrt{(\pi X_f)}$
Initial Total In-Situ Stress (P)	$\sigma_{initial}$ (before injection starts)
Single Phase Permeability (L^2)	Permeability of Formation in Darcy
External Filter-cake Permeability (L^2)	k_e in micro-Darcy
Grain Density (M/L^3)	ρg = Density of Rock Grains

D.3. Fluid Properties

NAME	DESCRIPTION
Cold Water Viscosity (P.t)	μ_c = Viscosity of Cold Injection Fluid in Pa.s
Warm Water Viscosity (P.t)	μ_w = Viscosity of Heated Injection Fluid in Pa.s
Oil Viscosity (P.t)	μ_o = Viscosity of Reservoir Fluid in Pa.s
Residual Water Saturation (-)	S_{wi} = Irreducible Injection Fluid Saturation
Residual Oil Saturation (-)	S_{wi}i = Irreducible Reservoir Fluid Saturation
Injection Fluid Density (M/L^3)	ρ_w = Density of Cold Injection Fluid Phase
Oil Density (M/L^3)	ρ_w = Density of Reservoir Fluid
Injection Fluid Relperm (-)	Relative Permeability of Cold Injection Fluid Phase
Total Suspended Solids (-)	TSS (ppm) = Fraction of Solids in Injection Water
Initial Reservoir Pressure (P)	P_{res} (before injection starts)

D.4. Poro-elastic Parameters

NAME	DESCRIPTION
Grain Compressibility (1/P)	C_g = Relative Change in Grain Volume by ΔP
Water Compressibility (1/P)	C_w = Relative Change in Injection Fluid Volume by ΔP
Oil Compressibility (1/P)	C_O = Relative Change in Reservoir Fluid Volume by ΔP
Biot Coefficient (-)	$\alpha_B \approx (0.4 - 1.0)$

D.5. Thermo-elastic Parameters

NAME	DESCRIPTION
Thermal Expansion Coefficient (1/T)	Relative change in Saturated Rock due to ΔT
Water Specific Heat (E/M/T)	C_{aphw} = Mass Specific Heat of Injection Fluid
Grain Specific Heat (E/M/T)	C_{aphg} = Mass Specific Heat of Rock Grains
Oil Specific Heat (E/M/T)	C_{apho} = Mass Specific Heat of Reservoir Fluid
Heat Capacity of Injection Fluid (E/ L^3/T)	$C_w = 4200 \frac{KJ}{m^3}$/℃
Heat Capacity of Fluid Filled Rock (E/ L^3/T)	$C_w = 2500 \frac{KJ}{m^3}$/℃
Heat Capacity of Reservoir Fluid (E/ L^3/T)	$C_w = 2100 \frac{KJ}{m^3}$/℃